

AD-756 259

NEW METHODS FOR GROWTH AND CHARACTERI-
ZATION OF GaAs AND MIXED III-V SEMI-
CONDUCTOR CRYSTALS

William R. Wilcox, et al

University of Southern California

Prepared for:

Advanced Research Projects Agency

31 December 1972

DISTRIBUTED BY:

NTIS

National Technical Information Service
U. S. DEPARTMENT OF COMMERCE
5285 Port Royal Road, Springfield Va. 22151

AD 756259

USCEE Report 437



UNIVERSITY OF SOUTHERN CALIFORNIA

NEW METHODS FOR GROWTH AND CHARACTERIZATION OF GaAs AND MIXED III-V SEMICONDUCTOR CRYSTALS

Principal Investigator: William R. Wilcox

Semiannual Technical Report
(July 1972 - 31 December 1972)

Prepared for
The Advanced Research Projects Agency
ARPA Order Number 1628
Grant No. DAHC 15-72-G7

Approved for public release. ~~Classification Authority~~; all others
should apply to the Clearinghouse for Federal Scientific and
Technical Information

ELECTRONIC SCIENCES LABORATORY

Reproduced by
NATIONAL TECHNICAL
INFORMATION SERVICE
U S Department of Commerce
Springfield VA 22151

Engineering

UNCLASSIFIED

Security Classification

DOCUMENT CONTROL DATA - R & D		
<i>(Security classification of title, body of abstract and indexing annotation must be entered when the overall report is classified)</i>		
1. ORIGINATING ACTIVITY (Corporate author) Electronic Sciences Laboratory University of Southern California Los Angeles, California 90007		2a. REPORT SECURITY CLASSIFICATION UNCLASSIFIED
		2b. GROUP
3. REPORT TITLE NEW METHODS FOR GROWTH AND CHARACTERIZATION OF GaAs AND MIXED III-V SEMICONDUCTOR CRYSTALS		
4. DESCRIPTIVE NOTES (Type of report and inclusive dates) SEMI-ANNUAL TECHNICAL REPORT		
5. AUTHOR(S) (First name, middle initial, last name) WILLIAM R. WILCOX		
6. REPORT DATE 1 July 1972 - 31 December 1972	7a. TOTAL NO. OF PAGES 106	7b. NO. OF REFS 35
8a. CONTRACT OR GRANT NO. DAHC 15-72-G7	9a. ORIGINATOR'S REPORT NUMBER(S) USCEE Report 437	
b. PROJECT NO. ARPA Order No. 1628	9b. OTHER REPORT NO(S) (Any other numbers that may be assigned this report)	
c.		
d.		
10. DISTRIBUTION STATEMENT Approved for public release; distribution unlimited.		
11. SUPPLEMENTARY NOTES Details of illustrations in this document may be better studied on microfiche		12. SPONSORING MILITARY ACTIVITY The Advanced Research Projects Agency
13. ABSTRACT The purpose of this program is to develop new and improved methods for the growth and characterization of gallium arsenide (GaAs) and mixed III-V semiconductor crystals. This is being accomplished by laboratory experiments and related theoretical research. The program is a continuation of one initiated in July 1970 under ARPA Order Number 1628, Grant Number DAHC15-70-G14, and continued under DAHC15-71-G6. Ten floating zone passes were completed on 1 cm diameter GaAs using our new liquid encapsulation technique. Optimal conditions for growth of 1 cm diam GaAs by the travelling heater method. Ga In _{1-x} Sb and Ga Al _{1-x} As were also prepared. Studies were also made on a new Czochralski technique permitting growth of dislocation-free GaAs, on the gradient freeze growth technique, on nucleation of gas bubbles during crystallization, on oxygen measurement and pumping by electrochemical methods, on cathodoluminescence and electrical anisotropy due to introduction of dislocations, on Si in GaAs, on the influence of light on cathodoluminescence, and on GaAs Schottky barriers.		

DD FORM 1473
1 NOV 65

I 6

Security Classification

14.	KEY WORDS	LINK A		LINK B		LINK C	
		ROLE	WT	ROLE	WT	ROLE	WT
	gallium arsenide, floating zone, liquid encapsulation, travelling heater method, Czochralski, dislocation-free, gradient freeze, gas bubbles, oxygen, cathodoluminescence, Si, light, Schottky barriers.						

FC

Semiannual Technical Report

1 July 1972 - 31 December 1972

NEW METHODS FOR GROWTH AND CHARACTERIZATION
OF GaAs AND MIXED III-V SEMICONDUCTOR CRYSTALS

University of Southern California
Los Angeles, California 90007

Submitted to

ADVANCED RESEARCH PROJECTS AGENCY

ARPA Order Number 1628
Grant Number DAHC 15-72-G7
1 July 1972 - 30 June 1973
\$184,586.00

Principal Investigator: William R. Wilcox: (213) 746-6203

Investigators:	Clarence R. Crowell:	746-6217
	Agerico L. Esquivel:	746-6224
	Eric S. Johnson:	746-6403
	Pat Leung:	746-6403
	James M. Whelan:	746-6219
	David B. Wittry:	746-2510

Details of Illustrations in
this document may be better
studied on microfiche

The views and conclusions contained in this document are those of the authors and should not be interpreted as necessarily representing the official policies, either expressed or implied, of the Advanced Research Projects Agency or the U.S. Government.

La

TABLE OF CONTENTS

	Page
SUMMARY	iv
I. BULK CRYSTAL GROWTH	1
A. Liquid-Seal Czochralski Technique	1
1. Silica Crucible with Silicon Susceptor	1
2. Silica Crucible with Vitreous Carbon Susceptor	4
3. Alumina Crucible with Direct Coupling to the Melt	4
B. Liquid-Encapsulated Floating Zone Melting	5
C. Travelling-Heater Method	15
1. Influence of Growth Parameters on THM Growth of GaAs	15
2. Temperature Profile Measurement inside GaAs Crystal during THM Growth	23
3. Seeding and Impurity Doping in THM Growth of GaAs	28
4. Dislocation Propagation during THM Growth of GaAs	33
5. Segregation in THM Growth	35
6. Growth of $Ga_xIn_{1-x}Sb$ and $Ga_xAl_{1-x}As$	41
II. STUDIES OF CRYSTAL GROWTH PHENOMENA	43
A. Organic Analog of Gradient Freeze Growth	43
1. Experiments	43
2. Interface Shape - Without Cooled End	43
3. Interface Shape - With Cooled End	49
B. Organic Analog Experiments on Zone Melting	51
C. Other Crystallization Studies	55
III. OXYGEN MEASUREMENT AND CONTROL IN LIQUID EPITAXIAL GROWTH OF III-V SEMICONDUCTORS	56

IV. CHARACTERIZATION	59
A. Dislocation Studies and Electrical Properties	59
1. Cathodoluminescence Study of Deformed Regions in n-type GaAs	59
2. Electrical Anisotropy from α and β dislocations in Plastically Deformed GaAs	74
B. Si Local Modes in GaAs	84
C. Infrared Modulation of Cathodoluminescence	89
D. Cathodoluminescence of GaAs, GaP and GaAs _{1-x} P _x	91
E. High Impedance Hall System	93
F. Schottky Barrier Capacitive Characterization	96
1. Measurement Facilities	97
2. Measurements	97
G. Tunnel and Thermal Effects in Photoemission in Schottky Barriers	102
REFERENCES	103

SUMMARY

The purpose of this program is to develop new and improved methods for the growth and characterization of gallium arsenide (GaAs) and mixed III-V semiconductor crystals. This is being accomplished by laboratory experiments and related theoretical research. The program is a continuation of one initiated in July 1970 under ARPA Order Number 1628, Grant Number DAHC 15-70-G14, and continued under DAHC 15-71-G6.

Nine low dislocation content GaAs crystals with a variety of dopings were pulled by our new liquid-seal Czochralski technique. Different crucibles were tried in a vain attempt to improve mobilities. Carbon contamination was successfully eliminated, without effect. Ten floating zone passes were successfully made on GaAs with our new liquid-encapsulation technique. We are developing methods for zoning ingots larger than the present 1 cm. The parameters influencing growth of GaAs by the travelling heater method were determined. Optimal conditions for a 1 cm diameter crystal and 1 cm long heater were found to be: 1 cm long seed, 0.55 to 0.7 cm initial Ga zone, heater temperature of 980°C and a lowering rate of about 1.5 mm/day. The axial dislocation density increased upon seeding and then decreased rapidly upon growth, unless the ampoule was quenched. The radial dislocation density was relatively constant. Large grained ingots of $\text{Ga}_{1-x}\text{In}_x\text{Sb}$ and $\text{Ga}_{1-x}\text{Al}_x\text{As}$ were also prepared by THM.

Organic analog experiments were performed on gradient-freeze growth, previously shown by us to be useful for GaAs. Cooling the

bottom of the tube made the freezing interface more convex and aided grain selection, as predicted by theory. Analog experiments on zone melting revealed information on convection currents, interface shapes and breakdown, and heat transfer coefficients. A theory for nucleation of gas bubbles during crystallization was developed and found to correspond with experience.

The zirconia electrochemical method for measuring and controlling oxygen in liquid epitaxial growth is being successfully developed.

Cathodoluminescence was used to observe dislocations generated by bending GaAs. Electrical properties were found to be anisotropic. The nature of Si in GaAs was elucidated by local mode measurements of ^{30}Si doped crystals. Cathodoluminescence of Cr-doped GaAs increased rapidly as the wavelength of impinging light decreased below 1.6μ . Light had no effect with high-resistivity undoped GaAs. The high-impedance Hall system was completed and measurements are being taken. The activation energy found thereby for a high-resistivity (nominally) undoped GaAs sample was 0.708 eV, corresponding to Cr doping. The Schottky-barrier capacitance, voltage, frequency apparatus is functioning. Frequency dispersion was observed on a nickel on n-type GaAs diode.

Ten scientific papers resulted from this program during the last six months.

The following equipment was purchased under this grant:

residual gas analyzer, cold trap, multipoint recorder, amplifier, pre-amplifier, desk calculator, flow control system, motor potentiometer, two temperature controllers and a programmer.

I. BULK CRYSTAL GROWTH

A. Liquid-Seal Czochralski Technique

P. Leung

In the last report [1] it was suggested that the presence of carbon may be responsible for the low mobilities and high resistivities of the undoped GaAs crystals grown by this technique. We planned to explore other possible GaAs crucible materials since the carbon crucibles were a source of carbon in the crystals as well as a possible source of other impurities. Therefore, during the past six months, a major effort was devoted to studying the feasibility of various materials to be used as crucibles. This technique has also been used to grow GaAs doped with ^{30}Si for infrared local mode absorption studies (see Sec. IV. B). All the crystals grown in this period are listed in Table I.

1. Silica Crucible with Silicon Susceptor

Silicon was considered as a good possibility as a susceptor material since it has a higher melting point than gallium arsenide, and is easily heated by RF induction. A susceptor was machined from a polycrystalline silicon ingot. It was then oxidized at about 1100°C over 24 hours. Originally, it was planned to carbonize the surface and use it as a crucible. However, since carbon was found in material grown in a vitreous carbon crucible, a fused silica crucible was used instead, with the silicon as the susceptor. During the test run, there was no difficulty in coupling to the silicon susceptor. However, it was not possible to

TABLE I

<u>Crystal No.</u>	<u>Dopant</u>	<u>Carrier Concentration (cm³)</u>	<u>Mobility (cm² volt⁻¹ sec⁻¹)</u>	<u>Samples Sent To</u>	<u>Purpose</u>	<u>Remarks</u>
CZ-48	Cr					Too much oxide on surface of melt, probably due to too much chromium doping. Ingot was polycrystalline.
CZ-49	Undoped					Trial run with silicon susceptor and quartz liner. The susceptor was melted before the Ga and As could be reacted.
CZ-50	³⁰ Si	2.5 × 10 ¹⁸		P. Leung	Si-doped GaAs local modes	Tried to control ³⁰ Si-doping. It appeared to have a slight amount of ²⁸ Si contamination, probably from the seed.
CZ-51	³⁰ Si	5.9 × 10 ¹⁸		P. Leung	Si-doped GaAs local modes. Mass Spec. Analysis	Absorption spectrum showed little ²⁸ Si.

<u>Crystal No.</u>	<u>Dopant</u>	<u>Carrier Concentration (cm³)</u>	<u>Mobility (cm²volt⁻¹ sec⁻¹)</u>	<u>Samples Sent To</u>	<u>Purpose</u>	<u>Remarks</u>
CZ-52	Undoped	8×10^{17}		P. Leung	Local modes. Mass Spec. Analysis	Trial run with carbon susceptor and quartz liner. Local mode measurements indicated much less carbon but an appreciable amount of Si contamination.
CZ-53	Undoped	9.2×10^{16}	2850	P. Leung	Local modes. Mass Spec. Analysis	Trial run with Al ₂ O ₃ crucible. No carbon local mode.
CZ-54	$^{30}\text{Si} + ^{28}\text{Si}$			P. Leung	Si Local modes. Mass Spec. Analysis	Regrowth of CZ-51 with added ^{30}Si and ^{28}Si . Absorption measurements showed too little ^{30}Si .
CZ-55	$^{30}\text{Si} + ^{28}\text{Si}$	6.1×10^{18}		P. Leung	Si local modes. Mass Spec. Analysis	Regrowth of CZ-54 with ^{30}Si added. Measurements showed approximately equal concentrations of ^{28}Si and ^{30}Si .
CZ-56	Cr	High ρ		S. Nieh	Absorption at 10.6 μ region	Much less than previous chromium doping was used. No problem with oxide forming on surface of melt. Ingot was single crystal.
				D. Wittry	Luminescence measurements of Cr-level	

provide enough heat to form and melt the gallium arsenide without melting the Si. Perhaps the difference between the melting points of GaAs (1240°C) and Si (1420°C) is not large enough because of the temperature drop through the crucible.

2. Silica Crucible with Vitreous Carbon Susceptor

With a fused silica crucible and a vitreous carbon susceptor, we expected less carbon in the material since the GaAs melt would not be in direct contact with the vitreous carbon. During the run the diameter control was not good. Nevertheless, a crystal was grown. Local mode measurements made on this material showed that the amount of carbon was much less compared to an undoped crystal grown in a vitreous carbon crucible. Local mode absorption data also showed that this material contained $\sim 8 \times 10^{17}/\text{cm}^3$ Si, probably from the silica crucible.

3. Alumina Crucible with Direct Coupling to the Melt

Previous attempts with alumina crucibles were not successful because the crucibles fractured due to thermal stresses, allowing gallium to leak out. This problem was avoided by placing the Al_2O_3 crucible on top of another upside-down Al_2O_3 crucible. With radio frequency induction heating, the power had to be coupled directly to the GaAs melt, and the diameter control was considerably more difficult. Since there was no carbon in the material (as shown by local mode measurements), the electrical data would be expected to be much improved. However, the measured electrical resistivity of $0.024 \Omega\text{-cm}$, carrier concentration of

$9.2 \times 10^{16}/\text{cm}^3$, and the mobility of $2850 \text{ cm}^2/\text{volt sec}$ were close to the values for some of the undoped materials grown with the vitreous carbon crucible. This led us to suspect that the present B_2O_3 seal material (99.95%) may not be pure enough. Impurities may have been introduced into the melt through vapor transport from the B_2O_3 seal. Our next attempt will be to use a higher-purity grade B_2O_3 (99.999% or 99.9999%) to determine if the purity of the crystals can be improved.

We are now awaiting the results of mass spectrographic analysis performed by Battelle Memorial Institute on crystals grown in carbon, SiO_2 with carbon susceptor, and Al_2O_3 to further study the impurities present in the crystals.

B. Liquid-Encapsulated Floating Zone Melting

Eric Johnson

The development of a technique for liquid encapsulated floating zone melting of GaAs has continued [2]. Problems involving the induction heating apparatus and a procedure for drying boron oxide have been solved. Likewise, procedures for the introduction of the GaAs feed rod into molten encapsulant, maintenance of a stable floating zone while containing volatile As, and the removal of the GaAs ingot from the encapsulant upon completion of zoning, have all been shown to be feasible. The best effort previously reported (ingot FZ - 7) achieved three floating zone passes on an 8 mm diameter GaAs feed rod. However, that ingot was not recovered intact from the encapsulant. Further

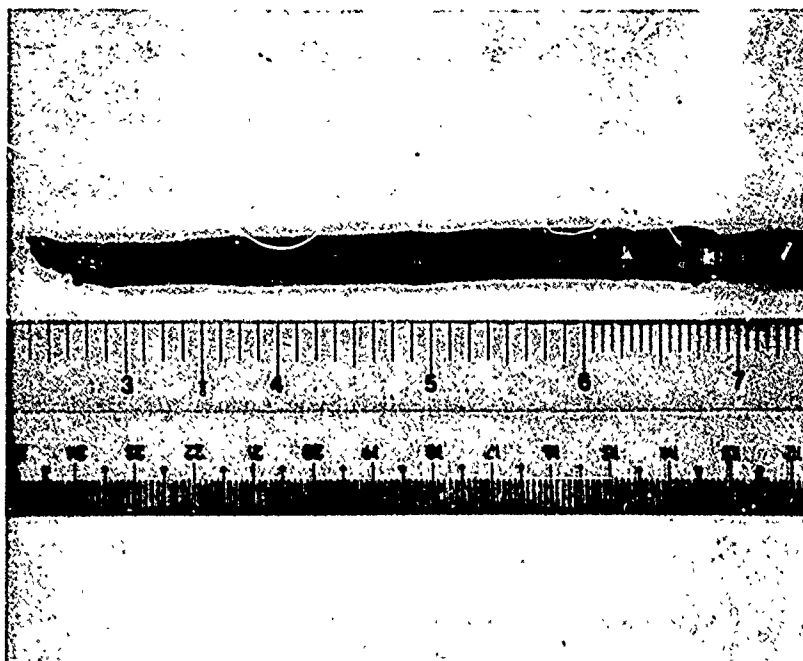


Figure 1: FZ-8 after 6 floating zone passes.

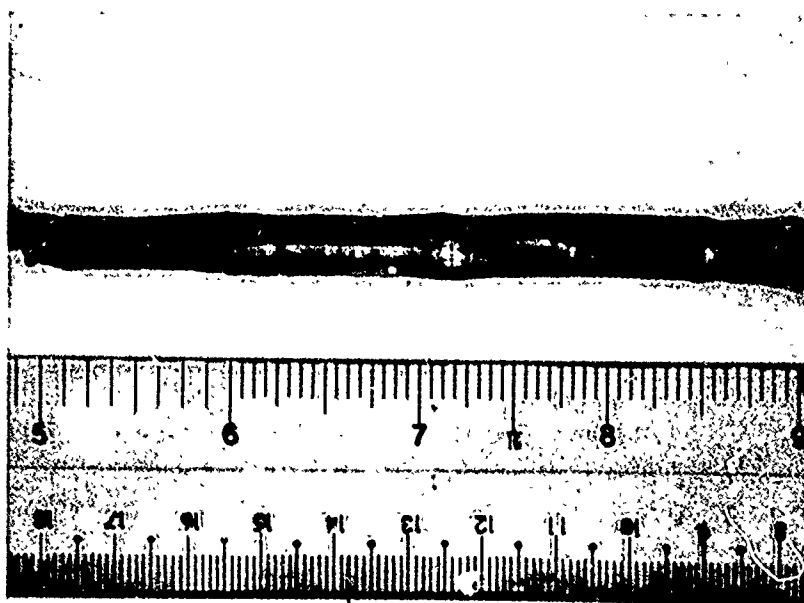


Figure 2: FZ-8 sandblasted to show grain structure.

information on the evolution of apparatus and procedure may be found in the previous report [1].

The major obstacle to the successful operation of encapsulated floating zone melting was to bring together consecutively the various successful individual procedures to produce an intact float-zoned ingot. We desired to make a significant number of floating zone passes in order to demonstrate that no practical limit exists to the number of passes which can be made. This goal has been successfully reached with the experiments producing ingots FZ-8 and FZ-9. Ingot FZ-8 is shown in Fig. 1. This ingot received six floating zone passes and has a maximum diameter of 8 mm. The grain structure of the ingot following sand-blasting and of a long-axis cross section are shown in Figs. 2 and 3, respectively. Ingot FZ-9 is shown in Fig. 4. This ingot received ten passes and has a maximum diameter of 10 mm. This ingot possessed a smaller grain structure than ingot FZ-8, as may be seen by comparing the sandblasted ingot and the cross section, Figs. 5 and 6, respectively, with Figs. 2 and 3. With the completion of these experiments, encapsulated floating zone melting can be considered successful for GaAs rod diameters up to one centimeter, at least from a mechanical standpoint.

A preliminary study of the effect of encapsulated float zoning on GaAs purity was described in the previous report [1] for ingot FZ-7. At that time, the presence of carbon as the dominant impurity was suspected. Some further measurements are described here, which make the previous interpretation suspect. Analysis by optical absorption spectroscopy shows

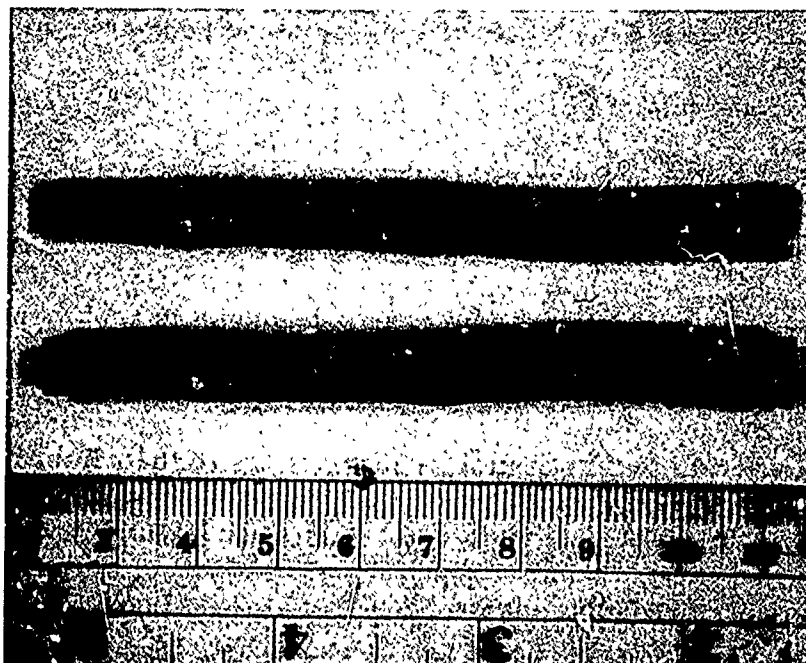


Figure 3: Sectioned FZ-8.

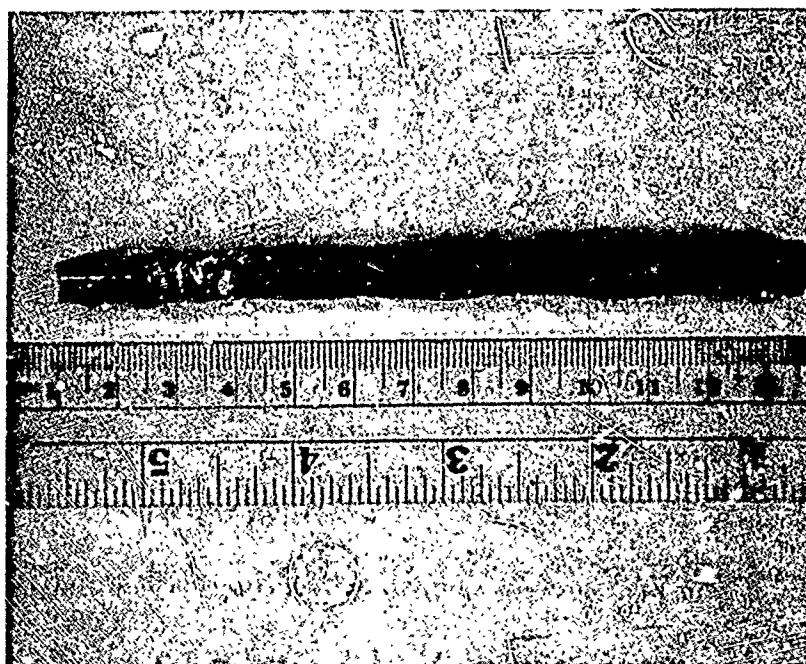


Figure 4: FZ-9 after 10 floating zone passes.

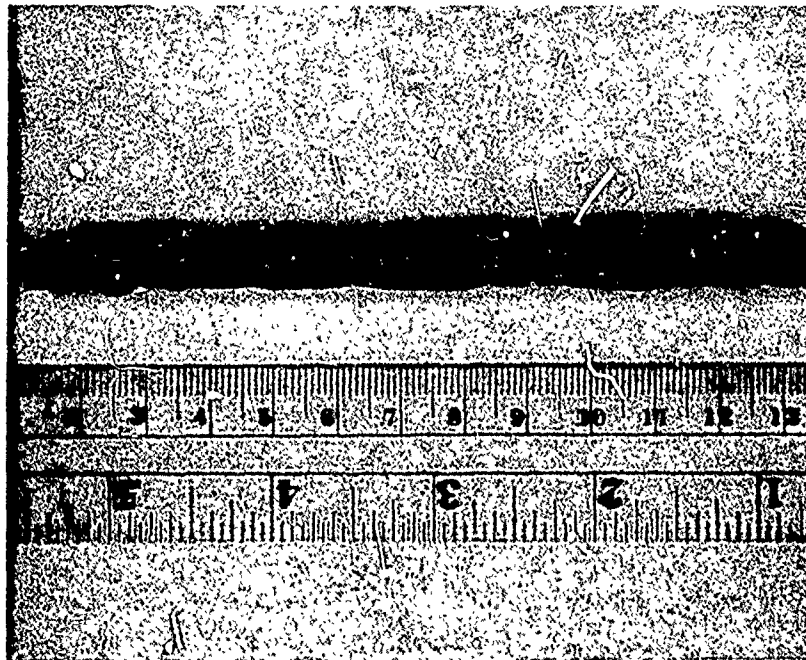


Figure 5: FZ-9 sandblasted to show grain structure.

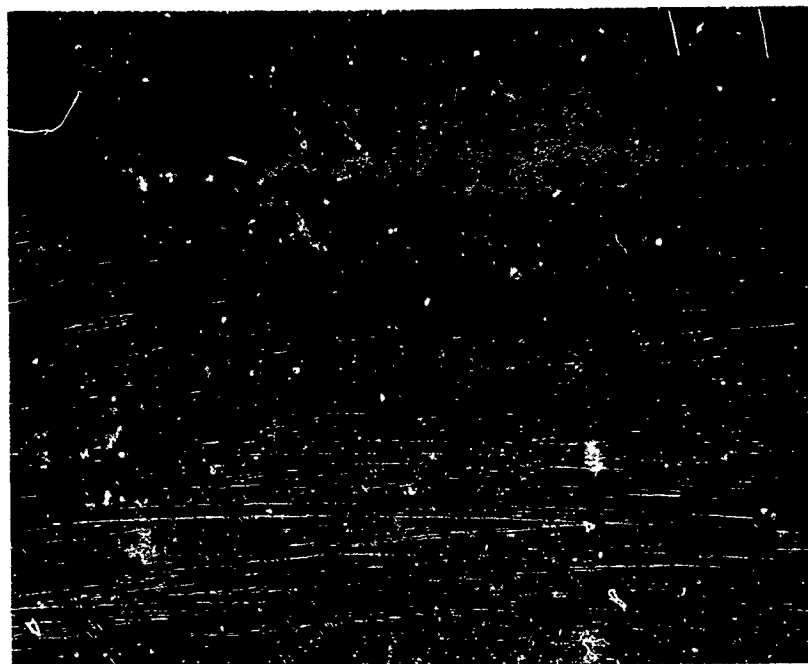


Figure 6: Sectioned FZ-9.

TABLE II

Summary of Elemental Impurity Analysis

Element	Factoral Increase	Final Concentration $\times 10^{15} \text{cm}^{-3}$
B	1000	44
Zn	0	150
In	10	11
Ni	10	9
Cr	10	4
Co, Ti	10	2
K, Ca	7	4
Cl, Ta	2-3	12
Al	2-3	4
Be, Mn, Fe, Mg, P	2-3	2

that carbon and boron impurity concentrations are below the detectability threshold for both the zoned ingot and a sample from the original Bridgman ingot from which the feed rod was taken. Although these thresholds are quite high for this method of analysis, the results are not insignificant, since carbon concentrations large enough to be observed have appeared in "as grown" ingots, as reported in Sec. I.A. Mass spectrometer analysis of impurity concentrations revealed that zinc was the dominant impurity in these samples, being present at a concentration of $1.5 \times 10^{17} \text{ cm}^{-3}$. This value is in good agreement with the hole concentration found from Hall measurements, 1.1 to $2 \times 10^{17} \text{ cm}^{-3}$. The mass spectrometer data gives no decrease in zinc concentration for the float zoned sample, whereas the Hall data does show a consistent trend of a decrease of $\sim 1/2$ in the carrier concentration. A factor of two difference for these independent measurements may be considered good agreement. Thus, the major impurity appears to be zinc with carbon playing only a minor role.

Further results of mass spectrometer analysis are shown in Table II. Samples from ingot FZ-7 and the Bridgman ingot from which the feed rod was taken are compared. The "final concentration" is that concentration obtained for the zoned material. Elements which were present in the same concentration in both samples (Zn excepted) are not listed. It is significant that for all cases where a difference existed the impurity concentration was higher after zoning than before. The results suggest that impurities from the boron oxide encapsulant or the fused

TABLE III

Hall Data for Ingots FZ-8 and FZ-9

Sample	Carrier Concentration cm^{-3}	Mobility $\text{cm}^2\text{volt}^{-1}\text{sec}^{-1}$
Feed for FZ-8	1.4×10^{18}	2000
FZ-8	1.6×10^{17}	3250
Feed for FZ-9	6×10^{15}	4400
FZ-9	3×10^{15}	----

silica tube were entering the GaAs.

Hall measurement data for ingots FZ-8 (six passes) and FZ-9 (ten passes) are shown in Table III. Hall mobilities listed are lower limits due to the difficulties in accurately measuring resistivity in polycrystalline GaAs. In some cases no resistivity measurements were possible. These data show a decrease of a factor of ten in carrier concentration for the case of feed material of high initial carrier concentrations ($\sim 10^{18} \text{ cm}^{-3}$). When the starting material was high purity undoped GaAs ($\sim 5 \times 10^{15} \text{ cm}^{-3}$), the results were less conclusive. The slight decrease in carrier concentration may represent actual purification -- the movement of compensating impurities. It was not possible to measure Hall mobility in this case. The results do indicate that the problem of contamination from boron oxide may not be as serious as the first mass spectrometer data suggest. More complete interpretation of the Hall data for these two ingots awaits comparison with results of the mass spectrometer analysis underway at the Battelle Columbus Laboratories. The diameter control shown for ingots FZ-8 and FZ-9 was quite good, considering that manual control of the radio frequency generator was used. Both ingots showed some mass transport in the direction of zone motion. A tendency for the number of grains to increase with the number of zone passes was also noted.

Considerable effort has been placed on the preparation of GaAs feed material using horizontal Bridgman growth techniques during this report period. Bridgman grown material need only be homogeneous and free of voids for use in some floating zone experiments, whereas in

other cases, low impurity concentrations are also necessary.

Prereacted "scrap" GaAs was melted down to ingot form in the former case, while Ga and As of semiconductor quality were reacted in the latter. A half-dozen Bridgman ingots have been grown for use as floating zone feed rods. At present we are developing techniques for horizontal Bridgman growth of much larger diameter GaAs ingots (2.5 cm O.D., 400 gm) for encapsulated float zone use.

The success of the experiments which produced ingots FZ-8 and FZ-9 shows that the mechanics of encapsulated float zone melting can be considered successfully proven. Of importance in upcoming work will be to establish the maximum diameter GaAs feed rod which can be successfully zoned using a boron oxide encapsulant. Apparatus has been constructed for the preparation and use of GaAs feed rods of 1.25, 1.50, 1.75, and 2.00 cm diameter. A system to provide stability to the induction heater's power output is essential to successful zoning of large diameter ingots. In the past, manual control of the power output was adequate. However, as the maximum possible GaAs feed rod diameter is approached, power stability will become increasingly important. Optimum stabilization would be achieved through use of a tuned radio frequency generator. However, difficulties have been experienced during previous attempts to tune the unit now available. A second possibility is to achieve power stability through a feedback loop in the generator control circuitry.

A second area in which work is in progress is the determination of the effect of encapsulant (boron oxide) purity on the ultimate purity of

GaAs subjected to repeated floating zone passes. Experiments using a boron oxide of significantly higher purity (.999% and .9999%) than that now widely used for crystal encapsulation (.995%, BDH Optran Grade) are planned. Necessary chemicals, GaAs feed rods, and silica have been prepared and the experiments are ready to begin.

C. Travelling Heater Method

Vincent Yip

1. Influence of Growth Parameters on THM Growth of GaAs

Our THM growth technique was described previously [1]. A systematic study of the influence of the difference growth parameters on GaAs growth was conducted as summarized in Table IV. The most important parameter which determines the crystallinity and perfection of the THM grown crystal seems to be the length of the Ga zone relative to the heater length. The heater length used throughout was 1 cm with a 1 cm diameter ampoule. The equilibrium length and position of the Ga zone at 980°C heater temperature were determined for 0.3, 0.55, 0.7, 1.0 and 1.55 cm initial Ga zone lengths, as shown in Figure 7. It was found that the bottom GaAs-Ga interface was convex when the zone was smaller than the effective heater length (which is greater than the 1.0 cm physical length) and concave when larger (as in the 1.55 cm zone). When the starting zone was much smaller than the heater, as in the case of the 0.3 cm zone, a GaAs bridge formed between the seed and feed in the colder center portion of the zone, thus rendering it unusable for THM

TABLE IV. Summary of Recent GaAs Travelling Heater Experiments (July 1972 - December 1972)

Run THM #	Heater Temp.	Original Seed Length (cm)	Original Ga Zone Length (cm)	Original Feed Length (cm)	Lowering Rate (mm/day)	Results
73	980°C	Self Seed	0.55	2.5 cm	4.0	Feed material was THM #78, the result of one Ga zone pass on GF-30. Two cm growth resulted from this second Ga zone pass.
76	980°C	Self Seed	0.55	2.0 cm	4.0	THM #73 was subjected to a third Ga zone pass. A 1.5 cm crystal was grown. The final 0.5 cm was single crystalline.
89	980°C	1.0	0.55	3.8	2.22	Growth of 2 cm completed before run was terminated because of power shut down. Crystal contained a $\langle 111 \rangle$ twin. No inclusions were observed. It appeared that 2.22 mm/day was close to the critical rate for single crystal growth at 980°C.
83	850°C	1.0 $\langle 111 \rangle$ Ga	0.55	2.0	0.5	Ga inclusions were present, as well as small crystals scattered in the grown crystal.
79	1100°C	Self Seed	0.55	3.8	20	Good quality, inclusion free crystal.
71	980°C	0.6 cm $\langle 111 \rangle$ As	2.578 g Ga 0.001 g Te	3.8	1.5	2.0 cm single crystal with a small polycrystal in the second cm.

TABLE IV (continued)

Run THM #	Heater Temp.	Original Seed Length (cm)	Original Ga Zone Length (cm)	Original Feed Length (cm)	Lowering Rate (mm/day)	Results
72	980°C	1.0 cm <111> As	2.80 g Ga no dopant	3.5	1.5	95% single crystal. Three tiny strip-like (111) twins nucleated near the circumference and grew into the center of the crystal at 70.5° to <110>.
81	930°C	0.6 cm <111> Ga	2.59 g Ga 0.001 g-Zn	2.0	1.5	Seeding poor. Polycrystalline from 0.5 cm to 1.5 cm.
84	980°C	1.0 cm <110>	3.39 g Ga 0.012 g Cr	2.0	1.5	After 0.3 cm growth in the <110> direction a (111) twin developed from the side and grew preferentially for the remaining 1.5 cm.
86	980°C	1.0 cm <110>	2.4 g Ga 0.036 g Cr	2.0	1.0	Completely single.

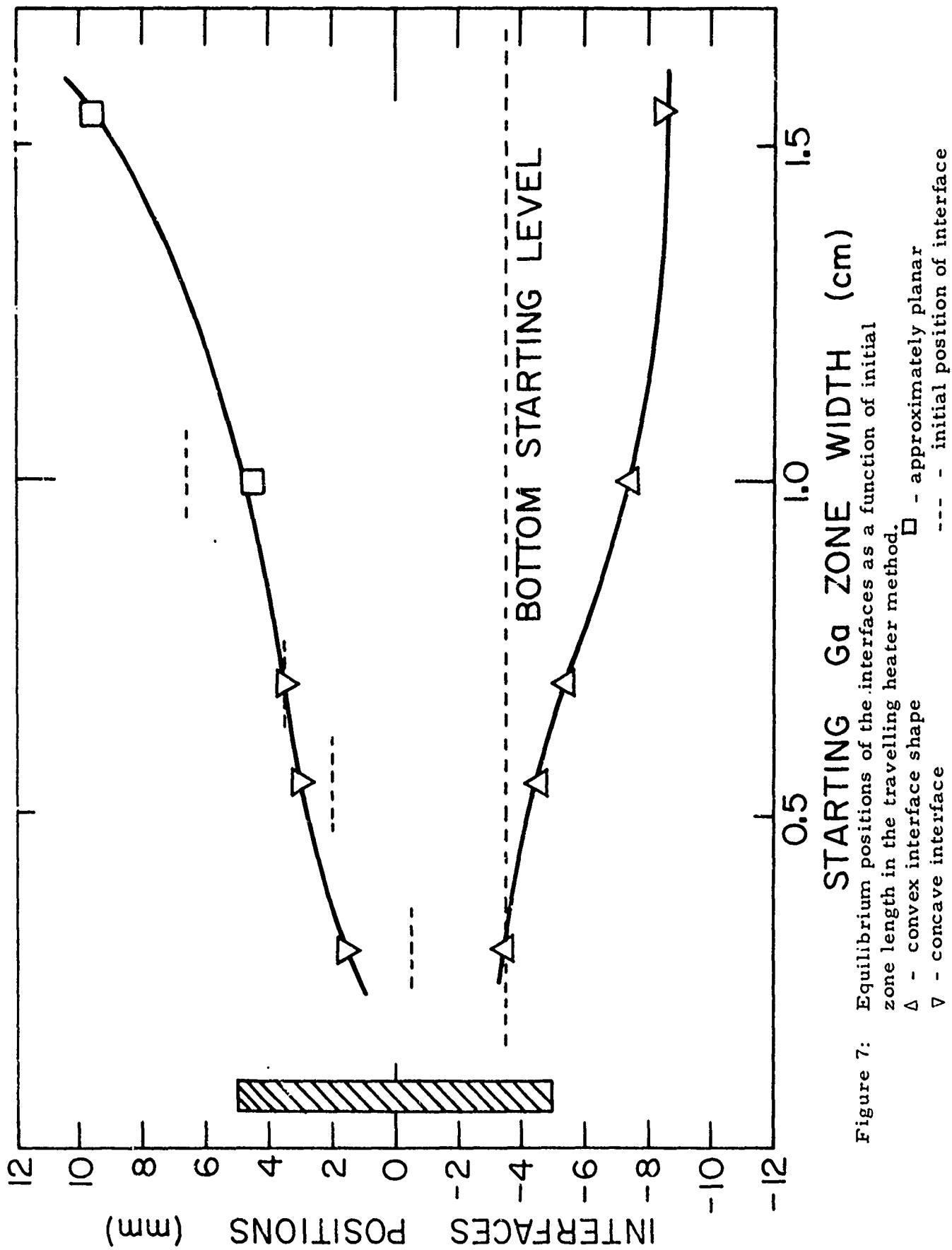


Figure 7: Equilibrium positions of the interfaces of the Ga zone width as a function of initial zone length in the travelling heater method.

Δ - convex interface shape
 \square - concave interface shape

\square - approximately planar

--- - initial position of interface

growth. Identical ampoules were prepared with different starting Ga zone lengths and growth was performed at 980°C with a 1.5 mm/day lowering rate. Figure 8 shows sections of the resultant crystals. The strong differences are evident. The crystals grown with convex solid-liquid interfaces (as in the cases of 0.55 and 0.70 cm zones) appeared to have fewer grains and the grain boundaries tended to grow out. The near-flat interface of the 1.0 cm zone was responsible for the length-wise propagation of grains in THM-62. In THM-41, in which the zone was larger than the heater and the growth interface concave, many grains nucleated at the wall and grew inwards. Traces of trapped Ga were also found in the center of the crystal. It seemed that to obtain good single crystal growth, the ratio of the length of the Ga zone to the heater length should be greater than 0.5 but less than 1.0.

An important phenomenon in THM growth was also detected and studied. It was found that as growth took place, the positions of the interfaces shifted relative to the heater because of the gradual change in heat transfer conditions. This shift was especially significant at the beginning and the end of the growth runs, producing an accelerated growth which should be taken into consideration in THM growth. Figures 9 and 10 show this effect for 0.55 cm and 1.55 cm zones.

The influence of temperature and lowering rate were also investigated. As will be discussed in the next section, the actual growth temperature inside the Ga zone was about 60° to 80°C lower than the measured maximum heater temperature. It was found that it was

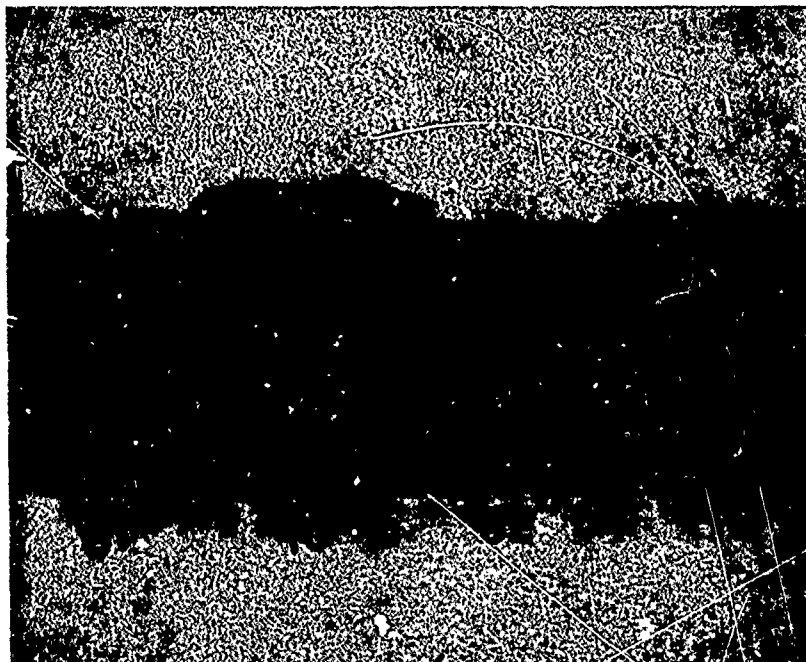


Figure 8: Travelling heater GaAs grown at ~ 1.5 mm/day with different initial Ga zone lengths.

THM-61 - 0.55 cm

THM-40 - 0.70 cm

THM-62 - 1.0 cm

THM-41 - 1.55 cm

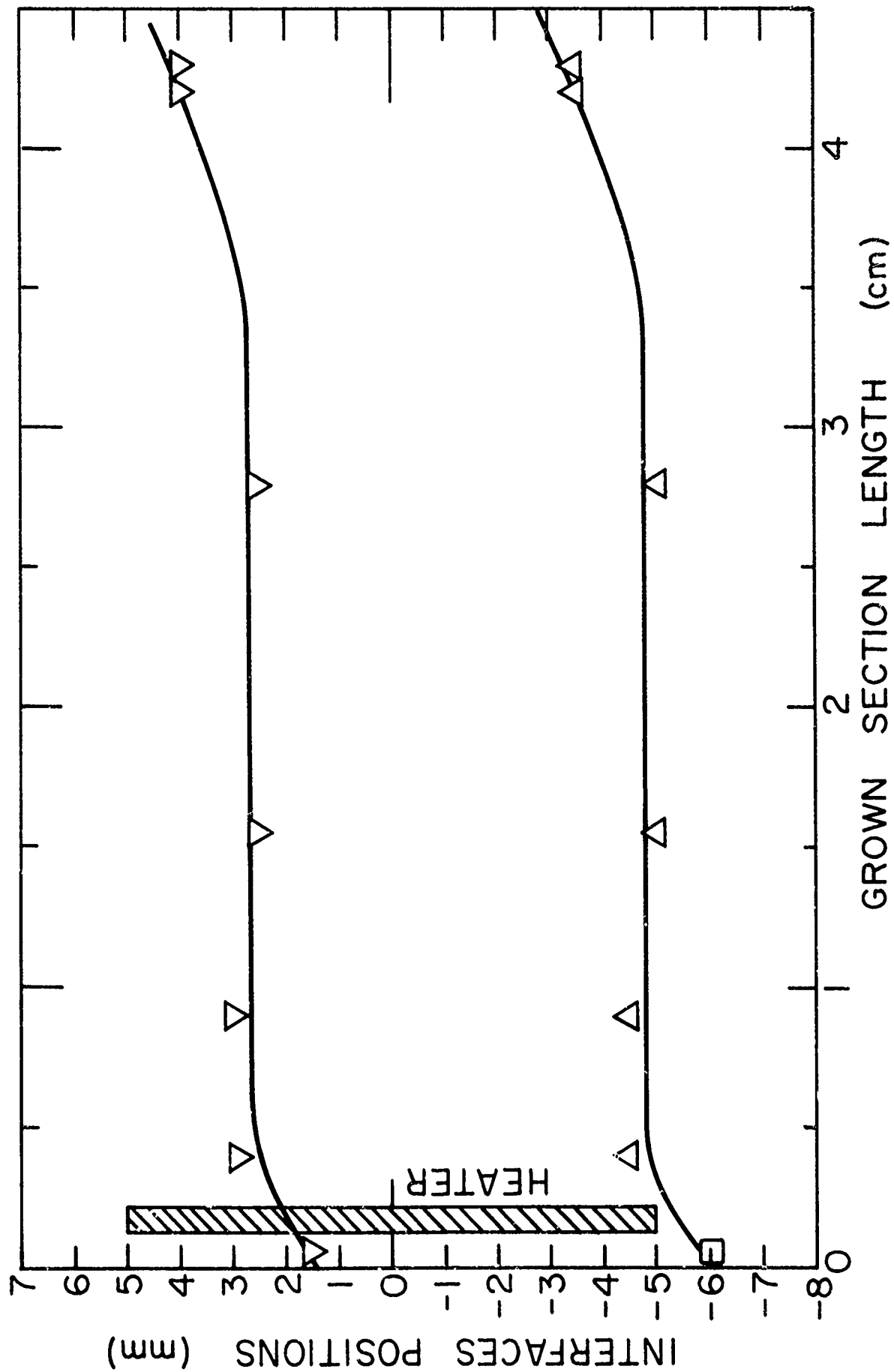


Figure 9: Equilibrium positions of the interfaces as a function of the length of solid below the zone. 0.55 cm initial Ga zone length.

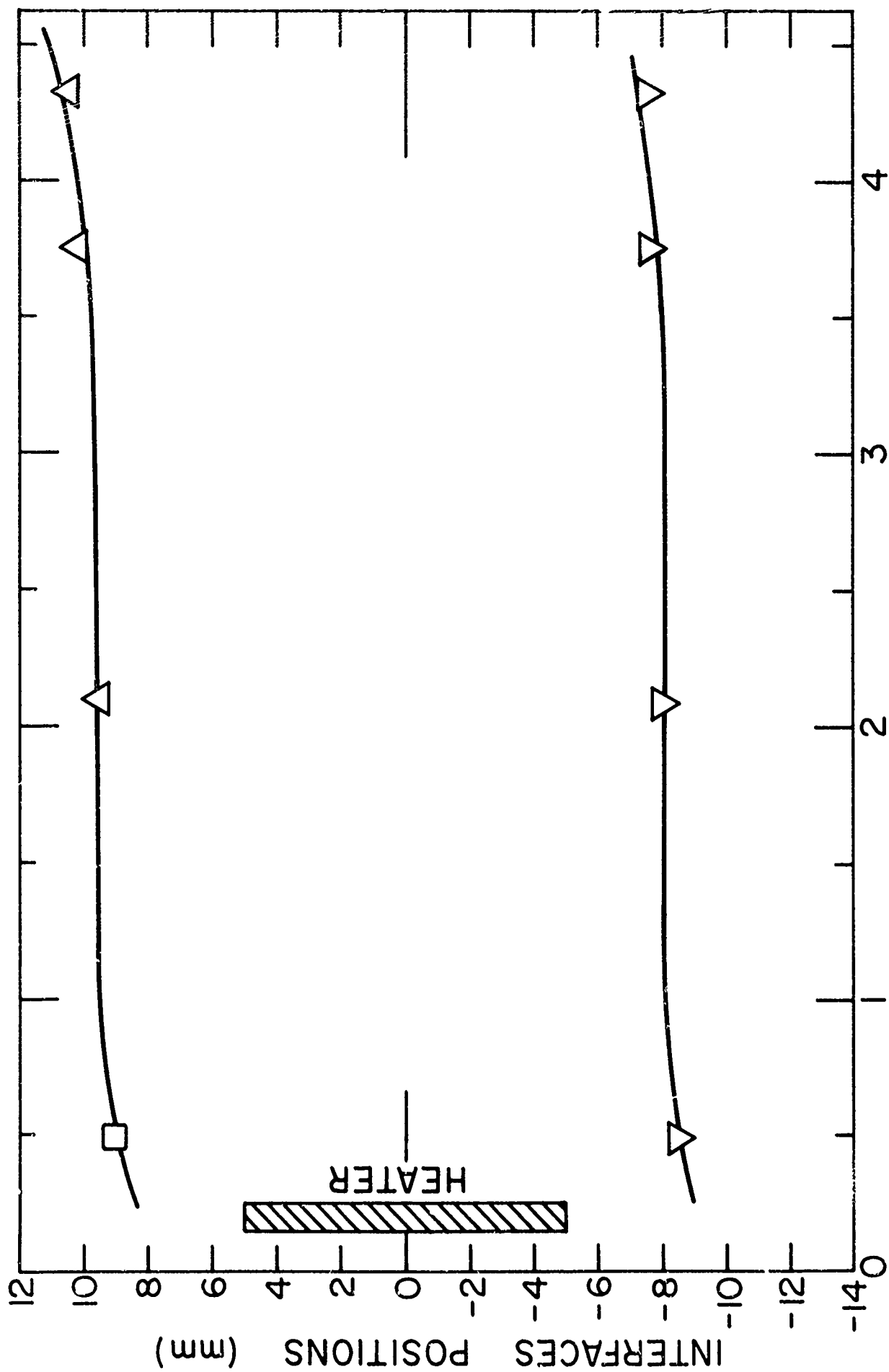


Figure 10: Equilibrium positions of the interfaces as a function of the length of solid below the zone. 1.55 cm initial Ga zone length.

impossible to grow good crystals at a heater temperature of 800°C . At 850°C growth at 0.5 mm/day produced fair quality crystals, while speeds greater than 2.0 mm/day produced crystals with inclusions. A convenient and sufficiently high heater temperature was 980°C . Figure 11 shows the crystals grown at this temperature with a 0.55 cm Ga initial zone and four different growth rates. At a heater temperature of 1100°C , it was possible to grow inclusion free, good quality crystals at growth rates of 20 mm/day. It appears that at a heater temperature of 980°C the critical lowering rate for inclusion-free single crystal growth was about 2.22 mm/day. The precise rate could not be determined because the crystallinity also depends on other factors which are not always controllable.

These studies on the effects of the different parameters produced a comprehensive understanding of the THM growth process and enabled the determination of these optimal conditions for growth of GaAs by 1 cm diameter THM: optimal conditions for seed of 1 cm length, feed longer than 2 cm, initial Ga zone 0.55 cm to 0.7 cm, heater temperature of 980°C and a lowering rate of about 1.5 mm/day.

2. Temperature Profile Measurement inside GaAs Crystal during THM Growth

After overcoming a number of technical difficulties, the temperature profile inside a GaAs crystal was measured during a THM growth run over 13 1/2 days at a lowering rate of 1.5 mm/day. Apparently no appropriate insulation or coating could prevent attack of a

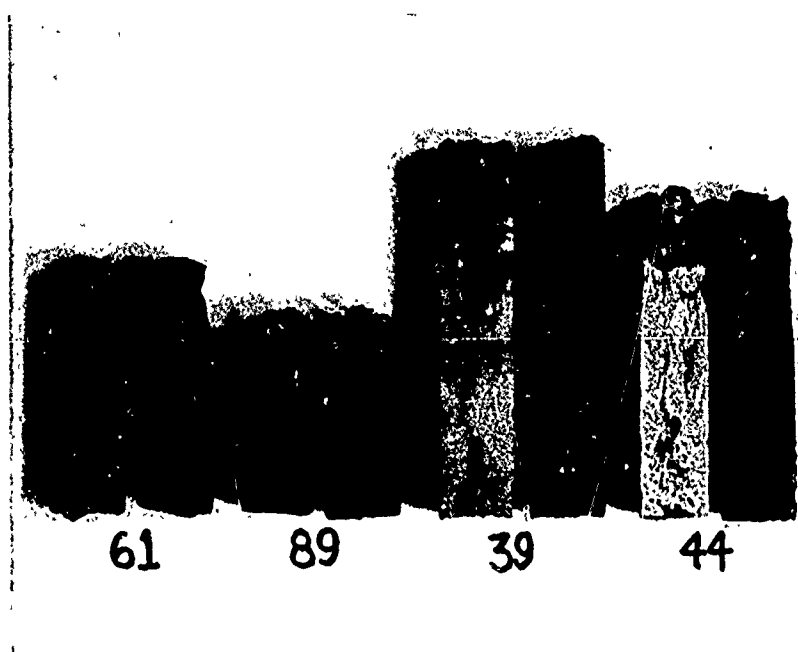


Figure 11: Sectioned THM GaAs grown with a heater temperature of 980°C at four different lowering rates,

THM-61 - 1.5 mm/day
THM-89 - 2.22 mm/day
THM-39 - 4.44 mm/day
THM-44 - 6.66 mm/day

thermocouple by arsenic and molten gallium at the operating temperature. This temperature measurement was accomplished by using a 3 mil Pt - Pt 10% Rh thermocouple, the leads to which were inserted in a two-holed 1/32 in. dia. alumina tube. This in turn was inserted into a long, thin-walled (.012" thick) quartz well which was welded and sealed to the quartz ampoule. This fit into a 0.14 cm dia. 2.6 cm deep hole drilled in the center of a GaAs feed rod of diameter 1.02 cm. Details of the experimental setup are shown in Figure 12.

The thermocouple output was continuously recorded on a chart recorder using a second Pt- Pt 10% Rh thermocouple immersed in an ice-bath as a reference junction. The result is plotted in Figure 13, together with the heater temperature profile measured with a thermocouple placed outside an identical ampoule. The measured "crystal temperature" cannot be considered and analyzed quantitatively because the measurement conditions were not ideal for great accuracy. Several features can be explained by taking into account errors introduced by the quartz wall separation and other factors. One important observation is that the temperature within the gallium zone was constant at 931°C , giving a difference of 82°C from the measured maximum heater temperature of 1013°C outside the ampoule. Another important piece of information obtained was the temperature gradient at the bottom GaAs-Ga growth interface, which was estimated to be around $5\text{-}10^{\circ}\text{C}/\text{mm}$. When the temperature measurement was terminated at point F, about 6 mm below the bottom interface, the heater power was turned off and

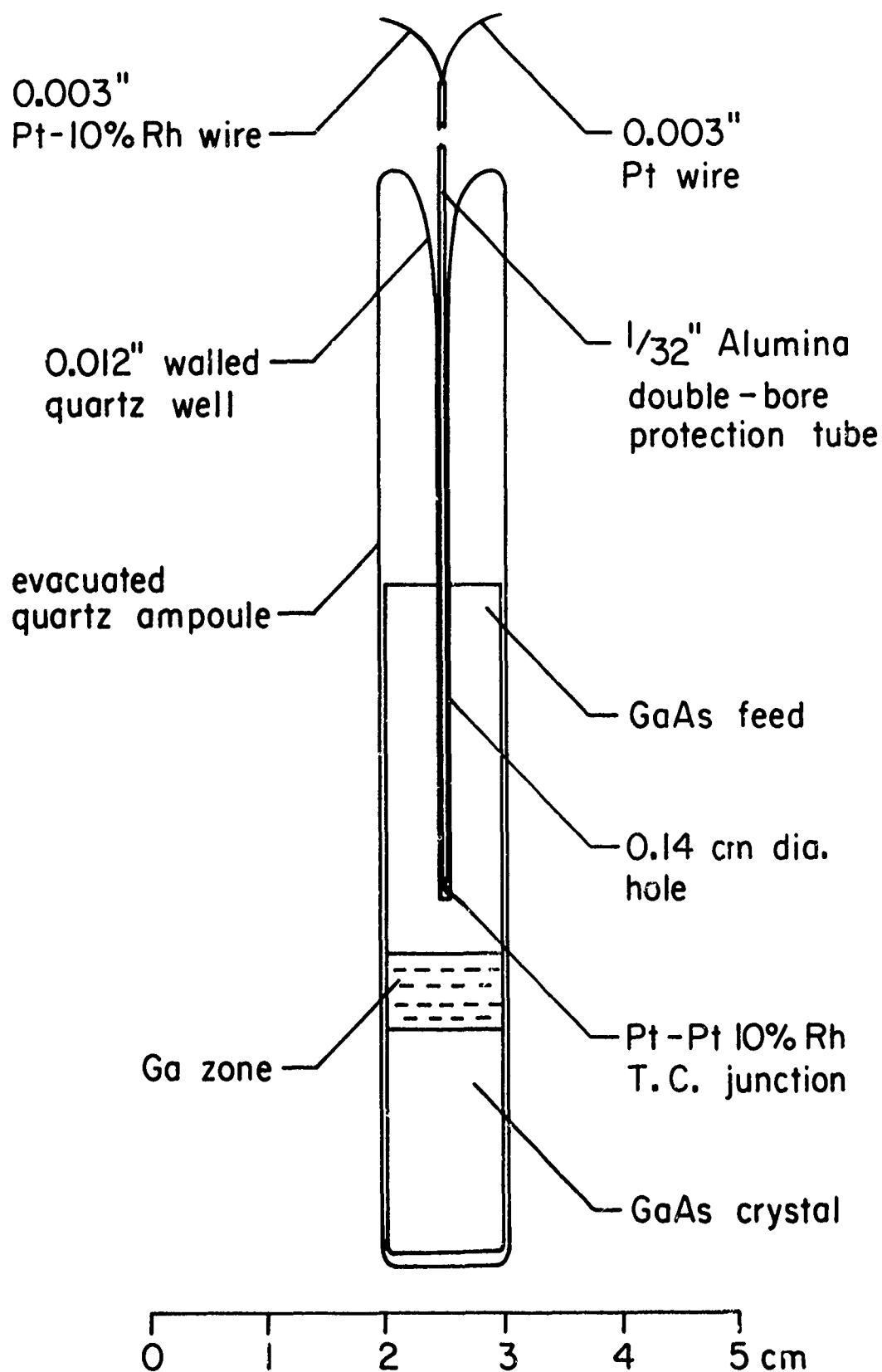


Figure 12: Assembled ampoule for measurement of temperature profile during THM growth.

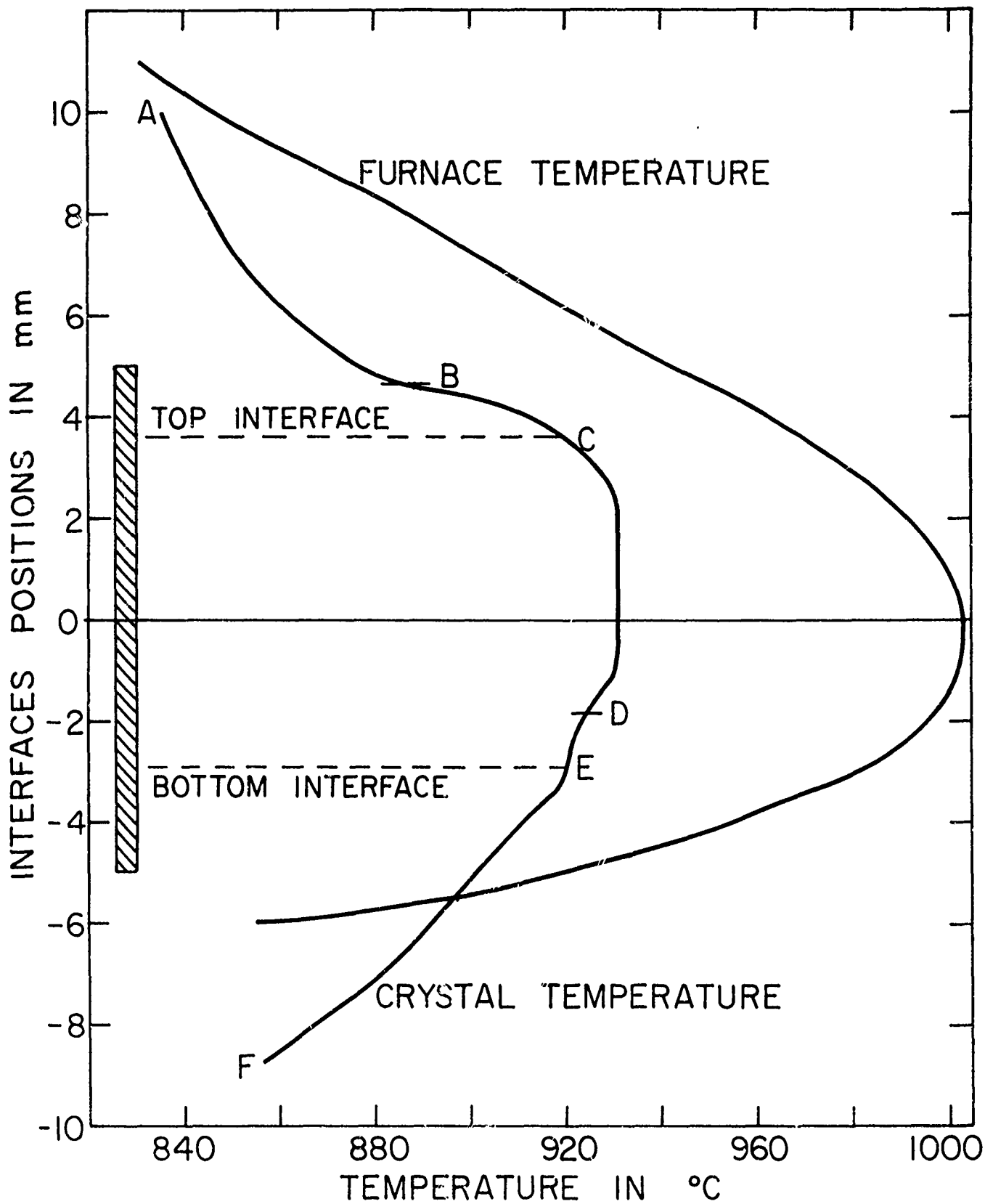


Figure 13: Measured temperature profiles inside and outside THM growth ampoules.

the temperature was recorded with the ampoule stationary. The temperature dropped rapidly from 798°C to 335°C in the first 30 minutes and afterwards decreased at a constant rate of about 1°C per minute.

3. Seeding and Impurity Doping in THM Growth of GaAs

After the different aspects of THM growth of GaAs were investigated and understood, six single crystals were successfully grown under the chosen optimal conditions of 980°C heater temperature, 0.55 cm Ga zone length and $\sim 1.0 - 1.5$ mm/day lowering rate. See Figures 14 and 15 for example. The seeding directions used were $\langle 111 \rangle \text{Ga}$, $\langle 111 \rangle \text{As}$ and $\langle 110 \rangle$. The crystals were not intentionally doped (#72 and #83) or were doped with Te (#71), Zn (#81), and Cr (#84 and #86). In all cases except one, seeding and growth were very satisfactory. In THM-72 (Figure 16), three tiny strip-like $\langle 111 \rangle$ twins, spaced 120° apart, nucleated near the circumference and grew into the center of the crystal at an angle of 70.5° to the (110) seeding face. From the mass spectrometric data of THM-71, grown with 1 mg of Te in 2.578 g of Ga, the Te concentration in the solid GaAs was calculated to be 0.784×10^{16} atoms/c.c., giving a Te segregation constant of about 1.0×10^{-3} for growth from a Ga solution at the estimated growth temperature of about 910°C . Such estimated K values would be lower than the true values, since some dopant inevitably evaporated from the zone and condensed at the colder part of the sealed quartz ampoule away from the hot Ga zone. Samples of these crystals grown under controlled seeding and

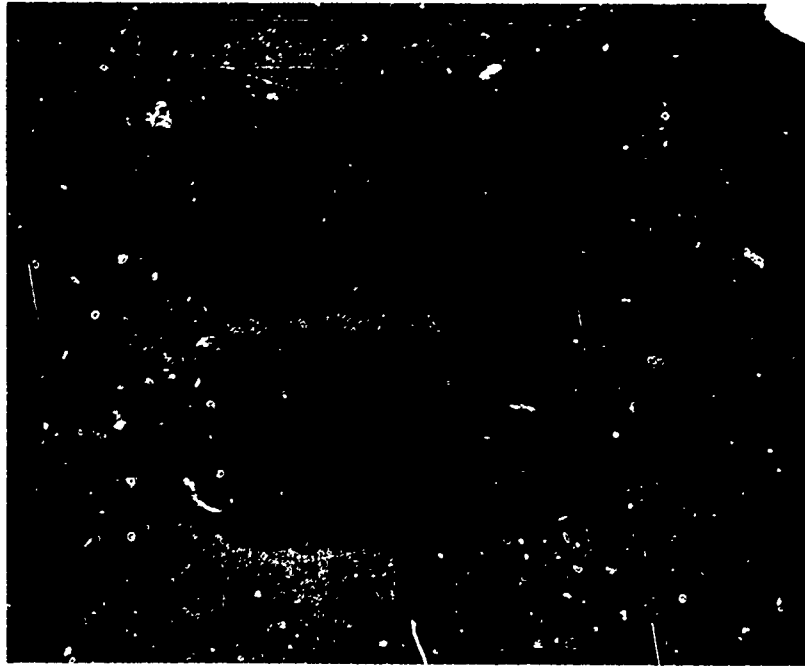


Figure 14: THM-71. Te doped and grown in $\langle 111 \rangle$ As.
 THM-86. Cr doped and grown in $\langle 110 \rangle$.

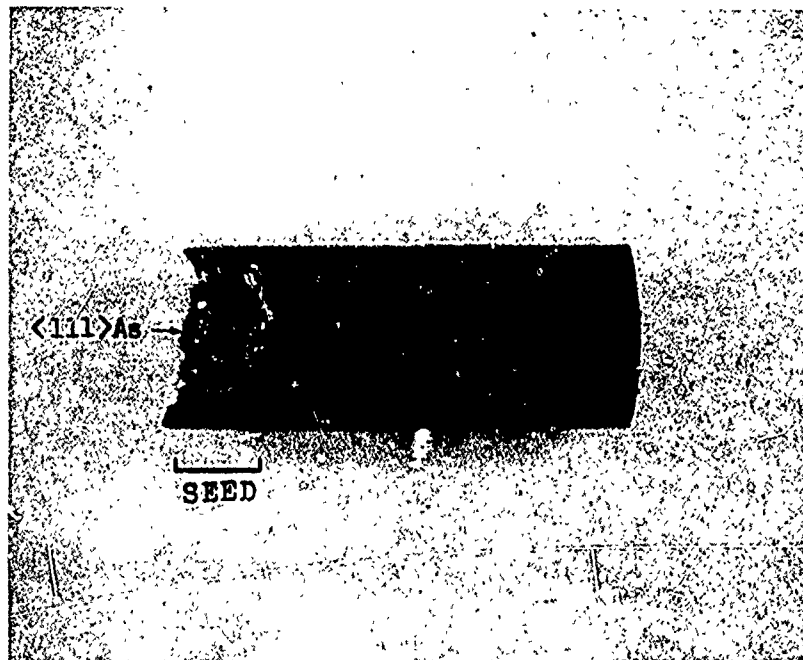


Figure 15: THM-71. Te doped and grown in $\langle 111 \rangle$ As.

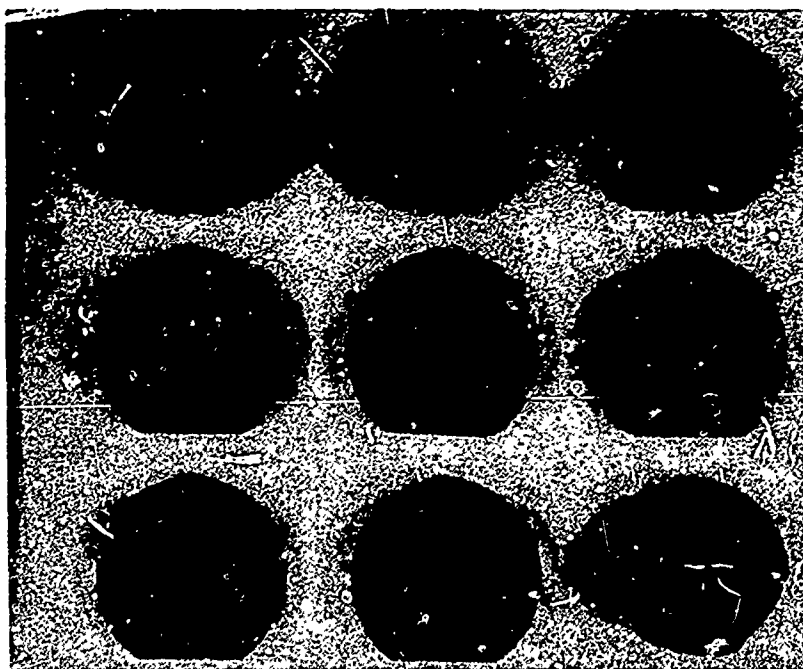


Figure 16: Twin formation and propagation in THM-72 GaAs grown in the $\langle 110 \rangle$ direction.

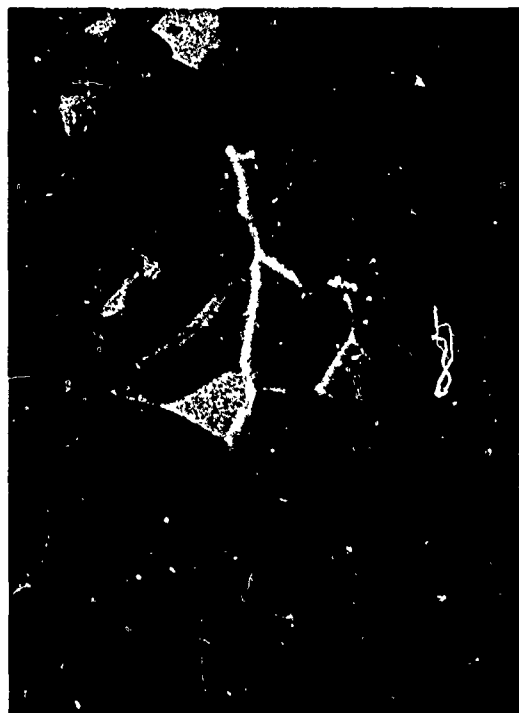
(Above)

(111) Ga etch pits on THM-72 as a function of distance from the seed X.

(Opposite Page)



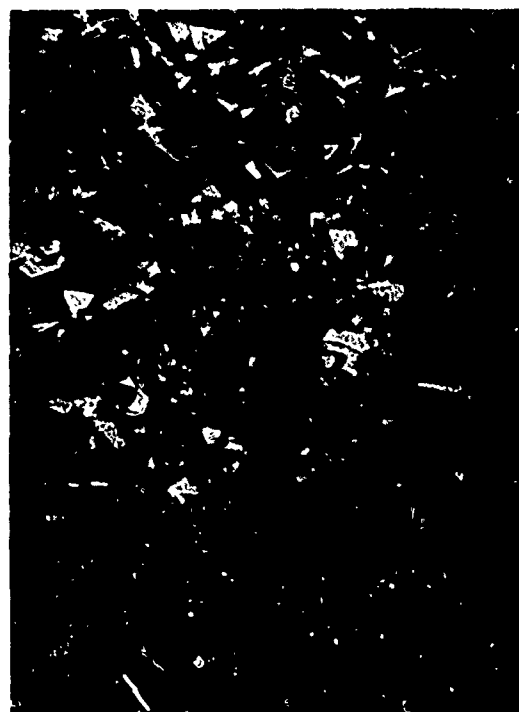
Slice 1: 0 mm



Slice 10: 19 mm

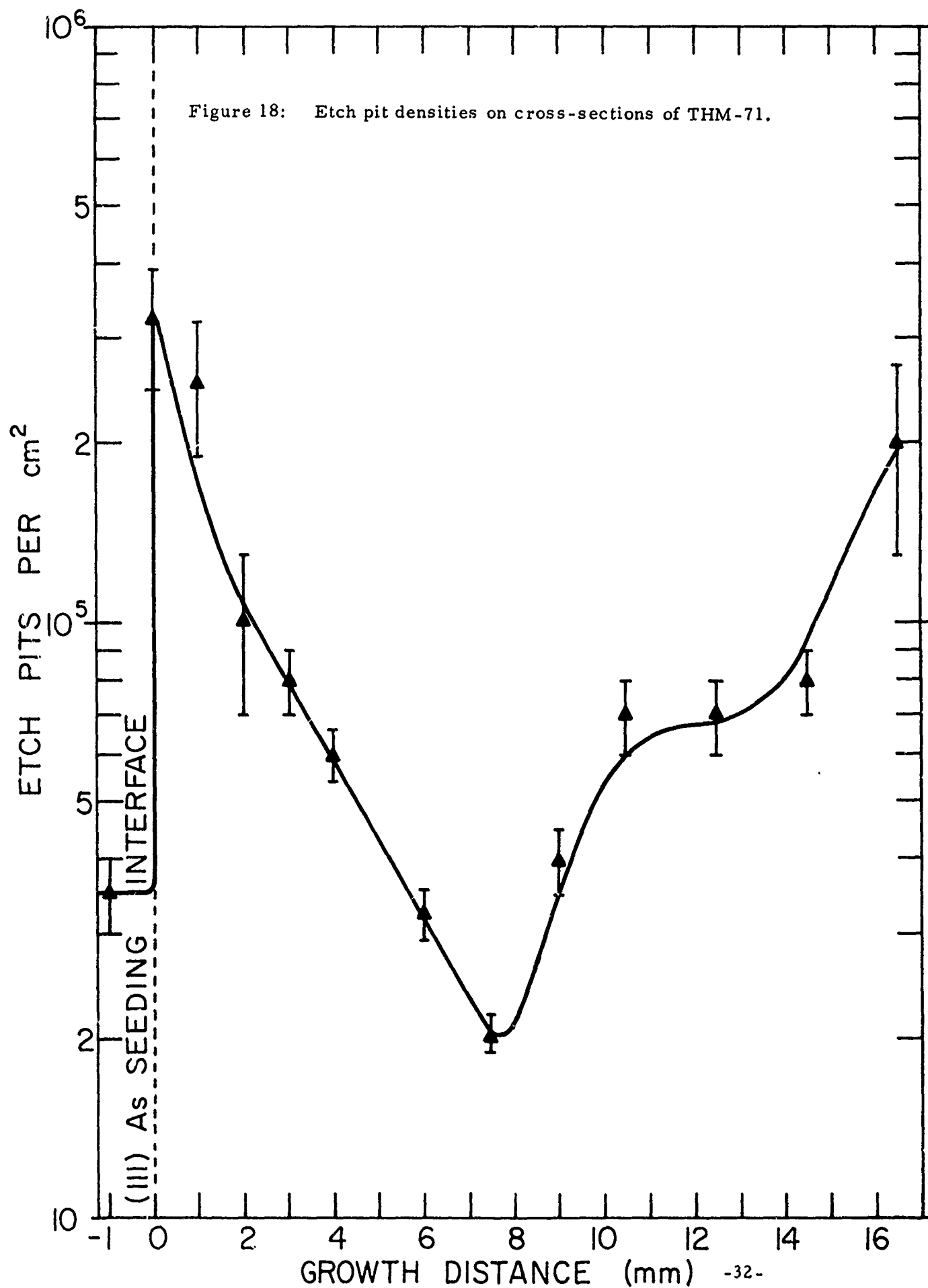


Seed Slice



Slice 6: 8mm

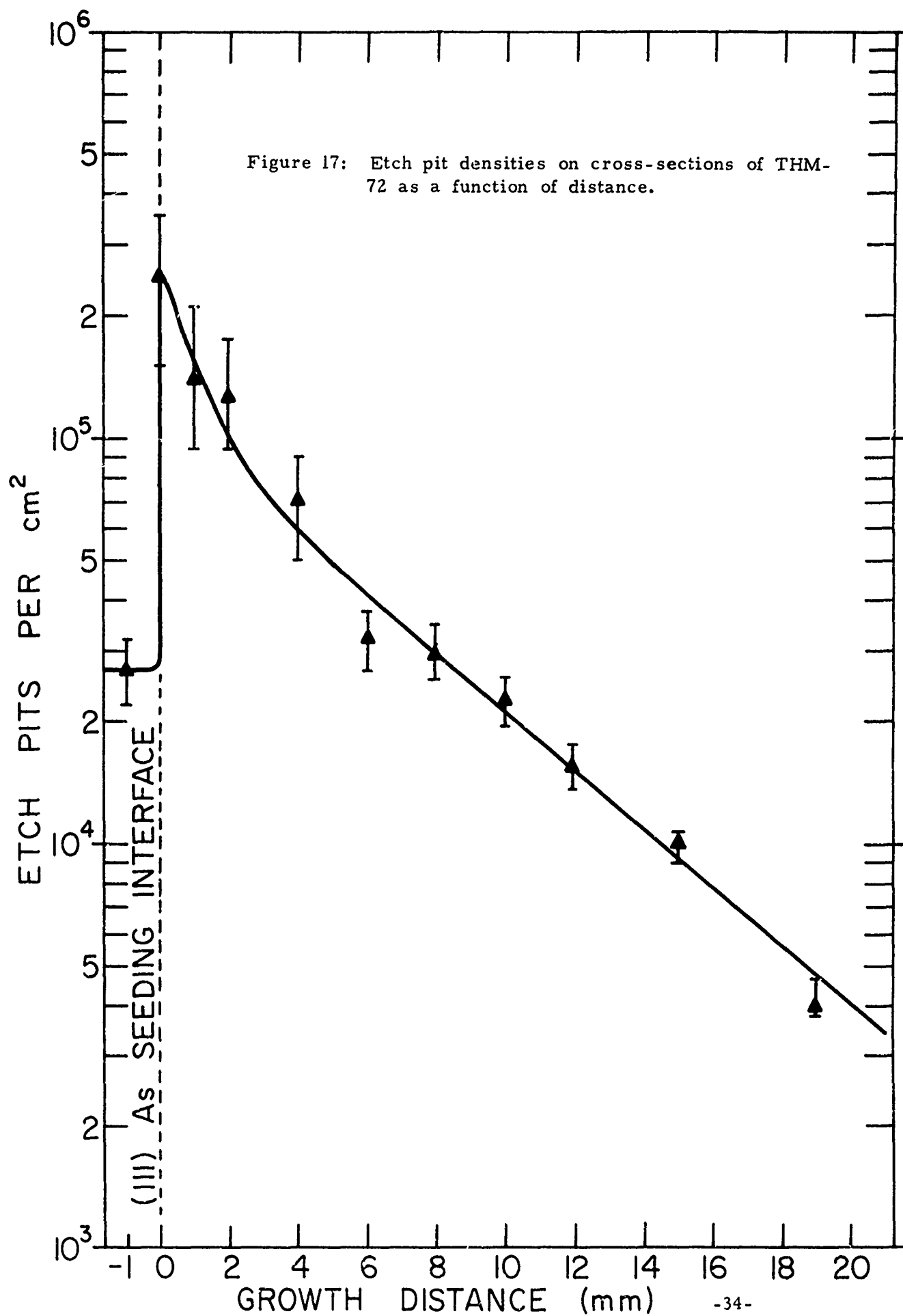
Figure 18: Etch pit densities on cross-sections of THM-71.



doping conditions were submitted for electrical measurements such as Hall, C-V and C-W measurements. The Cr-doped samples THM-84 and 86 were submitted for infrared absorption studies.

4. Dislocation Propagation during THM Growth of GaAs

In earlier studies of the effect of zone length on the growing interface shape, it was shown conclusively that a zone smaller than the heater (such as the 0.55 cm Ga zone used in all the later controlled seeded growths) would produce a slightly convex solid-liquid growth interface, which should have tended to "grow out" and eliminate dislocations as growth proceeded. Etch pits on (111) Ga were developed and counted on cross sections of the crystals THM-71 and THM-72, seeded in the $\langle 111 \rangle$ As direction. The results are shown in Figures 16, 17 and 18. For THM-72, the etch pit density increased from 0.5×10^4 per cm^2 to 1.0×10^5 per cm^2 at the seeding interface and then decreased approximately exponentially by two orders of magnitude to 0.3×10^3 per cm^2 after only 2 cm of growth. This dislocation elimination was probably enhanced by the convex growth interface. The run THM-71 was terminated by rapidly pulling the ampoule from the furnace, thus quenching to room temperature rather than leaving the ampoule in the furnace and turning the heater off to allow relatively slow cooling, as in run THM-72. The study on the resultant dislocations in the crystal showed that there was the same sudden increase in dislocations at the seeding interface and the exponential decrease afterwards, as shown in Figure 18. However, the etch pit



density increased by one order of magnitude from 7.5 mm to 16.5 mm. This was probably caused by thermal strain on the part of the crystal near the heater, which underwent a large temperature drop during the quenching process.

Crystals THM-84 and -86, seeded in the $\langle 110 \rangle$ direction and doped with Cr, were sliced longitudinally on the (111) plane and dislocation etch pit counts made along the length of the crystals. As shown in Figure 19, the etch pit density did not change appreciably at seeding and remained approximately at a constant value of around $2 - 3.5 \times 10^4$ per cm^2 . These results suggest that the axial thermal stresses were significantly greater than radial thermal stresses.

5. Segregation in THM Growth

The configuration of THM is similar to that of zone melting, except that a solvent zone replaces the molten zone. There should be a purification effect in THM growth and the factor should be greater than for melt growth since the growth temperature is considerably lower (the segregation constant of most impurities is much smaller in growth from Ga solution than growth from GaAs melt). Mass spectrometric analyses of feed GaAs and THM crystals grown from them bore out this fact, as shown in Table V. Crystal THM-72 was grown from seed and feed rods ground from Czechralski ingot CZ-41 using a zone of 2.8 g Ga of six 9's purity. There appeared to be a reduction in the amount of B, K, Cr and Fe. The purification in crystal THM-76, which was the result

Figure 19: Etch pit densities on longitudinal slices of THM-84 and THM-86.

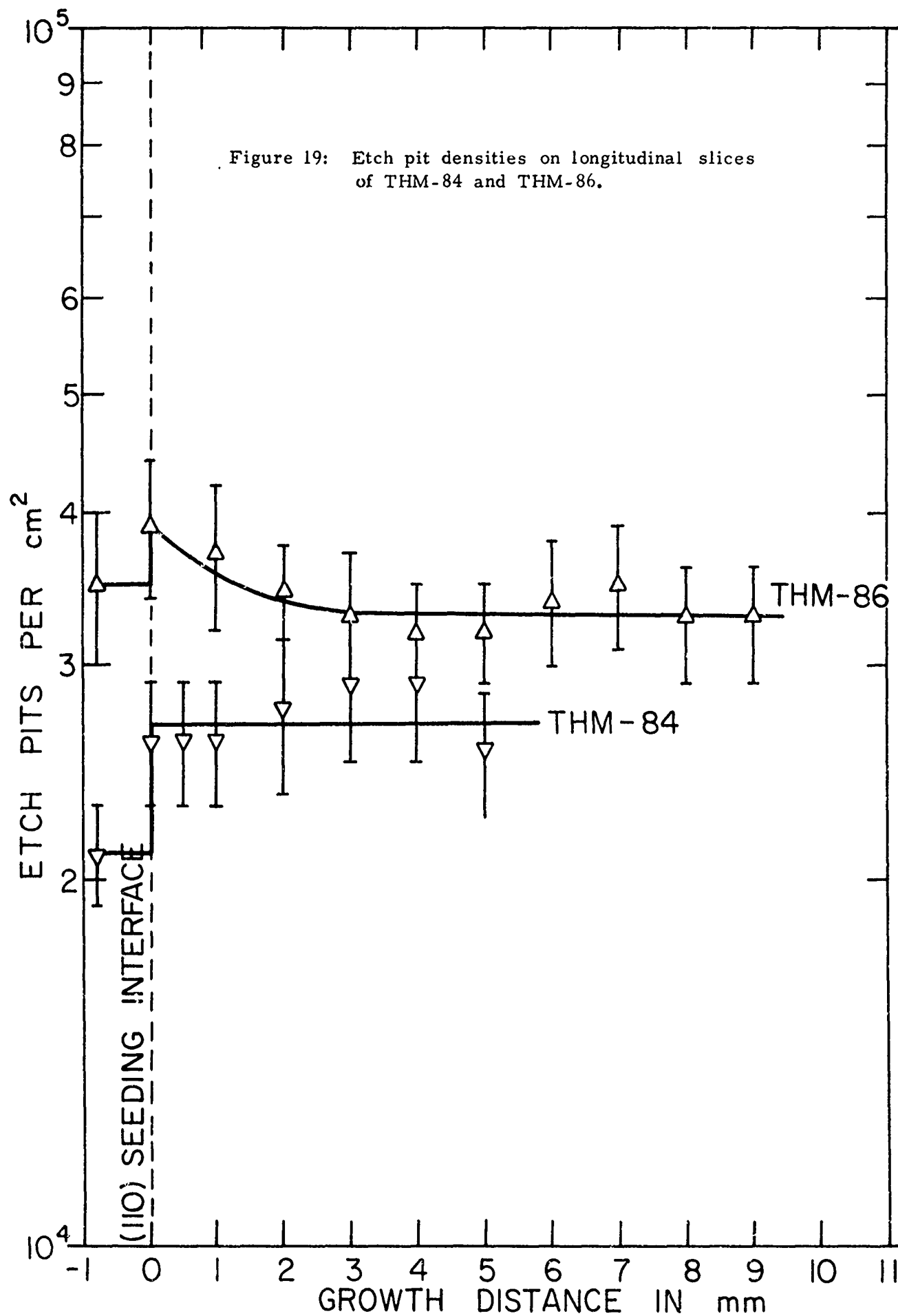


TABLE V

Mass Spectrometric Analyses of Feed Rods and THM
GaAs Grown from Them

<u>Element (ppmw)</u>	<u>Feed (CZ-41)</u>	<u>Crystal (THM-72)</u>	<u>Feed (GF-30)</u>	<u>Crystal (THM-73)</u>
Be	≤ 0.004	≤ 0.004	0.04	< 0.002
B	0.005	0.003	0.05	< 0.003
F	< 0.1	< 0.1	< 0.3	< 0.1
Mg	0.03	0.03	< 0.1	≤ 0.03
Si	< 1	< 1	0.7	0.6
K	< 0.2	0.1	0.06	0.03
Cr	0.1	< 0.02	< 0.03	< 0.01
Mn	< 0.02	< 0.02	< 0.02	< 0.01
Fe	0.4	0.07	0.2	1
Co	< 0.01	< 0.01	0.03	< 0.01
Ni	< 0.04	< 0.04	0.1	< 0.02
Cu	< 0.03	< 0.03	0.6	< 0.02
Zn	0.1	0.1	0.2	< 0.02
Sn	< 0.1	< 0.1	0.1	< 0.05
Te	< 0.05	< 0.05	< 0.06	< 0.06
Pb	< 0.06	< 0.06	0.6	< 0.06

TABLE VI. Summary of Travelling Heater Experiments on $\text{Ga}_{1-x}\text{In}_x\text{Sb}$

Run THM -	Heater Temp.	Seed	Original Zone Composition	Original Feed Length and Composition	Lowering Rate (mm/day)	Results
68	420°C	Self seed	2.5 g Ga	3.0 cm $\text{Ga}_{0.7}\text{In}_{0.3}\text{Sb}$	2.0	No growth achieved.
69	420°C	Self seed	5.5 g Ga_{In}	3.0 cm $\text{Ga}_{0.7}\text{In}_{0.3}\text{Sb}$	2.0	No growth achieved.
74	420°C	$\text{Ga}_{0.7}\text{In}_{0.3}\text{Sb}$	1.32 g Ga 1.57 g In	1.5 cm $\text{Ga}_{0.7}\text{In}_{0.3}\text{Sb}$	1.0	Only 0.2 mm deposited on seed. Temperature apparently too low for growth.
75	600°C	Self seed	1.25 g Ga 1.53 g In	2.0 cm $\text{Ga}_{0.7}\text{In}_{0.3}\text{Sb}$	1.0	Growth seemed successful.
77	600°C	Self seed	1.33 g Ga 1.57 g In Atom ratio $\text{Ga/In} = 1.4$	3.5 cm $\text{Ga}_{0.5}\text{In}_{0.5}\text{Sb}$	2.0	3.3 cm polycrystal successfully grown. Large grains were present with no solvent inclusion.
87	600°C	Self seed	2.0 g Ga 0.82 g In Atom ratio $\text{Ga/In} = 4.0$	2.5 cm $\text{Ga}_{0.7}\text{In}_{0.3}\text{Sb}$	2.0	Large-grained polycrystal with no inclusions and cracks along the radial direction, as in THM-77.
80	1100°C	Self seed	2.40 g Ga	13.12 GaAs 0.07 Al $\sim \text{Ga}_{0.97}\text{Al}_{0.06}\text{As}$	4.0	White powder (AlAs?) on wall of quartz ampoule and on feed material. Unsuccessful.

TABLE VI (continued)

Run THM	Heater Temp.	Seed	Original Feed Composition	Original Feed Length and Composition	Lowering Rate (mm/day)	Results
82	1114°C	Self seed	2.0 g Ga	~Ga _{0.94} Al _{0.06} As	2.0	Same as THM-80.
88	1110°C	GaAs seed 0.75 cm dia. 1.5 cm long < 111 > direction	1.025 g Ga	4.12 g GaAs 0.024 g Al ~Ga _{0.97} Al _{0.03} As	4.0	The growth took place inside a BN tube sealed in the usual evacuated quartz ampoule. No ALAs occurred and 1.5 cm of GaALAs was seeded and successfully grown. New grains nucleated near the BN crucible wall and propagated into the bulk of the ingot.

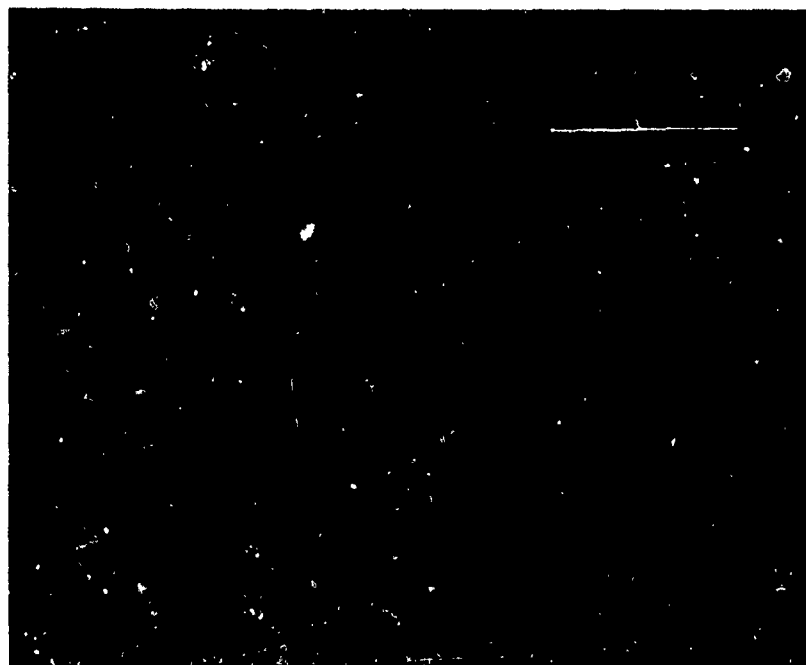


Figure 20: THM $\text{Ga}_x\text{In}_{1-x}\text{Sb}$ crystals and slow-cooled casting.
THM-87 - $\text{Ga}_{0.7}\text{In}_{0.3}\text{Sb}$
THM-77 - $\text{Ga}_{0.5}\text{In}_{0.5}\text{Sb}$

of three separate Ga zone passes performed on a vertical gradient freeze grown crystal GF-30, was very large. Almost all impurities decreased in concentration, some by a factor as large as 20 (as in Be). Most significantly, the most common and important impurities in GaAs, such as B, Mg, Si, Cr, Mn, Cu, Zn and Te all showed decreases. THM-73 had one of the lowest impurity concentrations in GaAs grown in this laboratory.

6. Growth $\text{Ga}_x\text{In}_{1-x}\text{Sb}$ and $\text{Ga}_x\text{Al}_{1-x}\text{As}$

A few experiments on growth of mixed III-V crystals were also performed, as summarized in Table VI. Feed rods of $\text{Ga}_{0.5}\text{In}_{0.5}\text{Sb}$ and $\text{Ga}_{0.7}\text{In}_{0.3}\text{Sb}$ were prepared by casting in fused silica tubes. Preliminary exploratory experiments revealed that at heater temperature of 420°C , it was not possible to grow the crystal by the THM whether a pure Ga, pure In or a mixed Ga, In zone were used. The melting points of GaSb and InSb are 702°C and 525°C , respectively. Raising the heater temperature to 600°C seemed to allow growth at 1-2 mm/day. THM-77 was grown at this temperature from a $\text{Ga}_{0.5}\text{In}_{0.5}\text{Sb}$ feed and a 1.4 Ga: In zone. THM-87 was grown from a $\text{Ga}_{0.7}\text{In}_{0.3}\text{Sb}$ feed and a 4.0 Ga: In zone. Both crystals were self-seeded. Length-wise sections of the two are shown in Figure 20, together with a crystal of $\text{Ga}_{0.7}\text{In}_{0.3}\text{Sb}$ grown by slow cooling from the melt.

It is apparent that the THM grown crystals contained much larger grains with no apparent segregation or inclusions. Samples of

the two crystals were sent for spectrochemical analysis in order to obtain the solute concentration profiles along the growth direction. Stress due to compositional variations have produced the cracks which appeared in the radial direction in all three crystals shown.

Attempts to grow $\text{Ga}_x\text{Al}_{1-x}\text{As}$ in the usual silica ampoule proved unsuccessful, possibly because AlAs formed and segregated, exhausting the Al in the Ga solution and forming an insulating layer on the feed material. The problem was solved by performing the growth inside a BN crucible sealed inside an evacuated silica ampoule. The feed material was GaAs with Al wire placed along the length of the feed rod, giving a feed material composition of approximating $\text{Ga}_{0.97}\text{Al}_{0.03}\text{As}$. The heater temperature was 1110°C , the lowering rate was 4.0 mm/day and the crystal THM-88 was seeded in the $\langle 111 \rangle$ direction. The growth was successfully completed. About 80% of the first 4 mm of growth was single crystalline. New grains nucleated near the BN crucible wall and propagated inwards. No solvent inclusion, AlAs or oxide segregation was observed.

II. STUDIES OF CRYSTAL GROWTH PHENOMENA

A. Organic Analog of Gradient Freeze Growth

Chong E. Chang

1. Experiments

In order to observe the freezing interface, pure naphthalene was used. Nichrome wire was wound on silica tube, increasing the number of windings from bottom to top. A fairly linear temperature profile in the heater was obtained. A pyrex tube of 10.6 mm I.D. was used as the container, and a thermal shield (pyrex tube) was placed between the growth tube and the heater. A schematic diagram of the apparatus is shown in Figure 21.

The Biot number (H) estimated for this arrangement is about 0.1. The heater temperature was lowered by continuously decreasing the power input. The cooling rate (θ) of the heater and that of the tube inside the heater were almost identical and constant throughout the freezing process.

2. Interface Shape - Without Cooled End

The temperature profile in the naphthalene rod for the present experimental conditions was estimated for $H = 0.1$, temperature gradient $G = -2.2^{\circ}\text{C}/\text{cm}$, length of tube $L = 12\text{ cm}$, and radius of tube $R = 0.53\text{ cm}$, and is presented in Figure 22. The predicted temperature profile for naphthalene showed a more curved S-shape than for GaAs (as shown in previous progress report [1]). Suspended carbon particles failed to detect the presence of natural convection in the liquid. A fine

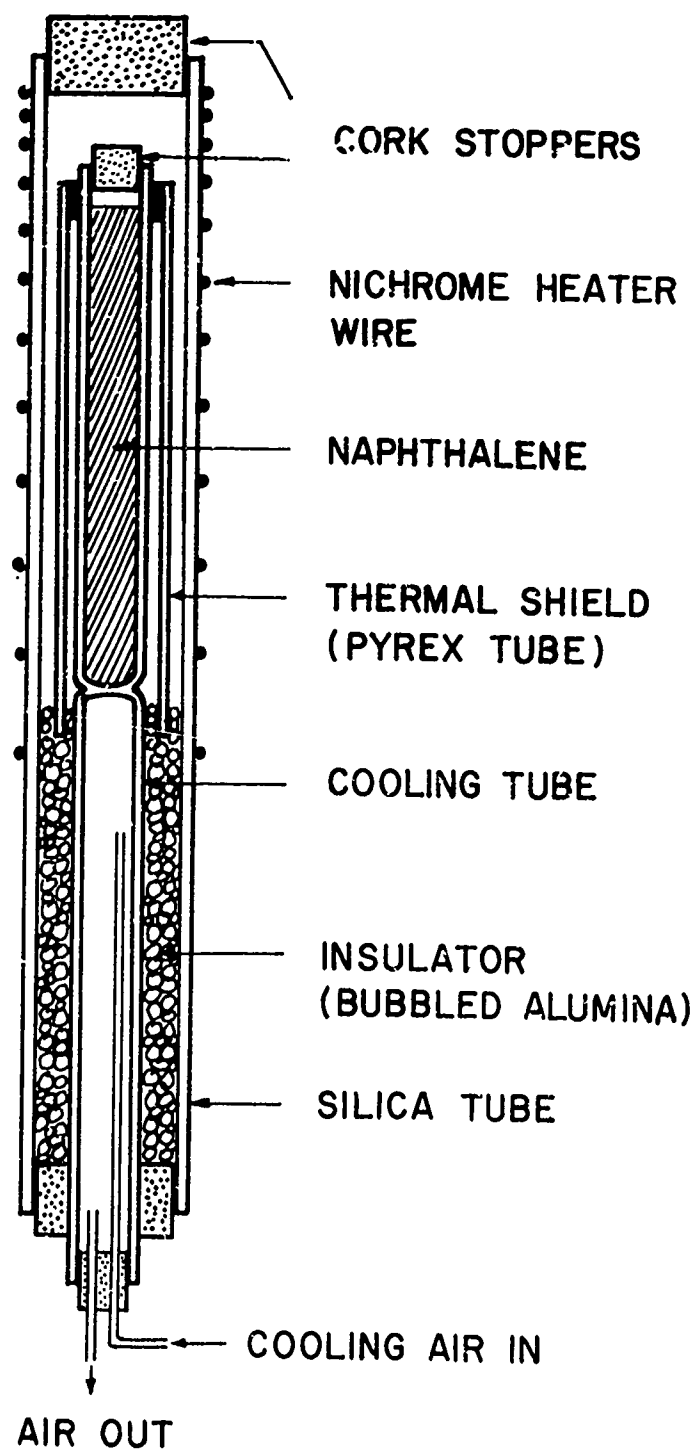


Figure 21: Schematic diagram of gradient freeze apparatus for observation of interface shape.

thermocouple (0.003 inch dia.) placed at the center of tube did not detect temperature fluctuations characteristic of vigorous free convection.

The freezing interface was observed through a microscope. A curious freezing phenomena was noted at the ends of tube. Instead of initiating at the tip of the tube, the liquid appeared to freeze instantaneously up to 1.5 ~ 2.0 cm from the base of the bottom end of the tube. As the interface approached the top of the tube, the liquid began to freeze on the wall at the top of the tube before the interface reached there. This instantaneous freezing at the ends of tube is thought to be due to a supercooling of the liquid at the ends of tube because of the S-shaped temperature profile of the system ($\beta = \theta \rho C_p R / Gk \approx 0.1$) as illustrated in Figure 22. The measured solid-liquid interface shape versus axial position is shown for $\beta = 0$ (i.e., $\theta = 0$), and $G = -3.0^\circ\text{C}/\text{cm}$ in Figure 23 (A). The convex interface shape in the bottom tip was caused by the effect of the tapered bottom end since a tapered end is cooled more effectively than a flat end. The experimental interface shape shown in Figure 23 (A) agrees with the theoretical results in Figure 22 which predict a concave shape for the first 50% of the tube and a convex interface for the remainder. The fraction freezing with a concave shape is expected to increase as freezing rate increases, as exemplified in Figure 22. Under the experimental conditions shown in Figure 23 (B) ($\beta = 0.097$, $G = 3.0^\circ\text{C}/\text{cm}$, $H = 0.1$, $L = 12$ cm, $R = 0.53$ cm), theory predicts a concave interface for the first 87% of the tube, the fact of which indicates that the heat of fusion (which was not taken into account in the theory) caused the interface

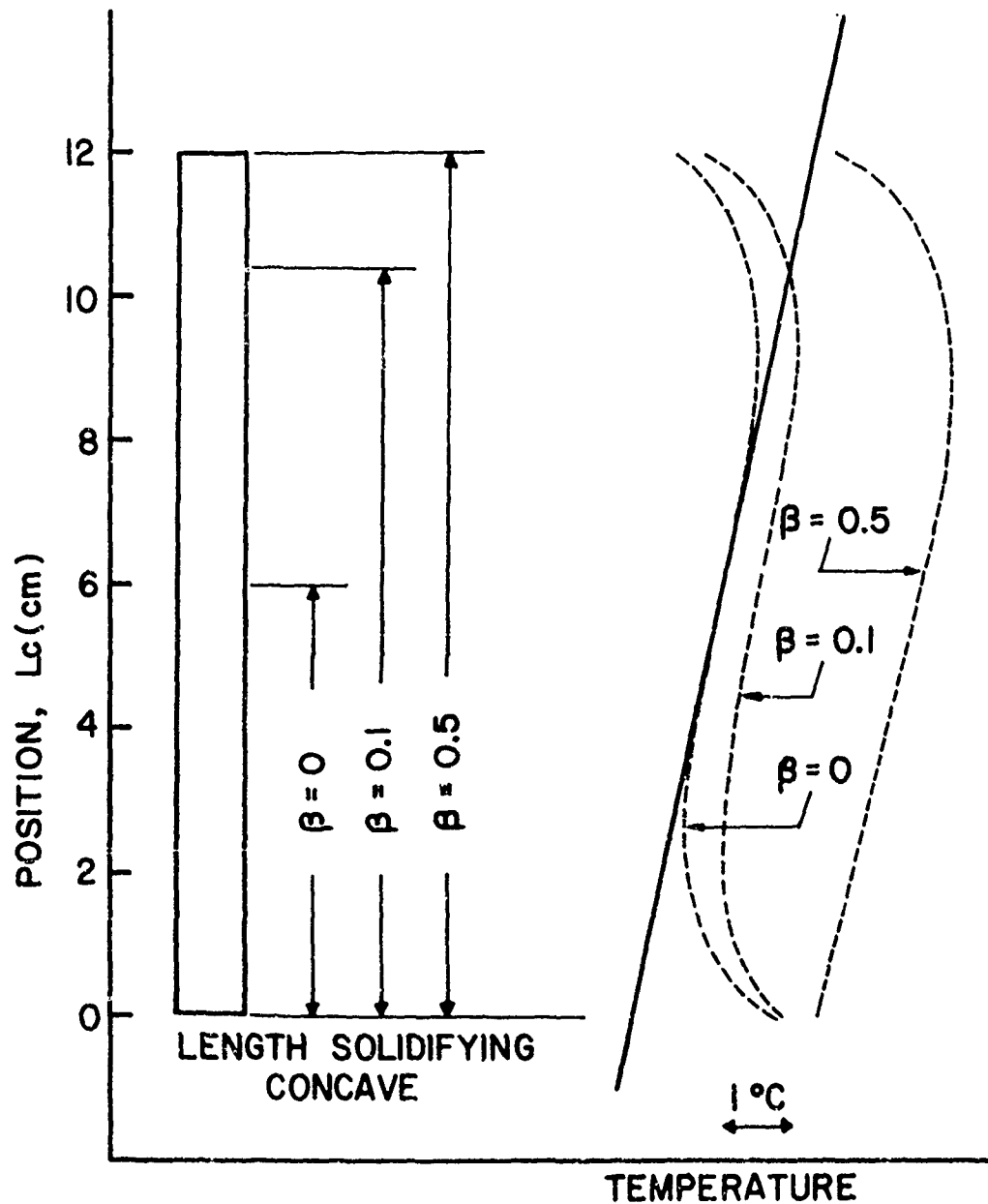


Figure 22: Temperature profiles and length solidifying concave predicted by one-dimensional heat transfer analysis for gradient freeze crystal growth.
 Dimensionless heat transfer coefficient, Biot Number, $H = 0.1$
 Temperature gradient, $G = -2.2^\circ\text{C}/\text{cm}$
 Tube length, $L = 12$ cm
 Tube radius, $R = 0.53$ cm
 — furnace temperature
 - - - - temperature in ampoule

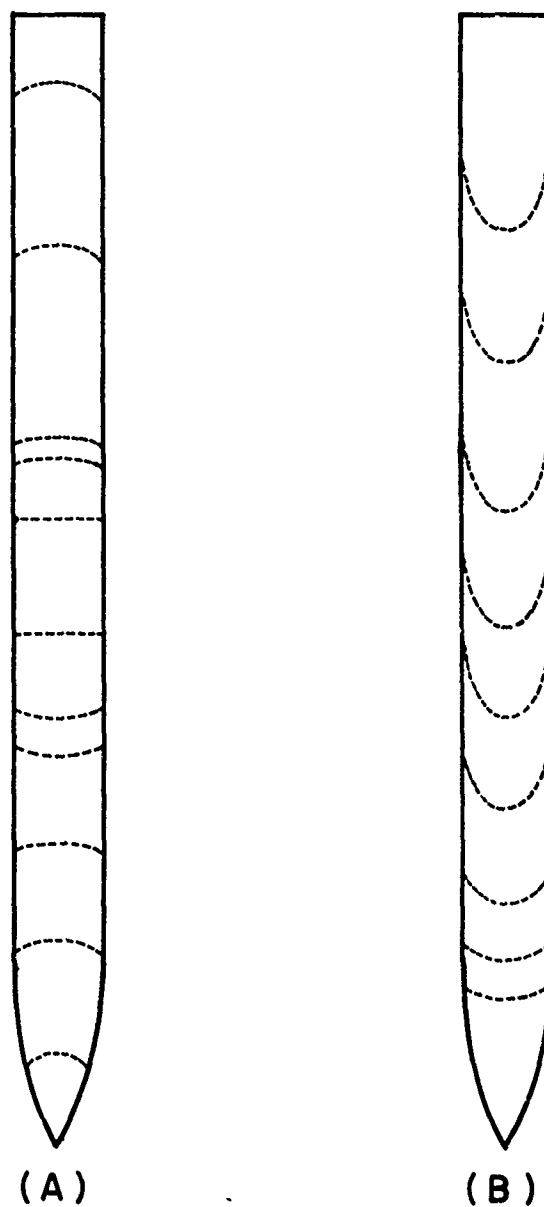


Figure 23: Solid-liquid interface shape versus axial position for gradient-freeze growth of naphthalene with $G = -3.0^{\circ}\text{C}/\text{cm}$, $L = 12 \text{ cm}$ and $R = 0.53 \text{ cm}$.
 (A) Zero freezing rate, $\theta = 0$, $\beta = 0$.
 (B) Finite freezing rate, $\theta = -8.8 \times 10^{-4}^{\circ}\text{C}/\text{sec}$, $\beta = 0.097$.
 Interface shapes shown at 30 min. intervals.

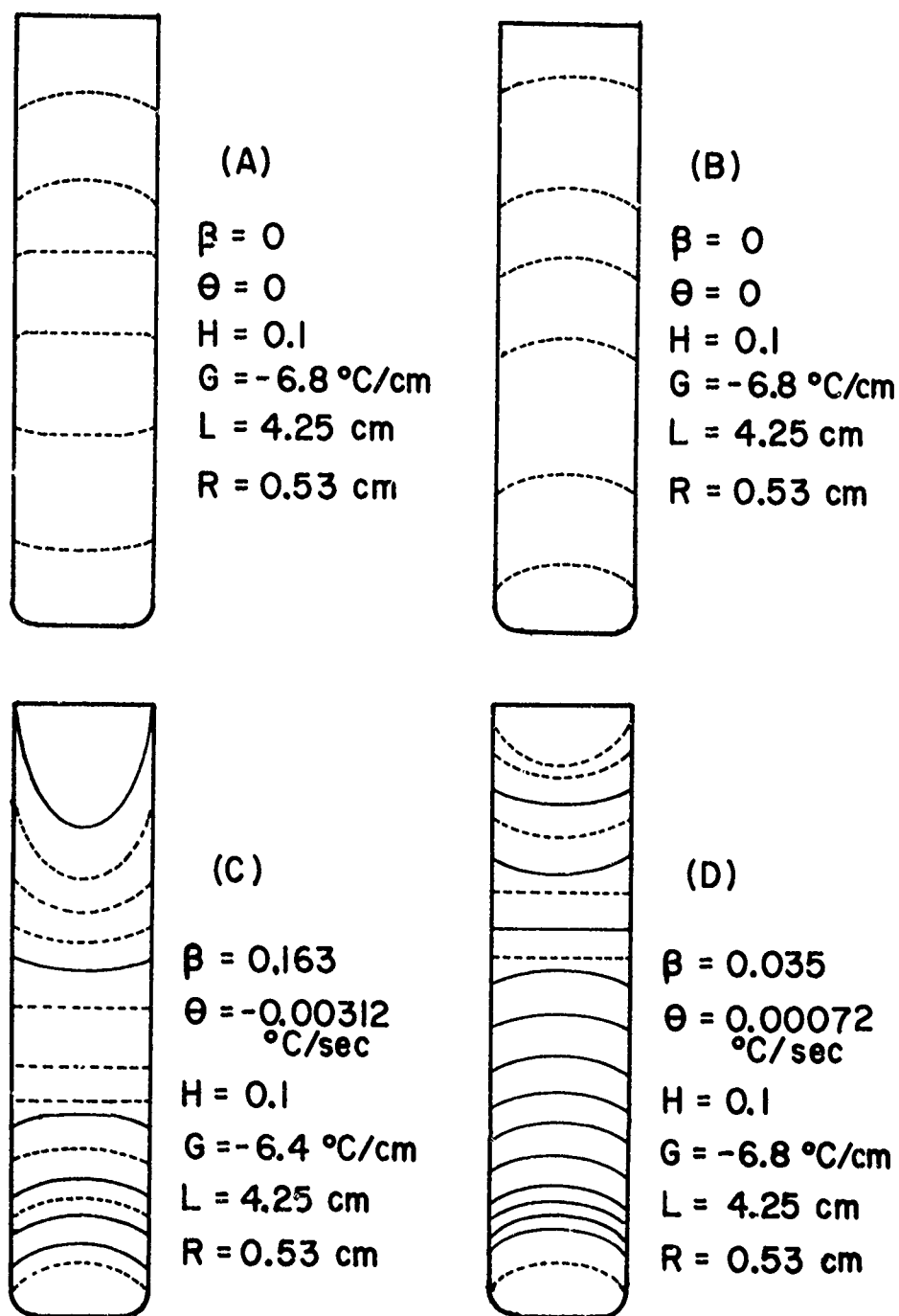


Figure 24: Solid-liquid interface shape vs. axial position for gradient-freeze growth of naphthalene. Curves in (C) and (D) indicate interface positions at one-hour intervals.

(A) Zero freezing rate without cooling bottom
 (B) Zero freezing rate with cooled bottom
 (C) Rapid freezing with cooled bottom
 (D) Slow freezing with cooled bottom.

shape to be more concave.

3. Interface Shape - With Cooled End

The bottom end of the tube was cooled by air through a tube joined below with the tube containing naphthalene as shown in Figure 21. The flow rate of cooling air was maintained constant. For a zero cooling rate (i. e., $\beta = 0$), the interface shape versus tube locations were as shown in Figure 24 (A) when the bottom end was not cooled, and in Figure 24 (B) when the bottom end was cooled. From these figures we see that when the cooling rate was very slow (i. e., $\theta \rightarrow 0$), cooling the bottom end forced the entire tube to freeze with a convex interface (only the upper half of the tube would have frozen with a convex interface shape if the bottom end had not been cooled). Figures 24 (C) and 24 (D) show the freezing interface shape when the bottom was cooled. Note that a slow cooling rate ($\theta = -0.72 \times 10^{-3} \text{ }^{\circ}\text{C/sec}$, Figure 24 (D)) forced a larger fraction of the tube to freeze with a convex interface shape and to freeze with a less concave interface shape on the top than a fast cooling rate ($\theta = -3.12 \times 10^{-3} \text{ }^{\circ}\text{C/sec}$, Figure 24 (C)). Increasing the length of the tube did not force a larger fraction to freeze with a convex interface, as shown in Figure 25.

The temperature gradient in the bottom end became steeper when it was cooled. This resulted in a slower freezing rate at the bottom end, as shown in Figures 24 (C) and (D), and 25. The freezing rate at the top was significantly faster than the rate at the bottom.

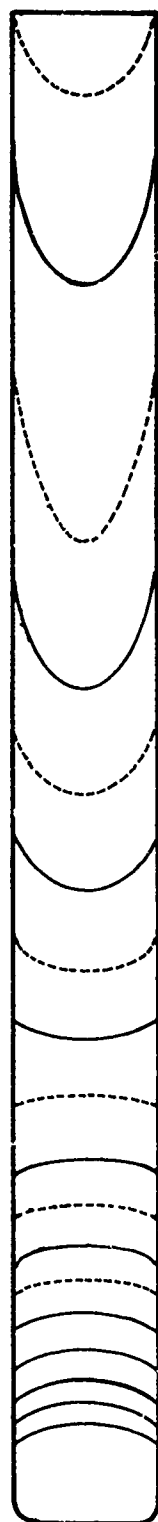


Figure 25: Solid-liquid interface shape at one-hour intervals vs. axial position for gradient-freeze growth of naphthalene.
 $\theta = 0.00099^\circ\text{C}/\text{sec}$, $G = -3.0^\circ\text{C}/\text{cm}$, $\delta = 0.11$, $L = 10$ cm,
 $R = 0.53$ cm.

B. Organic Analog Experiments on Zone Melting

Chong E. Chang

In order to obtain further information about the influence of zone parameters on the travelling heater method and on liquid encapsulated floating zone melting, temperature measurements and microscopic observations of the interface were made for zone melting of pure naphthalene in the same manner as for the travelling heater growth of naphthalene from naphthalene-benzoic acid solution reported previously [1]. The interfacial temperature gradients in the solid versus travel rate were evaluated from the measured temperature profiles and are summarized in Figure 26 as a function of tube diameter. It is seen that the temperature gradients generally increased as the diameter of the tube decreased and as the interface position moved closer to the cold bath. The temperature fluctuations in the zone decreased as the length of the zone decreased, since disturbances in well-defined convection currents occurred in the portion of the zone which protruded into the cooler. However, the macroscopic interface shape was significantly distorted when the length of zone became short, as shown in Figures 27 and 28. This was because of a tendency for the interface shape to follow the stream line of the convection currents in the short zone, which normally lay completely within the heater. The heat transfer coefficients at the interface were calculated from the measured temperature gradients by the interfacial heat balance. The dependence of heat transfer coefficients at the bottom interface on the travel rate generally decreased as the

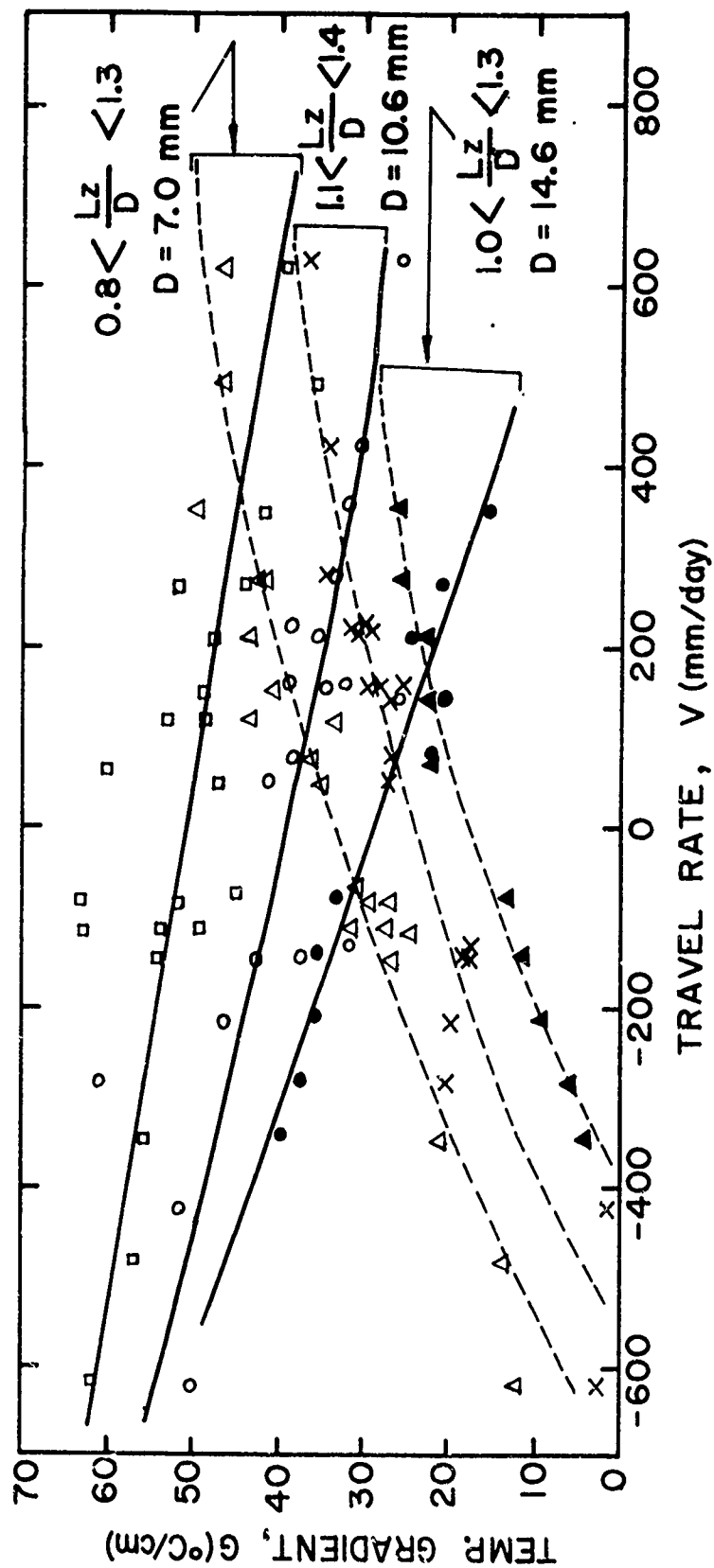


Figure 26: Experimental interfacial temperature gradients in vertical zone melting of naphthalene as a function of zone travel rate.

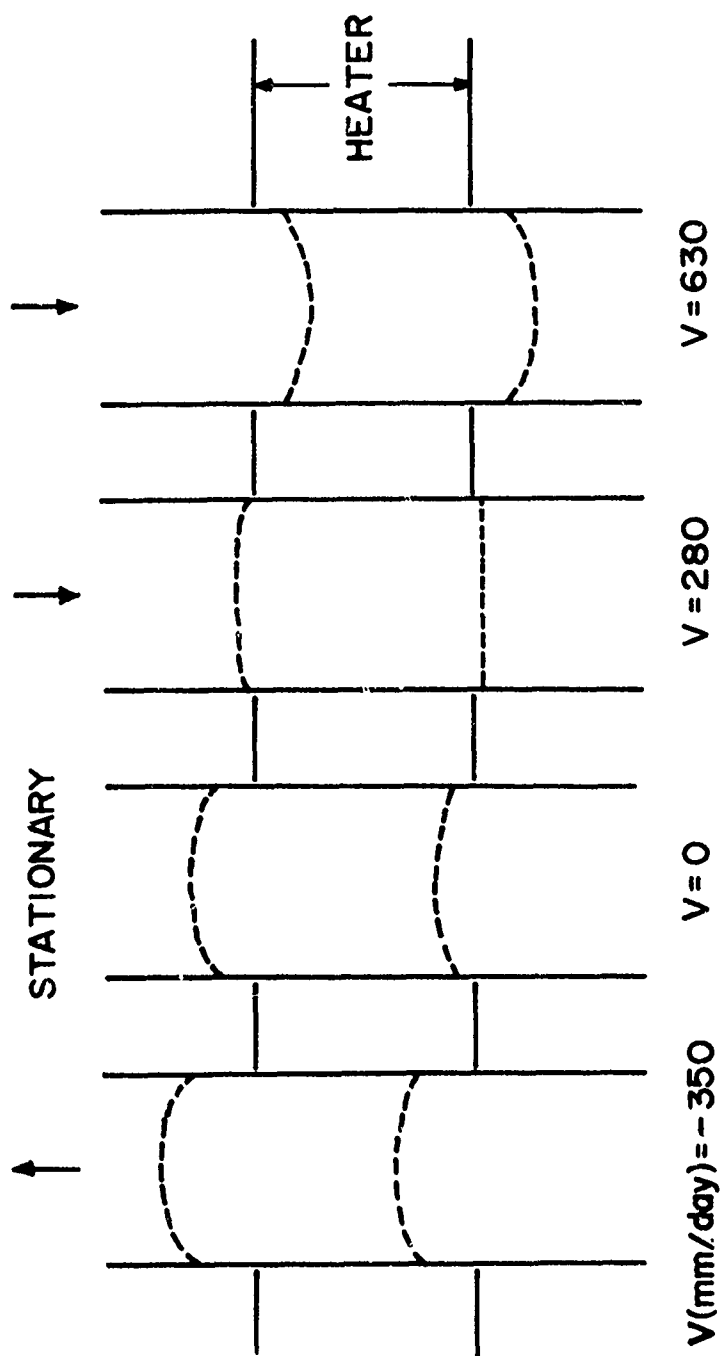


Figure 27: Schematic interface shapes for vertical zone melting of naphthalene with a zone longer than the heater.

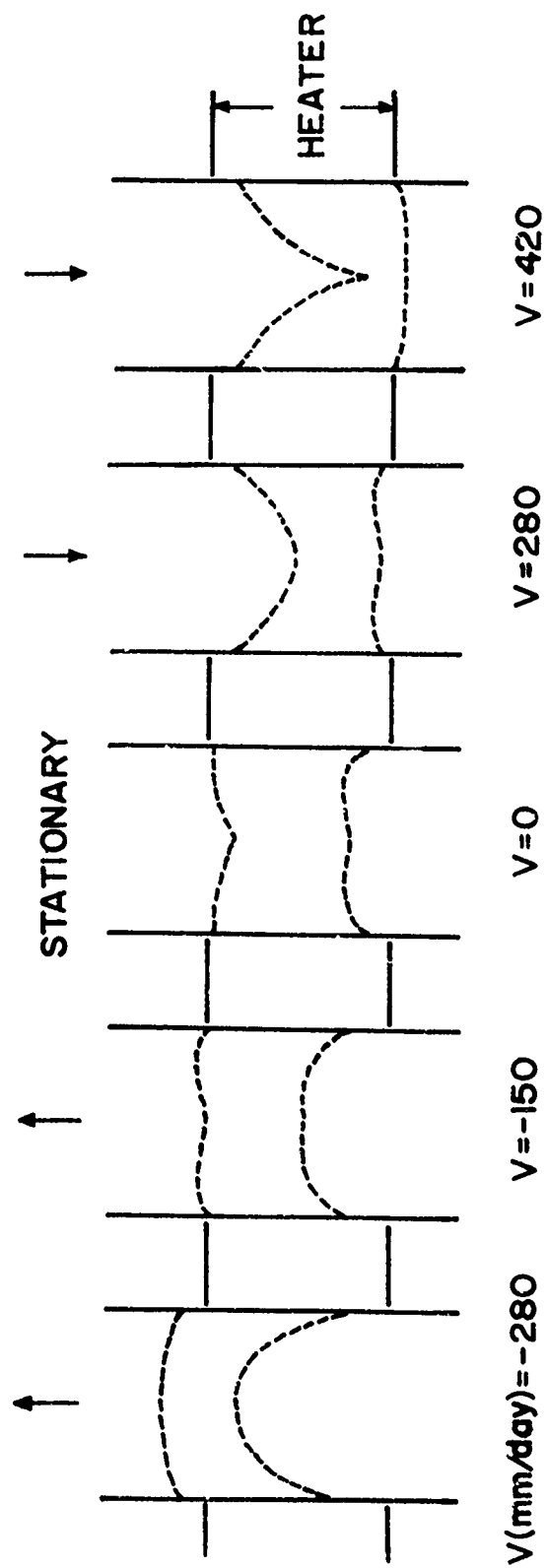


Figure 28: Schematic interface shapes for vertical zone melting of naphthalene with a zone shorter than the heater.

diameter of the tube decreased and as the temperature gradient increased.

A talk was given on localized interface breakdown [4].

C. Other Crystallization Studies

W. R. Wilcox, V. H. S. Kuo and K. H. Chen

A final report [5] and two papers [6,7] were written on the factors influencing incorporation of foreign particles during solidification. Further experiments to elucidate the forces involved in particle pushing are being designed. Papers were also published on movement of liquid inclusions by centrifugation [8] and on boiling and convection during movement of inclusions by temperature gradients [9].

Nucleation of bubbles during crystallization has been analyzed theoretically [10]. Comparison with experience shows that bubble nucleation during solidification is probably homogeneous, while that during solution growth is probably heterogeneous on the crystal surface. The tendency to form bubbles increases as the gas pressure over the melt increases, as freezing rate increases, as stirring decreases, as the height of the melt over the interface increases, and is influenced by the temperature of the melt surface.

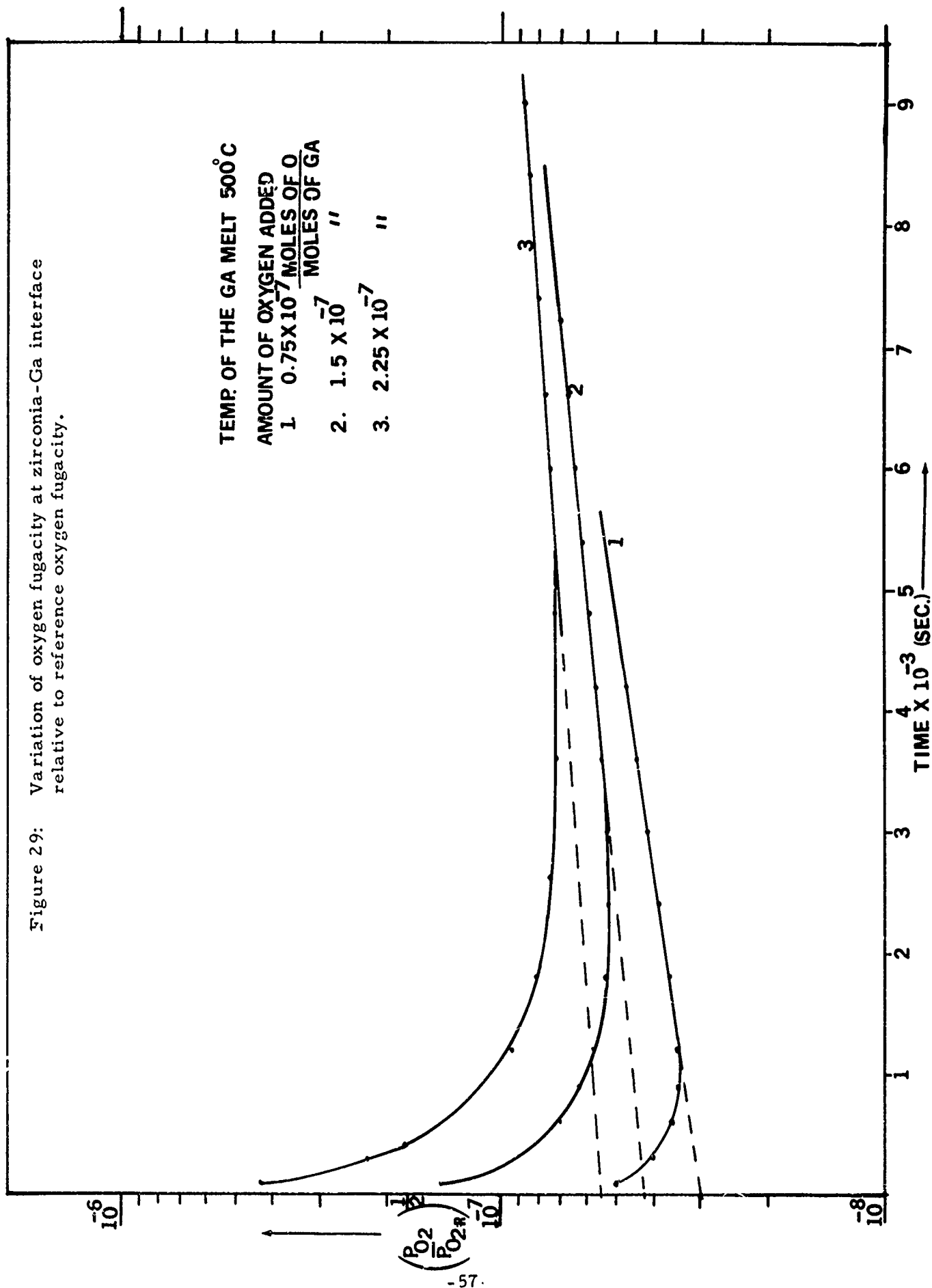
III. OXYGEN MEASUREMENT AND CONTROL IN LIQUID EPITAXIAL GROWTH OF III-V SEMICONDUCTORS

J. M. Whelan

The program to estimate the concentration of oxygen in GaAs and to grow an epitaxial thin film of GaAs at low temperatures [1] has been continued. Experiments were conducted to determine the concentration of oxygen as a function of its fugacity in Ga solutions at 670° and 500°C . This dependency is necessary to estimate the concentration of oxygen in GaAs. To measure the changes in oxygen fugacities with the amounts of oxygen added or removed from Ga solutions, the experiment was done as follows. Oxygen was pumped out of Ga by passing a known amount of charge through the zirconia, transporting oxygen as ions. At a particular e.m.f. value after adding a known amount of oxygen into the solution, the e.m.f. of the cell was measured as a function of time. This served to measure the fugacity of the oxygen at the zirconia-Ga interface as a function of time. These data were then extrapolated to a non-transient change in the oxygen fugacity upon the addition of a measured amount of oxygen, as shown in Figure 29.

Hydrogen which was saturated with water vapor at 0°C was used to fix the oxygen fugacity at the reference electrode. Hydrogen not saturated with water vapor caused a drifting e.m.f. To improve the degree of saturation, the water bubbler was replaced by a new one. In the new bubbler, hydrogen was passed through a long spiral tubing chilled with liquid water at 0°C before it bubbled through a fritted disc into the water.

Figure 29: Variation of oxygen fugacity at zirconia-Ga interface relative to reference oxygen fugacity.



Glass beads were also placed on the outlet side of the bubbler to collect any entrained water droplets. With the new bubbler the e.m.f. measurements were uniform and steady to 0.1 mV, corresponding to water vapor pressure in the reference electrode being constant to within 0.13 percent.

The fugacities of atomic oxygen in Ga solutions at 670°C could be reduced readily by 3 orders of magnitude below that achieved by flushing with Pd diffused hydrogen alone. It was observed that the leakage rate of oxygen from the reference side of the electrode to the Ga solution was the rate limiting mechanism for oxygen leaking into Ga. After pumping, the observed leakage rates were reasonable in terms of the electronic transference numbers published by Etsell and Flengas [11]. To reduce these leakage rates, the temperature of the Ga was lowered to 500°C. At 500°C mole fractions of oxygen equal to 5×10^{-8} could be measured by measuring the cell e.m.f. Preliminary data indicated that Henry's law is obeyed for this concentration range. The Henry's law constant is unfortunately still subject to some uncertainty because of a delayed realization that the charge measurements contained an uncertainty.

Because of the easy ability to reduce the fugacities of atomic oxygen in Ga solution at 670°C and 500°C about 3 and 5 orders of magnitude, respectively, below those achieved by Pd diffused hydrogen, it is apparent that this pumping means will be useful for growing GaAs films at these reduced temperatures. (This presumes that the difficulty at these low temperatures are associated with an oxide on the GaAs substrate.)

IV. CHARACTERIZATION

A. Dislocation Studies and Electrical Properties

Agerico L. Esquivel, Sanghamitra Sen and W. N. Lin

This section deals with the continued effort of characterizing dislocations in GaAs grown by the liquid seal Czochralski method in our Crystal Growth Laboratory. In our previous report [1] we applied the method of Infra-red Cathodoluminescence (IR-CL) to the surfaces of plastically deformed GaAs. In this report, the first section will deal with the characterization of deformed GaAs crystals with varying dislocation densities using the technique of IR-CL. The method will be extended to include not only IR-CL microscopy but also a study of IR-CL spectra as influenced by dislocations in GaAs. In the second section, the anisotropy of electrical properties in GaAs containing edge dislocations aligned parallel or perpendicular to the applied electric field will be described.

1. Cathodoluminescence Study of Deformed Regions in n-Type GaAs [12]

GaAs crystals were deformed so that an excess of either α -(Ga-) or β -(As-) dislocations of progressively increasing densities were introduced by four-point bending, as described previously [1]. The samples listed in Table VII were examined in an electron microprobe operated at 40 KV and with sample currents ranging from 0.46 to 0.70 microamperes. Most of the micrographs were taken at 200X and the surfaces examined represent square areas from 350 to 400 μ along each edge.

TABLE VII

Infra-red Cathodoluminescence Intensity, Half-width and
Peak Position for Control and Bent GaAs Samples

A. Horizontal Bridgman (HB-105) Undoped

No.	Sample No.	Condition Excess Disloc'n Type	Calculated Disloc'n Density ρ (cm^{-2})	Peak Pos'n λ_p (\AA)		Half- Width HW (\AA)		Relative Peak Intensity, I		% Change in Inten- sity Rela- tive to Tip
				Center	Tip	Center	Tip	Center	Tip	
1	F11-A-AG2	as-grown	$\sim 10^4$ (a)	8780	-	228	-	0.95	0.90	+5
2	F11-B-H2	Heated	—	8800	-	228	-	3.30	3.10	+6
3	F13-C-B1	Bent: B	5.8×10^6	(b)	-	(b)	-	(b)	-	-
4	F11-C-B2	α	5.0×10^6	8790	8810	224	228	1.64	3.20	-49
5	F12-C-B3	α	9.4×10^6	8320	8830	228	228	1.62	4.08	-60
6	F10-C-B4	β	1.7×10^7	8830	8830	225	230	2.10	3.52	-40

(a) From etch pits on (111) plane.

(b) Not determined.

TABLE VII (continued)

B. Czochralski (CZ-16) Doped Te (10^{17} cm^{-3})

No.	Sample No.	Cond'n	ρ (cm^{-2})	λ_p (Å)		HW (Å)		Relative I		% Change in I
				Center	Tip	Center	Tip	Center	Tip	
1	9A-AG1	as-grown	$\sim 10^3$ (a)	8780	-	245	-	1.75	1.60	+9
2	9B-H1	Heated	-	8780	-	240	-	3.06	3.44	-11
3	10F-B1	Bent: α	4.3×10^6	8790	8790	245	245	1.85	2.72	-32
4	10E-B2	β	4.6×10^6	8790	8790	250	240	1.74	2.47	-30
5	10C-B3	β	8.6×10^6	8780	8790	250	245	0.81	2.82	-71
6	10D-B4	β	1.5×10^7	8790	8790	245	246	2.21	3.54	-38

Figure 30 shows secondary electron emission (SEE) micrographs (column 1), IR-CL micrographs (column 2) and IR-CL intensity, I_c , versus distance, d , (column 3) from the edge of the undoped horizontal Bridgman (HB-105) crystals. The micrographs were taken from the (112) surface at the center of the sample as indicated by the black rectangle in the schematic diagram in Figure 30. In our previous report [1] it was shown that surface markings as well as growth striations became visible in the IR-CL micrographs. In the present set of pictures (Figure 30) a subsurface flaw not apparent in the SEE micrograph became visible when examined in the IR-CL mode as indicated by the arrows (Figure 30a, column 2) and by the decrease in IR-CL intensity in column 3.

The set of pictures in Figure 30 (a,b,c,d) describes the central portions of the bent horizontal Bridgman samples, while those in Figure 31 (a,b,c,d), the corresponding areas in the Te-doped Czochralski sample (CZ-16). The micrographs were taken in the order of increasing calculated dislocation density (indicated in column 2) and as a function of the type of excess dislocation (α or β) present. No significant features associated with the density or type of dislocation could be discerned from the micrographs. However, from the IR-CL micrographs dislocation densities were estimated by taking average counts of the number of black dots visible in column 2 and the number of minima recorded by the line scans in column 3.

The results of the dislocation density measurements based on the IR-CL micrographs are shown in Figure 32. The deviation of some of the

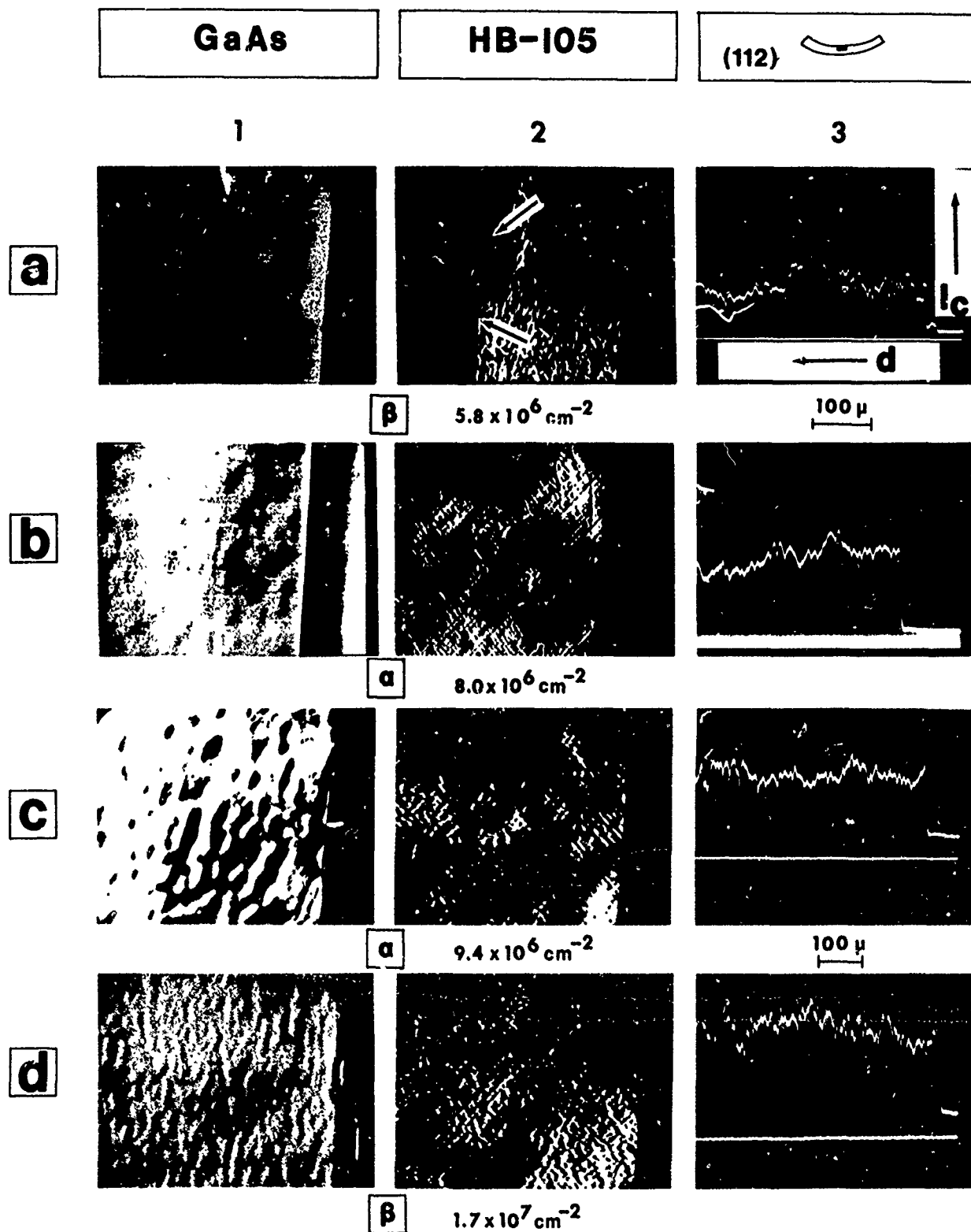


Figure 30: Caption on following page.

Figure 30: Secondary electron emission (SEE) micrographs (column 1), infra-red cathodoluminescence (IR-CL) micrographs (column 2) and IR-CL intensity, I_c , line scans versus distance, d , in microns (column 3) for the undoped, bent GaAs samples (HB-105). Areas examined were taken from the (112) surface at the center of the bend. Figures a, b, c, and d represent increasing dislocation densities (noted in column 2) and different types of excess dislocation (α and β). A subsurface flaw is indicated by arrows in (a) - column 2. Sample numbers: (a) F13-C-B1, (b) F11-C-B2, (c) F12-C-B3, (d) F10-C-B4.

(On Preceding Page)

Figure 31: SEE micrographs (column 1), IR-CL micrographs (column 2) and IR-CL intensity line scans for the doped ($\text{Te: } 10^{17} \text{cm}^{-3}$), bent GaAs samples (CZ-16). Figures a, b, c, and d represent increasing dislocation densities (noted in column 2) and different types of excess dislocation (α and β). Sample numbers: (a) 10-F-B1, (b) 10-E-B2, (c) 10-C-B3, (d) 10-D-B4.

(On Following Page)

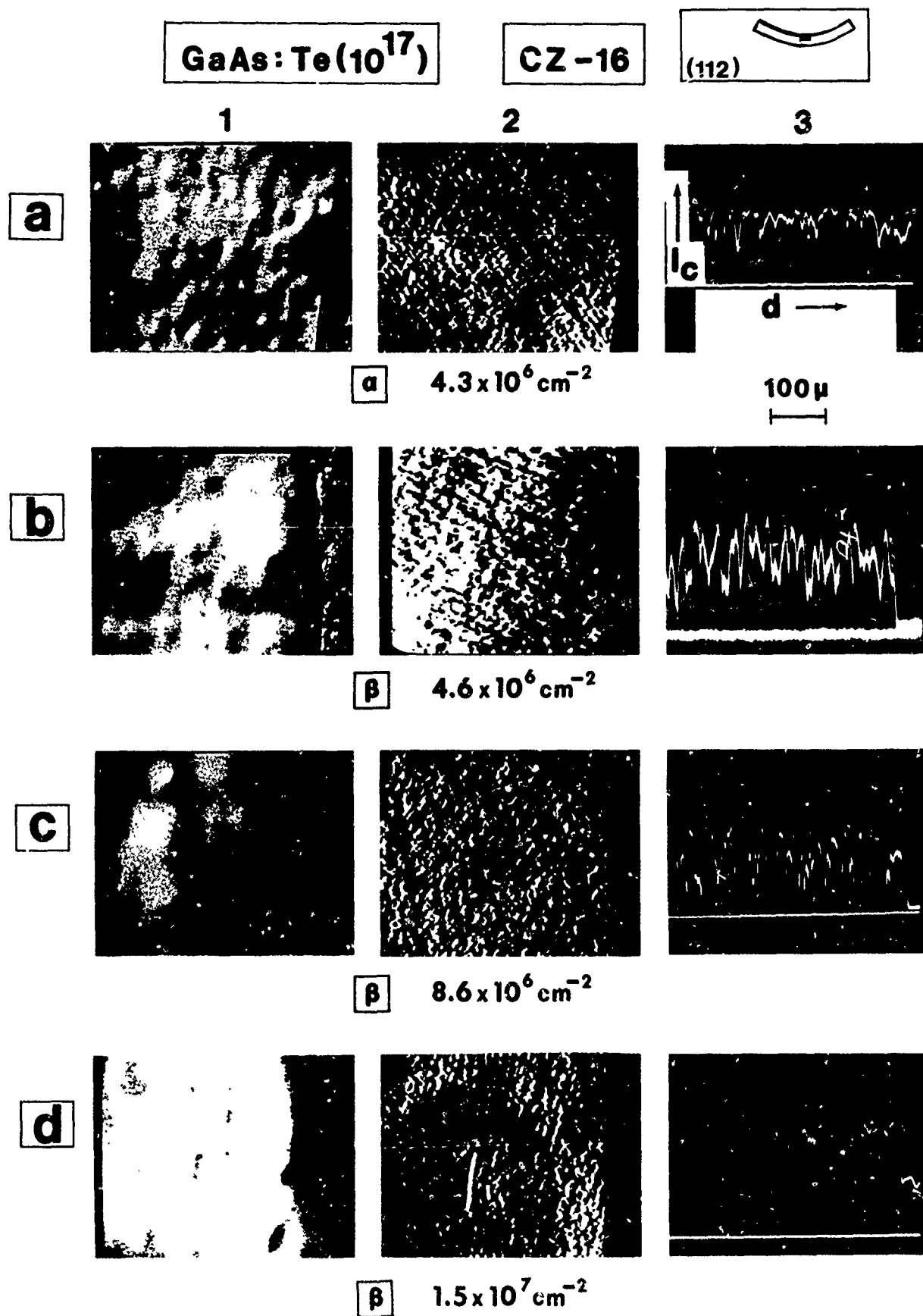


Figure 3l: Caption on preceding page.

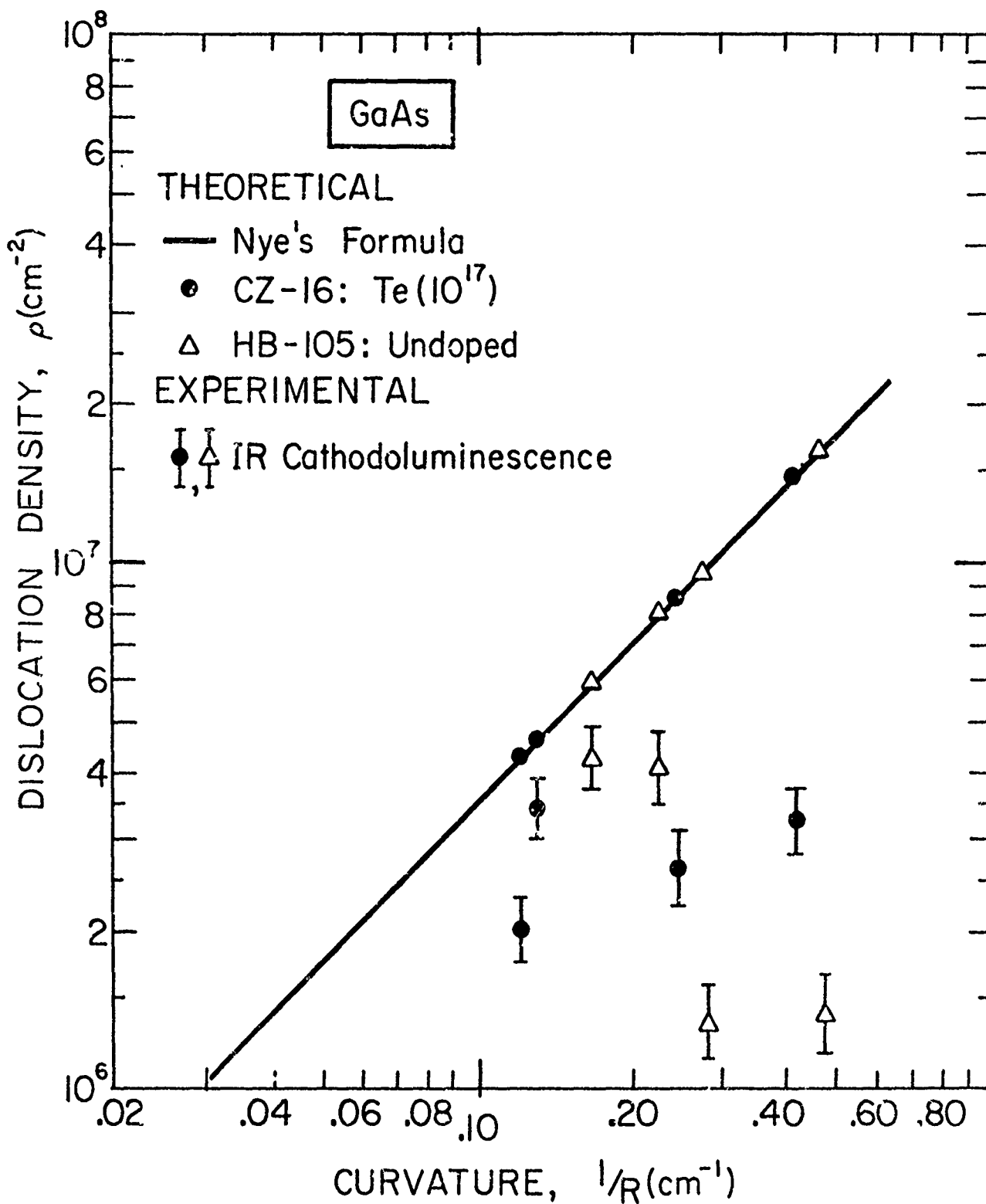


Figure 32: Determination of dislocation densities on the (112) face of bent GaAs samples (CZ-16 and HB-105) using the non-destructive infra-red cathodoluminescence (IR-CL) method. Deviation from the theoretical values can be improved by increasing the resolution of details in the IR-CL micrographs.

points from the calculated values was due mainly to the lack of resolution in the micrographs. However, from IR-CL micrographs obtained earlier [1] and from Figure 30b-2, the black dots believed to be associated with the end points of dislocations could be resolved to a diameter of $3\ \mu$. An attempt will be made to improve this resolution by determining an optimum level for the bias control. For the present, the three points close to the theoretical values in Figure 32 indicate the potential application of the IR-CL method for measuring dislocation densities in a non-destructive way, namely, without chemically etching the sample surface.

To obtain semiquantitative data related to the type and density of dislocations, the intensity, peak position and half-width of the infra-red (IR) peak at an emission energy of $E = 1.41\ \text{eV}$ ($\lambda_p = 8800\ \text{\AA}$) were recorded from the control and bent samples and from various positions within each bent or unbent sample. The observed IR spectra are shown in Figures 33-36. The spectra were taken from the areas indicated by black rectangles in the schematic diagrams of the samples. Also indicated in the figures are the type and density of dislocations in each sample. The curves indicate changes in IR peak intensity associated with heating or increase in dislocation density. No changes were observed in the peak position or half-width which could be related to the type or density of dislocations (Table VII-a, b).

For both the undoped and doped GaAs samples (Figures 33 and 34) an increase in IR intensity was noted after heating. This increase appeared genuine since the peak intensities recorded represented the average of

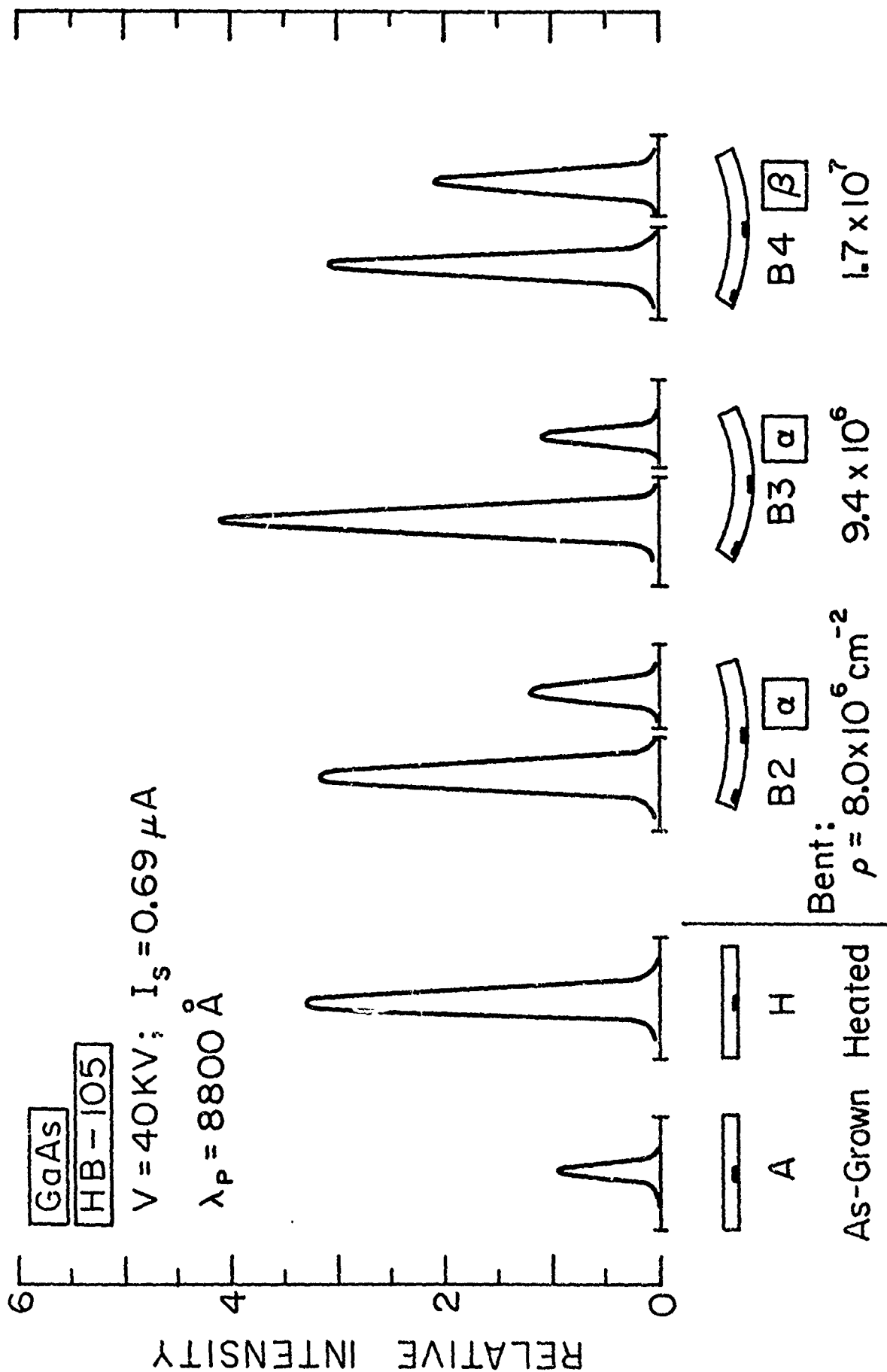


Figure 33: Caption on following page.

Figure 33: Relative infra-red cathodoluminescence (IR-CL) intensities taken from the center and tips of the as-grown (A), Heated (H) and bent GaAs samples (HB-105). Dislocation densities (ρ) and type of dislocation (α or β) are indicated. IR peak position is at $\lambda_p = 8800\text{\AA}$, at an accelerating voltage in the microprobe of 40 KV, and sample current of $0.69\mu\text{A}$. Areas examined are indicated by black rectangles in the schematic diagrams of the samples.

(On Preceding Page)

Figure 34: Relative IR-CL intensities for the as-grown (A), heated (H), and bent (CZ-16) GaAs samples with different types (α and β) and densities (ρ) of dislocations. Same scheme is followed as in Figure 33.

(On Following Page)

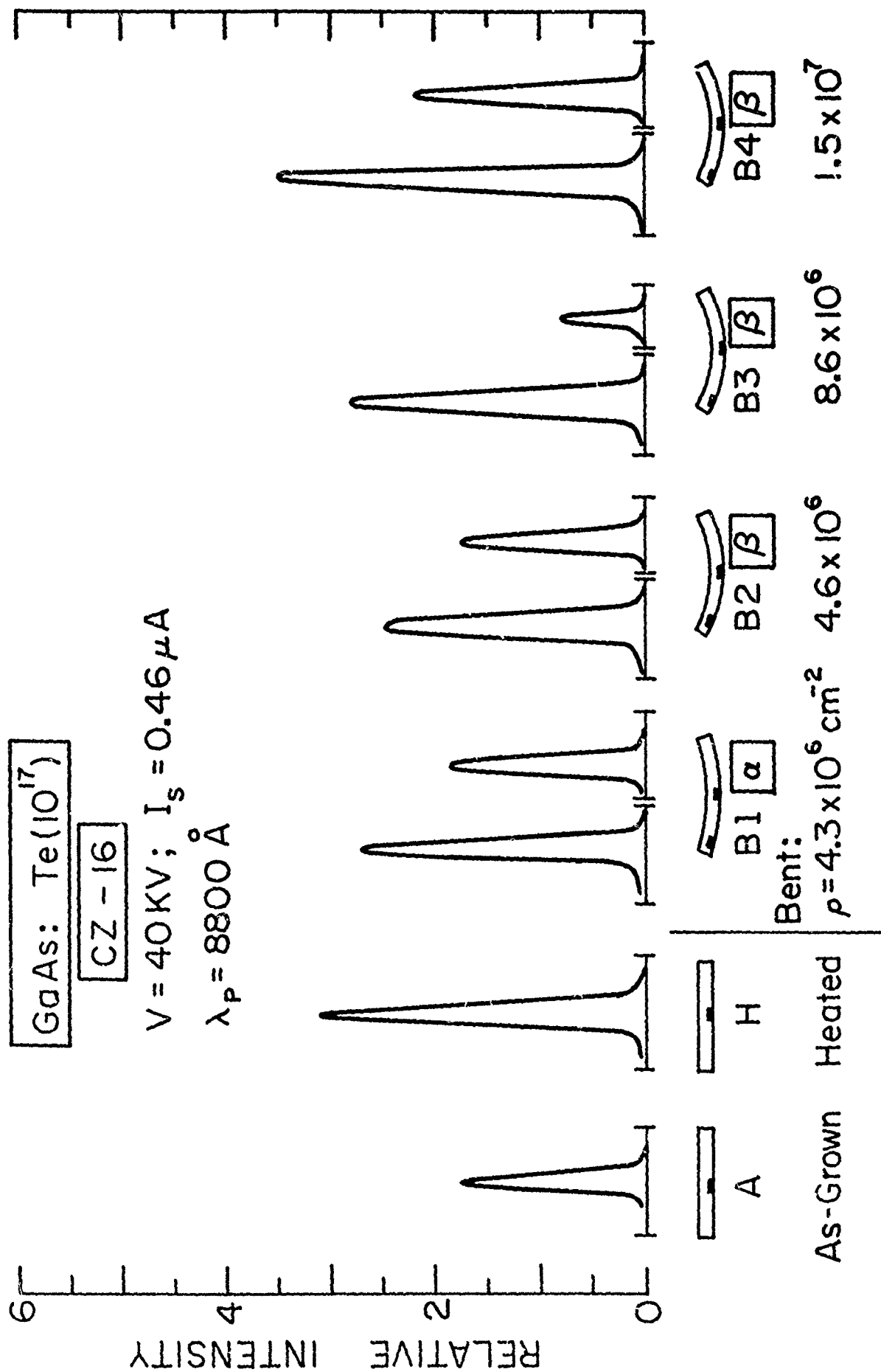


Figure 34: Caption on preceding page.

twelve to nineteen measurements along the length of each sample. Furthermore, the peak intensity of the heated sample approximated the intensities observed from the tips of the bent doped and undoped samples (Figures 33 and 34). Thus, short term heating at 700°C for 15 minutes produce an annealing effect on the dislocations in the as-grown sample as well as a probable redistribution of impurities. Both these processes appear to enhance radiative recombination at the observed wavelength in the heated sample and in the relatively undeformed tips of the bent samples.

Although no systematic decrease in IR intensity was observed with increasing calculated dislocation density in the bent samples, it was observed that the IR intensity from the central portion of the bent sample was consistently lower than the intensity from the relatively undeformed tip of the same sample. This observation was found true both for Bridgman and for Czochralski samples (Figure 33 and 34). To eliminate the possibility of excessive inhomogeneity within the same sample, the regions between the center and the tip as well as between the tensile and compressive surfaces of the bent samples were examined for changes in the IR intensity. The results shown in Figures 35 and 36 indicate a systematic decrease in IR intensity with increasing dislocation density. That the dislocation density increased upon approaching the bend center has been observed in previous IR-CL micrographs [1].

Although the process of recombination of excess carriers at dislocations is not fully understood, it is known that dislocations in

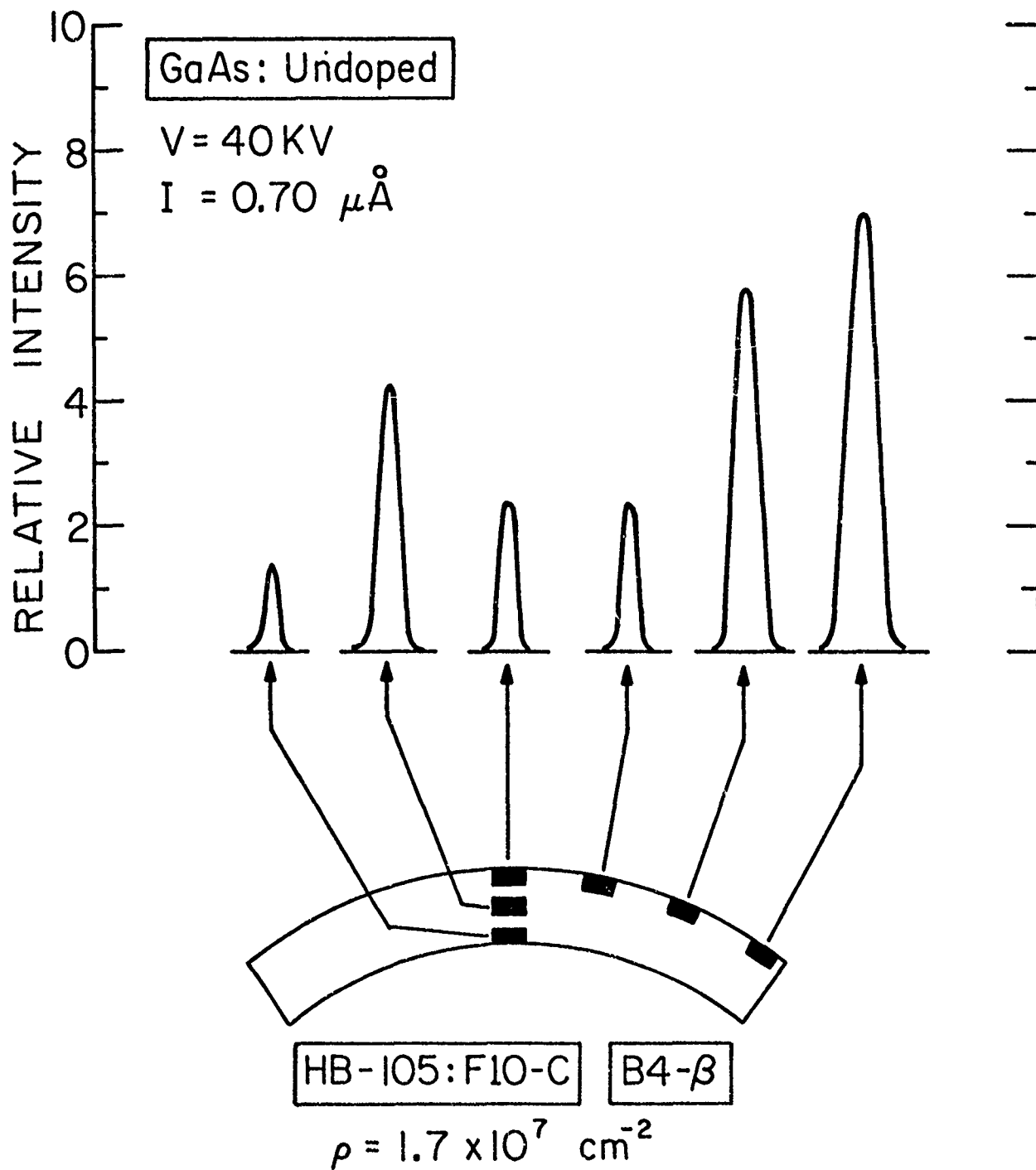


Figure 35: Relative IR-CL intensity as a function of position in a bent (HB-105) GaAs sample with a dislocation density, $\rho = 1.7 \times 10^7 \text{ cm}^{-2}$. Areas examined are indicated by black rectangles.

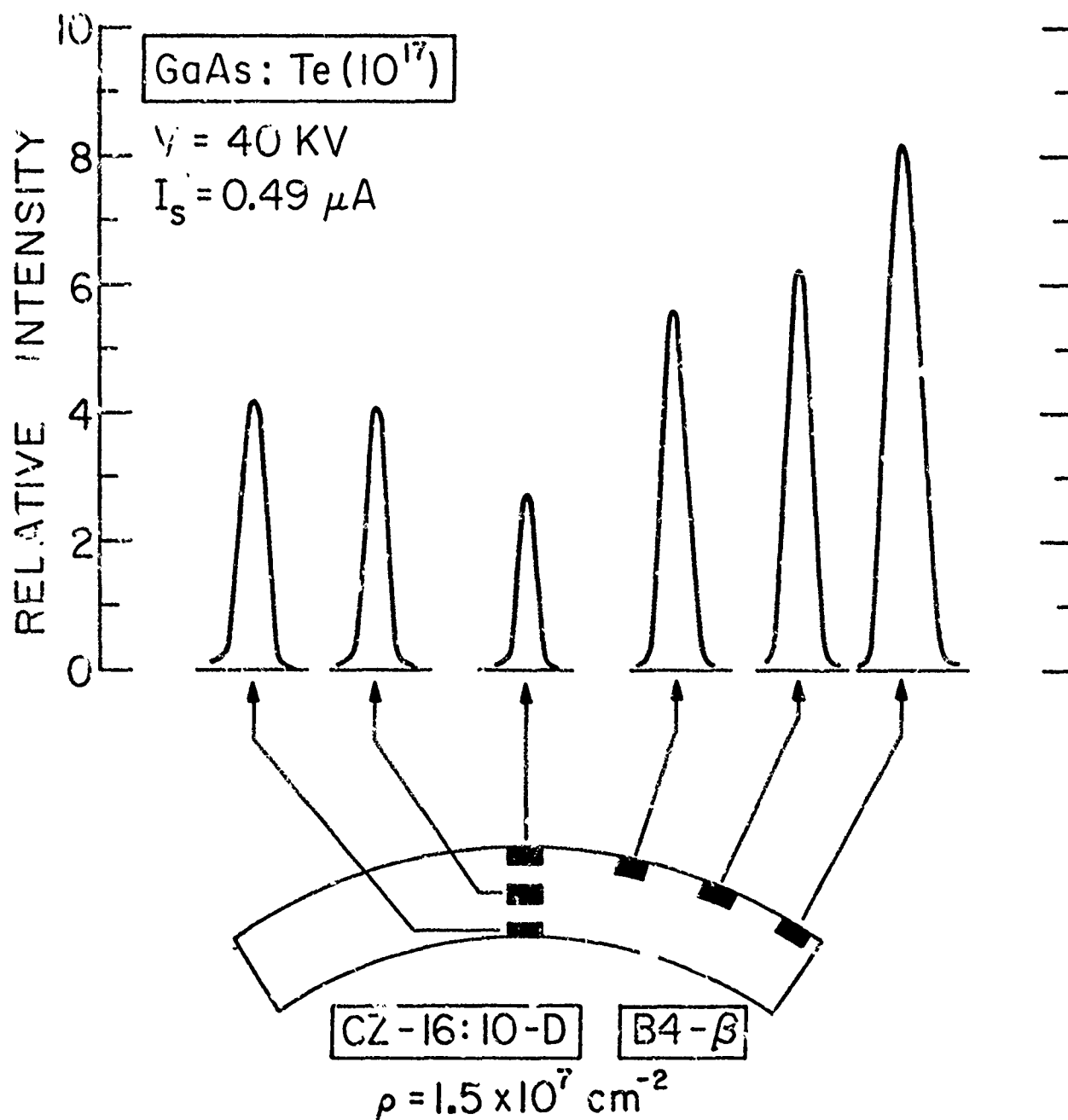


Figure 36. Relative IR-CL intensity as a function of position in a bent (CZ-16) GaAs sample with a dislocation density, $\rho = 1.5 \times 10^7 \text{ cm}^{-2}$. Black rectangles indicate areas examined.

germanium introduce deep acceptor levels which act as traps for minority carriers [13-16]. Dislocations in GaAs, however, would be expected to behave in the same way. Thus, in portions of the bent sample where the dislocation density is high, there is a corresponding high density of traps so that a decrease in radiative recombination takes place. There is also the possibility that dislocations act as recombination centers which emit IR radiation at a wavelength which falls beyond the range (0.6 to 1.1 μ) of our S-1 IR detector so that the observed low IR intensity represents merely a portion of the complete IR spectrum. Further study with a detection system capable of recording IR radiation at wavelengths greater than 1.1 μ should resolve this question.

2. Electrical Anisotropy from α - and β -Dislocations in Plastically Deformed GaAs [17]

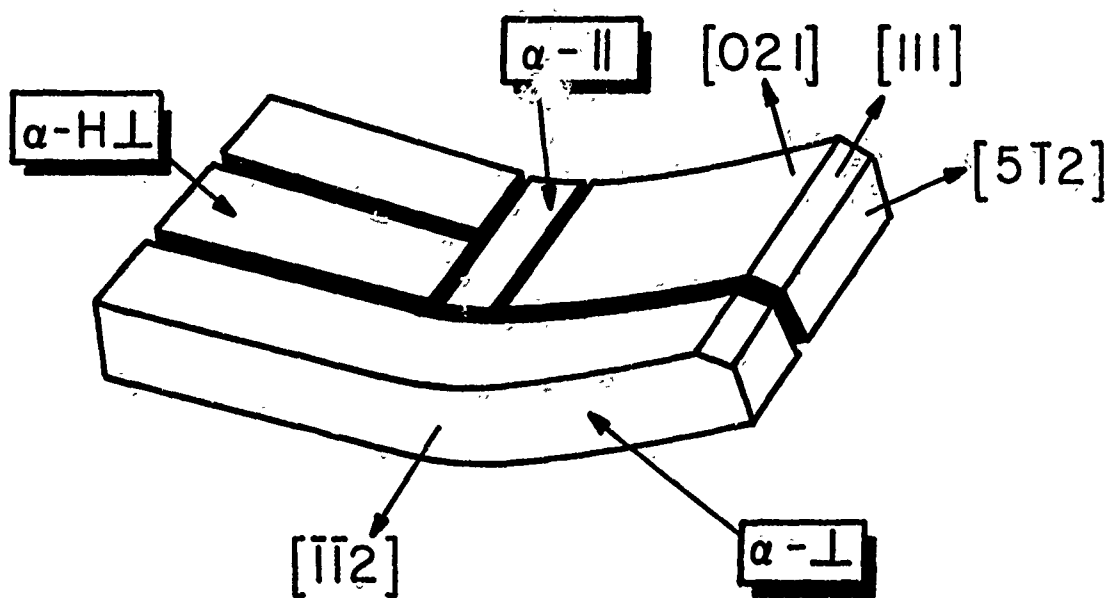
Previously, we reported [1] that after plastic deformation of GaAs, a decrease was noted in the mobility and conductivity of the samples. Because of the impurities present and the significant effects of short term heating on the control (unbent) samples, it was not possible to separate impurity effects from purely dislocation effects.

Based on the assumption that heating and bending would cause a migration of impurities towards dislocations in the bent samples, it was planned to measure the mobility and conductivity in a direction parallel and perpendicular to the $[112]$ bend axis, thus detecting the directionality, if any, of the electrical properties of dislocations with impurities.

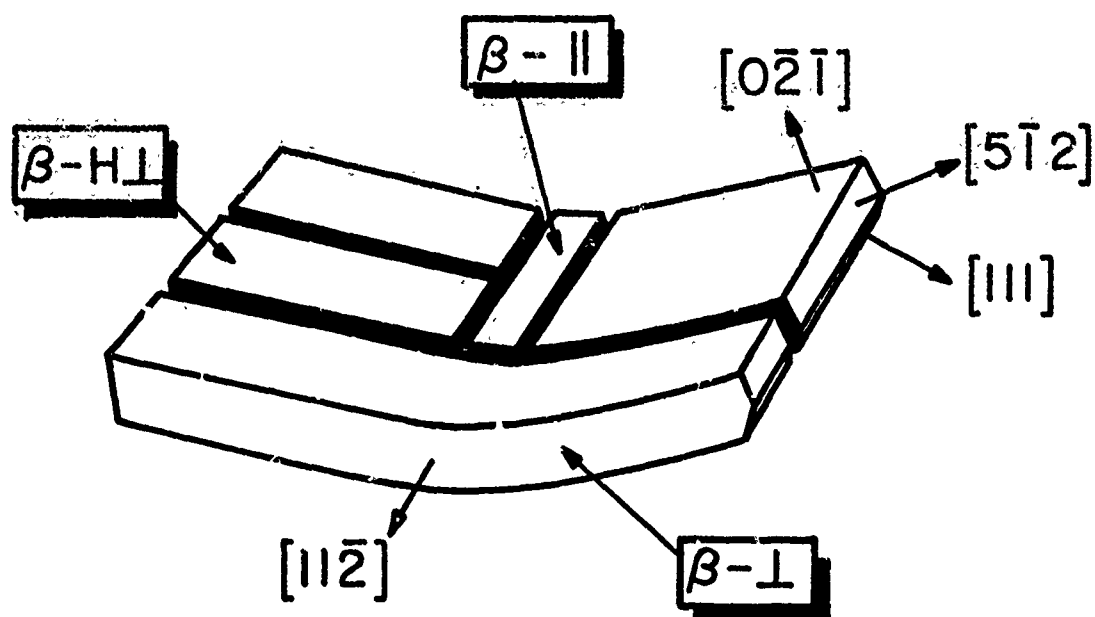
Figure 37 shows how two adjacent slices of Te-doped (10^{17} cm^{-3}) Czochralski GaAs (CZ-16) were oriented to introduce single slip after four-point bending and to produce an excess of α - or β -dislocations. The figure also shows how each sample was cut to obtain sections parallel and perpendicular to the bend axis. In addition, a sample labeled "H \perp " (heated, perpendicular) was cut with the intention of providing a control sample from the same slice. It turned out, however, that the deformation extended to these samples such that their Hall curves approximated those for the α - \perp and β - \perp . Hence, the data from these samples were not included in the figures. The control samples, A (as-grown) and H (heated) were taken from a slice close to the α -slice and their curves were taken from the previous report [1].

Resistivity and Hall voltages were measured in a 5 kG magnetic field (aligned normal to the bend axis and the electric field) as a function of temperature (83° to 300°K) in a Hall apparatus made available through the courtesy of Dr. H. H. Wieder of the U.S. Naval Electronics Laboratories Center, San Diego.

The Hall parameters for the six samples as a function of reciprocal temperature are shown in Figures 38-40. Figure 38 shows that after heating no changes took place in the carrier concentration of the control samples, thus indicating an absence of contamination during the heating process. All the bent samples exhibited decreases in carrier concentration relative to the heated, unbent sample H, with the β -samples showing a larger decrease than the α -samples. A comparison of the α - \perp with



(a)



(b)

Figure 37: Schematic diagram of the orientation of Te-doped GaAs (CZ-16) samples relative to the $[1\bar{1}2]$ bend axis to introduce: (a) an excess of α -type dislocations and (b) an excess of β -dislocations. The samples were then cut to obtain slices perpendicular ($\alpha-\perp$, $\beta-\perp$) or parallel ($\alpha-\parallel$, $\beta-\parallel$) to the bend axis. The samples labeled $\alpha-H\perp$ and $\beta-H\perp$ represent heated-perpendicular slices.

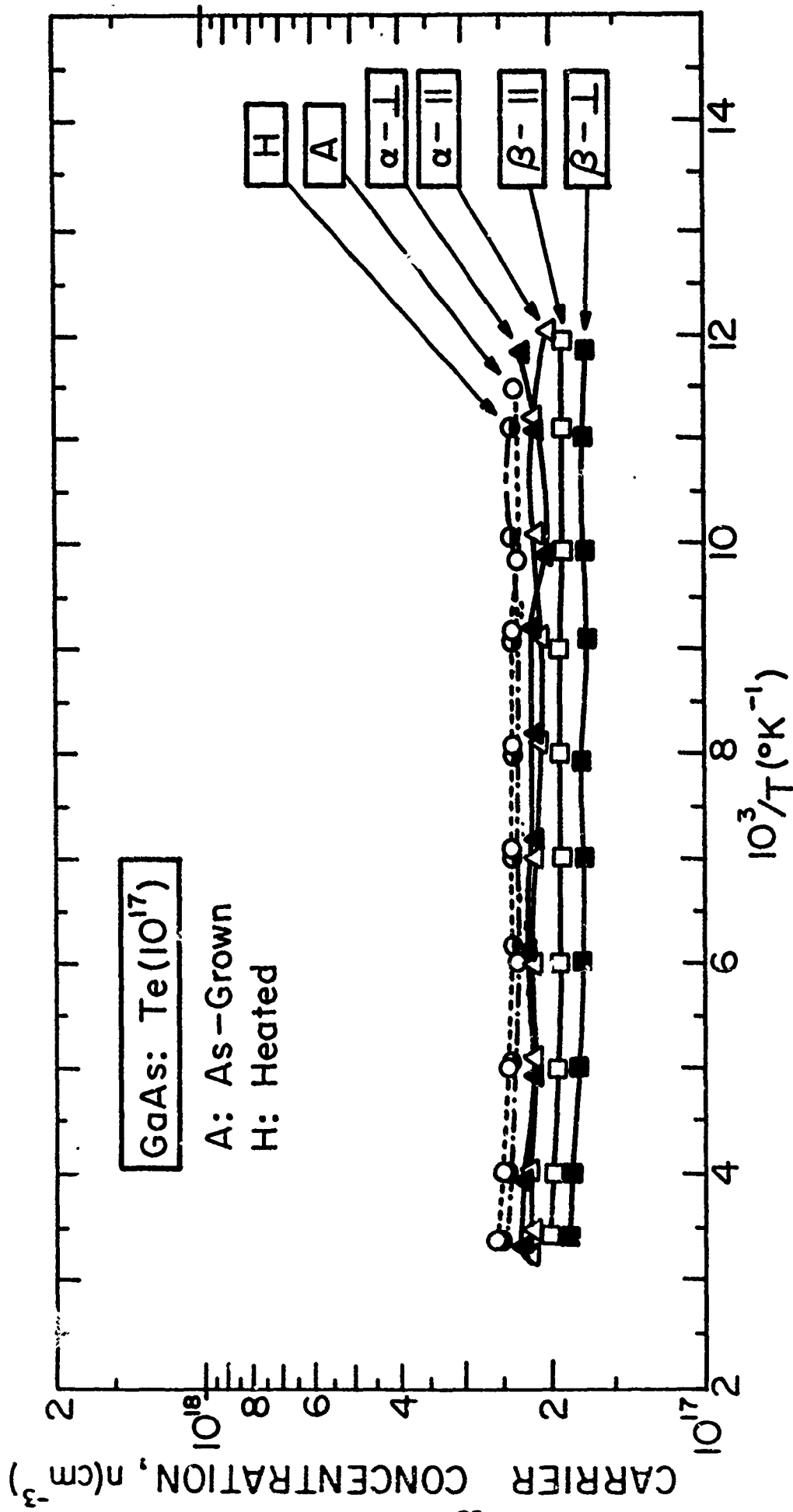


Figure 38: Carrier concentration vs. reciprocal absolute temperature for the as-grown (A), heated (H) and bent (α , β) samples which were measured parallel (\parallel) or perpendicular (\perp) to the bend axis (CZ-16).

$\alpha - \parallel$ shows that these two exhibited decreases in carrier concentration of 5 and 16 per cent, respectively, while the $\beta - \perp$ showed a decrease of 28 per cent compared to the 20 per cent decrease of $\beta - \parallel$ (Table VIII). While the differences between the carrier concentrations in the parallel and perpendicular samples for the same type of dislocation are not significant, the decrease in carrier concentration relative to the heated control strongly suggests the introduction of acceptor sites in the bent $\alpha -$ and $\beta -$ samples.

Figure 39 shows the changes in mobility after bending, particularly in the $\beta - \parallel$ sample. The effect of heating (relative to the as-grown condition) has been to decrease the mobility in sample H. Relative to the heated control, the effect of bending has been to decrease the mobility of the $\alpha - \perp$ and $\beta - \perp$ by 18 and 8 per cent, respectively--a decrease reflected in the corresponding drop of 19 and 34 per cent in conductivity (Figure 40). This decrease in mobility and conductivity in the perpendicular direction (which was reported previously [1]) has been directly related to the scattering, either specular [18] or diffuse [19] or both at the dislocations acting as space charge tubes.

What is remarkably significant is the dramatic increase (relative to the heated control sample) in mobility (118%) and conductivity (73%) in the $\beta - \parallel$ samples. A brief review of work by other investigators (Table IX) on the anisotropy of electrical properties in semiconductors shows that the mobility in the \parallel -direction is either equal to [20] or slightly less than the mobility of the control sample [21]. Read [28] assumed

TABLE VIII

Per Cent Change (Relative to the Heated Sample) in the
Hall Parameters of the Bent Te-doped (10^{17}cm^{-3})
GaAs Sample (CZ-16)

No.	Sample No.	Disloc'n Type & Direction	Per Cent Changes in:		
			Carrier Conc'n	Mobility	Conductivity
1	11-E1	$\alpha - \perp$	-5	-18	-19
2	11-E1	$\alpha - \parallel$	-16	+29	+11
3	12-E2	$\beta - \perp$	-28	-8	-34
4	12-E2	$\beta - \parallel$	-20	+118	+73

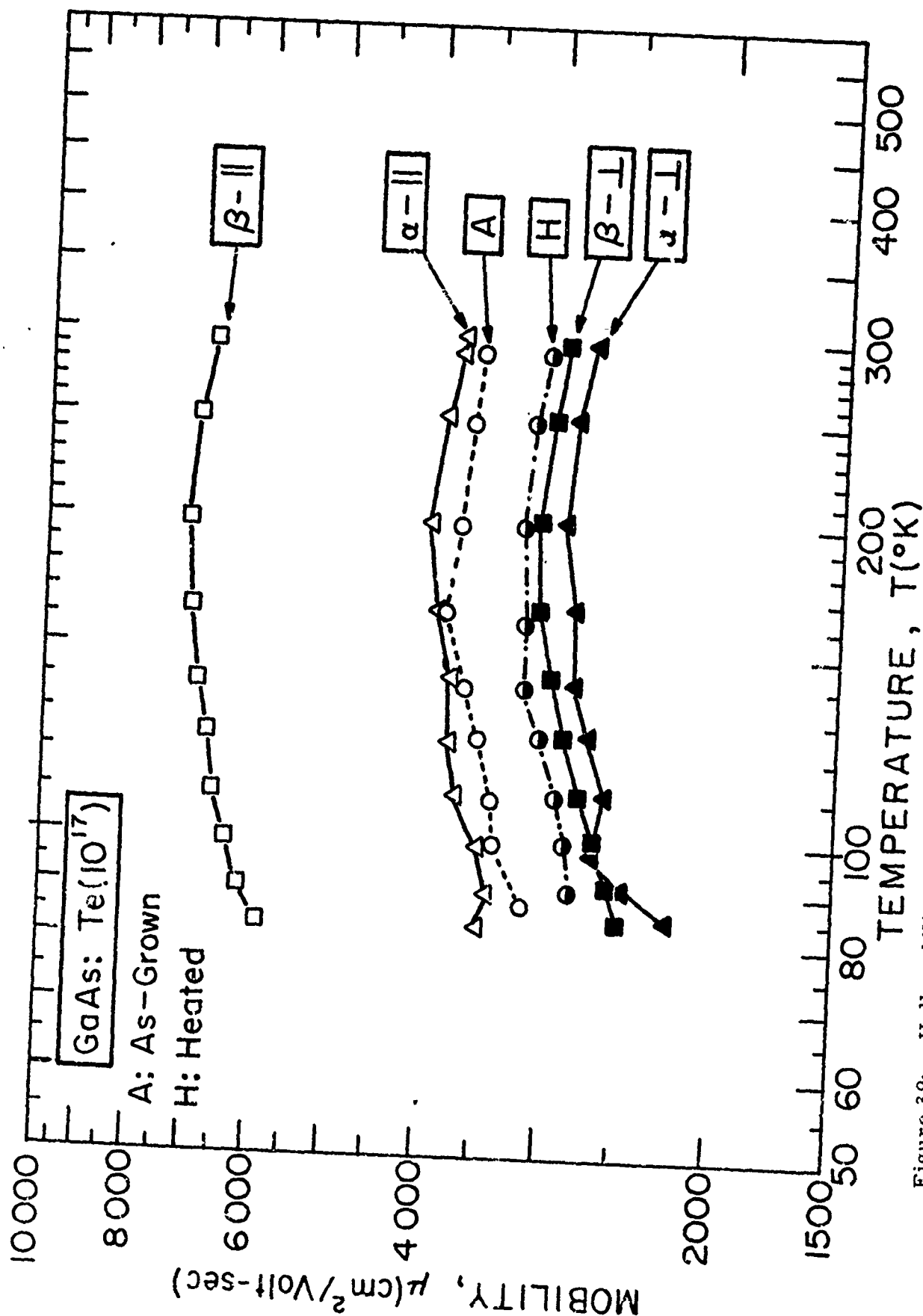


Figure 39: Hall mobility vs. reciprocal absolute temperature for the as-grown (A), heated (H) and bent samples (α -||, α -⊥, β -||, β -⊥) (CZ-16).

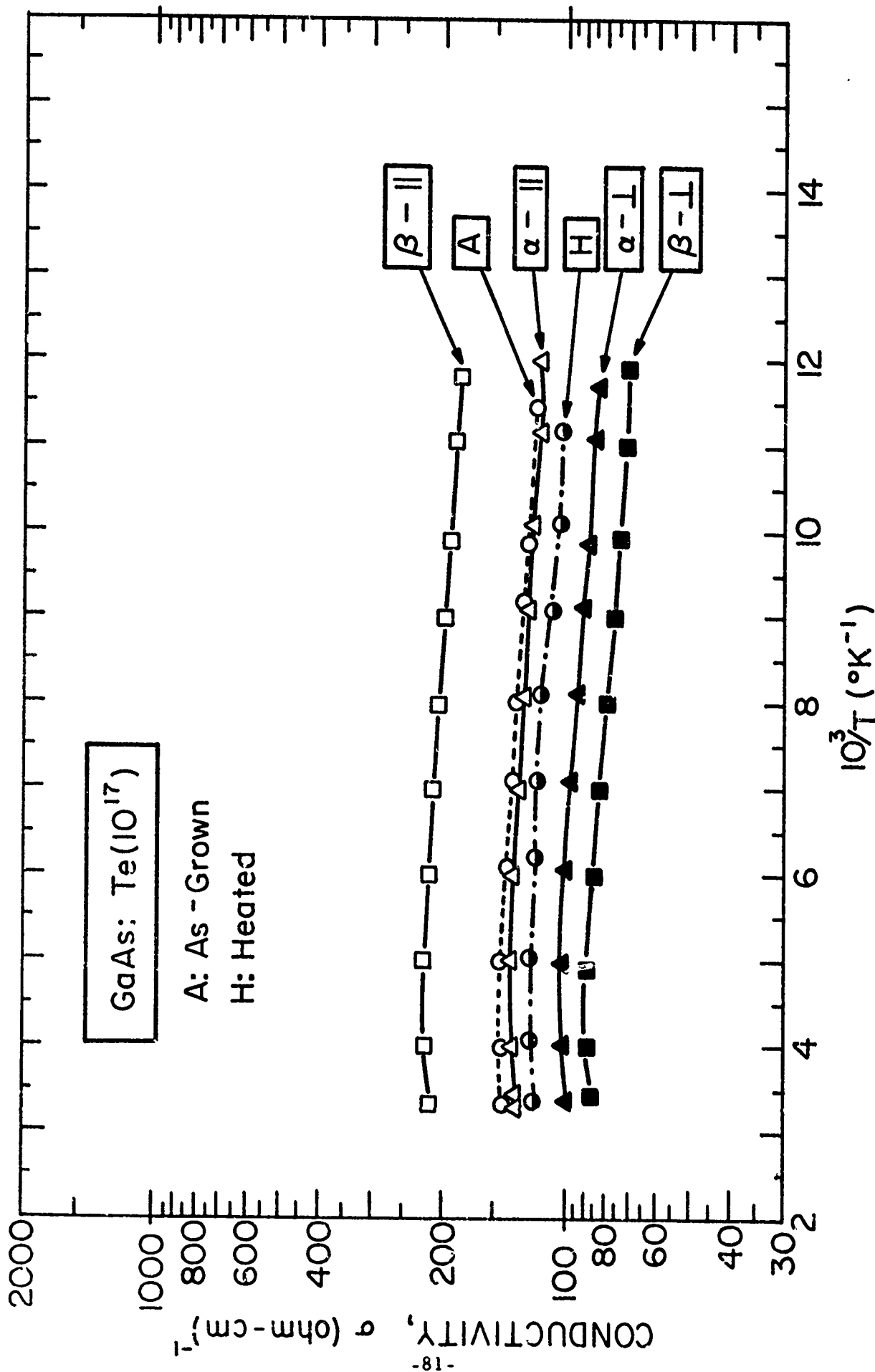


Figure 40: Conductivity vs. reciprocal absolute temperature for the as-grown (A), heated (H) and bent samples ($\alpha - \parallel$, $\alpha - \perp$, $\beta - \parallel$, $\beta - \perp$) (CZ-16).

TABLE IX

Summary of the Anisotropic Character of the Conductivity, Carrier Concentration and Mobility of Bent Semiconductor Crystals

No.	Semi-conductor Mat'l	Net Carrier Conc'n, Nd-Na (cm^{-3})	Excess Disloc'n Type	Disloc'n Energy Levels Ec-Edis (eV)	Type of Disloc'n Level	Anisotropic Behavior in:			Reference
						Conductivity	Carrier Conc'n	Mobility	
1	Ge	2×10^{14}	(a)	0.20	Acceptor	$\sigma_{\parallel} < \sigma_o$ $\sigma_{\perp} < \sigma_{\parallel}$	$n_{\parallel} = n_o$ $n_{\perp} < n_{\parallel}$	$\mu_{\parallel} = \mu_o$ $\mu_{\perp} < \mu_{\parallel}$	20
2	Ge	3.5×10^{14}	(a)	0.50	Acceptor	$\sigma_{\parallel} < \sigma_o$ $\sigma_{\perp} < \sigma_{\parallel}$	$n_{\parallel} < n_o$ $n_{\perp} > n_{\parallel}$	$\mu_{\parallel} < \mu_o$ $\mu_{\perp} < \mu_{\parallel}$	19
3	InSb	8.33×10^{13}	α (In)	0.12	Acceptor	$\sigma_{\parallel} < \sigma_o$ $\sigma_{\perp} < \sigma_{\parallel}$	$n_{\parallel} < n_o$ $n_{\perp} = n_{\parallel}$	$\mu_{\parallel} < \mu_o$ $\mu_{\perp} < \mu_{\parallel}$	21
			β (Sb)	0.22	Acceptor	$\sigma_{\parallel} < \sigma_o$ $\sigma_{\perp} < \sigma_{\parallel}$	$n_{\parallel} < n_o$ $n_{\perp} = n_{\parallel}$	$\mu_{\parallel} < \mu_o$ $\mu_{\perp} < \mu_{\parallel}$	
4	GaAs (Te-doped)	2.5×10^{17}	α (Ga)	(b)	Acceptor	$\sigma_{\parallel} > \sigma_o$ $\sigma_{\perp} < \sigma_{\parallel}$	$n_{\parallel} < n_o$ $n_{\perp} > n_{\parallel}$	$\mu_{\parallel} > \mu_o$ $\mu_{\perp} < \mu_{\parallel}$	This Work
			β (As)	(b)	Acceptor	$\sigma_{\parallel} \gg \sigma_o$ $\sigma_{\perp} < \sigma_{\parallel}$	$n_{\parallel} < n_o$ $n_{\perp} < n_{\parallel}$	$\mu_{\parallel} \gg \mu_o$ $\mu_{\perp} < \mu_{\parallel}$	

(a) Not indicated.

(b) Not determined.

in his theory that only the perpendicular component of the momentum vector of the electrons will be scattered by the charged cylinder and that the parallel component should remain unaffected. Nowhere has it been predicted that the parallel component will be enhanced.

One principal difference between the earlier work on deformed Ge [20] and InSb [21] and the present study is the higher impurity concentration present in bulk grown GaAs. Hence, to explain the increase in the parallel mobility, one must include the role of impurities in the heating and bending process. Because of the fact that after heating no change was observed, while after bending there was a decrease in carrier concentration in both the parallel and perpendicular directions, it is highly probable that the combined process of heating and bending produced a migration of impurities to the dislocations and/or a sweeping away of the impurities by the dislocations. Thus, areas between neighboring dislocations would be cleared of impurities, while regions near or at the dislocations would have a high concentration of impurities. As a result, there would be in the sample an inhomogeneous distribution of impurities which could produce the high apparent mobilities predicted and observed by Wolfe et al. [22] in inhomogeneous semiconductors.

On the basis of dislocation densities of the order of 10^7 cm^{-2} and assuming a uniform distribution of dislocations at the center of the bend (as indicated by the uniform array of black dots in the IR-CL micrographs), there would be a separation distance of 3μ between dislocation centers. Using Read's [28] estimate of 1μ as the typical diameter of

the space charge cylinders, the actual space between the outer surfaces of the cylinders would then be $2\ \mu$. If this $2\ \mu$ region were swept clean of impurities, it would not be unreasonable to expect a corresponding increase in mobility and conductivity in the parallel direction as indeed has been observed for both the α -|| and β -|| GaAs samples.

B. Si Local Modes in GaAs

Pat Leung

Local mode absorption is a very useful tool for studying the nature of defects in semiconductors. From the experimentally observed band frequency, strength, carrier concentration dependence, symmetry considerations, etc., the defect species for a particular local mode can be identified. Si-doped GaAs is a particularly interesting case since Si is an amphoteric impurity in GaAs, i. e., it can go substitutionally on the Ga site to form a donor (Si_{Ga}) or on the As site to form an acceptor (Si_{As}). In addition, there is the possibility of formation of Si-Si pairs and other complexes. Previous experimental studies on Si-doped GaAs [23,24] have revealed many local mode absorption bands and have attributed them to Si_{Ga} , Si_{As} , $\text{Si}_{\text{Ga}} - \text{Si}_{\text{As}}$, $\text{Si}_{\text{Ga}} - \text{Li}_{\text{Ga}}$, etc. This work attempts to verify some of these band assignments, particularly those due to the $\text{Si}_{\text{Ga}} - \text{Si}_{\text{As}}$ pairs, by introducing a different silicon isotope (^{30}Si) as a dopant, singly and in combination with natural silicon (^{28}Si).

The main problem involved in performing this study was the preparation of the material with controlled ^{30}Si doping. To achieve this,

the crystal had to be grown in a system relatively free of Si contamination from the system. The liquid-seal Czochralski technique offered this advantage. In addition, it was necessary to prevent the dopant from being oxidized before the material was reacted. Several trial runs were made, with no signs of oxides being formed, and the resultant crystals had the expected doping concentration. A total of four ingots with ^{30}Si doping were grown with this liquid-seal Czochralski technique: (1) $[^{30}\text{Si}] \sim 2 \times 10^{18}/\text{cm}^3$ at front end, (2) $[^{30}\text{Si}] \sim 2 \times 10^{19}/\text{cm}^3$, (3) and (4) $[^{30}\text{Si}] + [^{28}\text{Si}] \sim 2 \times 10^{19}/\text{cm}^3$ and approx. equal concentrations.

Local mode measurements were performed on these samples after they had been diffused with ^6Li to compensate the free carriers. The absorption spectrum of sample 1 indicates some ^{28}Si contamination--bands due to ^{28}Si were noted. This was probably due to the use of a seed previously used for growth with ^{28}Si doping. Absorption of sample 2 shows no noticeable bands due to ^{28}Si . In this case, the bands previously observed in ^{28}Si -doped GaAs at 367, 374, 379, 384, 393, 399, 405, 464. cm^{-1} due to $\text{Si}_{\text{Ga}} - \text{Si}_{\text{As}}$, $\text{Si}_{\text{Ga}} - \text{Li}_{\text{Ga}}$, $\text{Si}_{\text{Ga}} - \text{Li}_{\text{Ga}}$, Si_{Ga} , $\text{Si}_{\text{Ga}} - \text{Si}_{\text{As}}$, Si_{As} , $\text{Si}_{\text{Ga}} - \text{Li}_{\text{Ga}}$, $\text{Si}_{\text{Ga}} - \text{Si}_{\text{As}}$, etc., shifted to 356, 365, 369, 373, 383, 388, 394, 449 cm^{-1} , respectively. The shifts were close to the isotopic shift in the simple harmonic oscillator approximation. Sample 3 represented the first attempt to grow a crystal with approx. equal concentrations of $[^{28}\text{Si}]$ and $[^{30}\text{Si}]$. This was done by adding a small GaAs charge and ^{28}Si to the remainder of the previous ingot. Absorption measurements indicated that ^{30}Si was low and that $[^{28}\text{Si}] \cdot [^{30}\text{Si}] \approx 2 : 1$. Probably

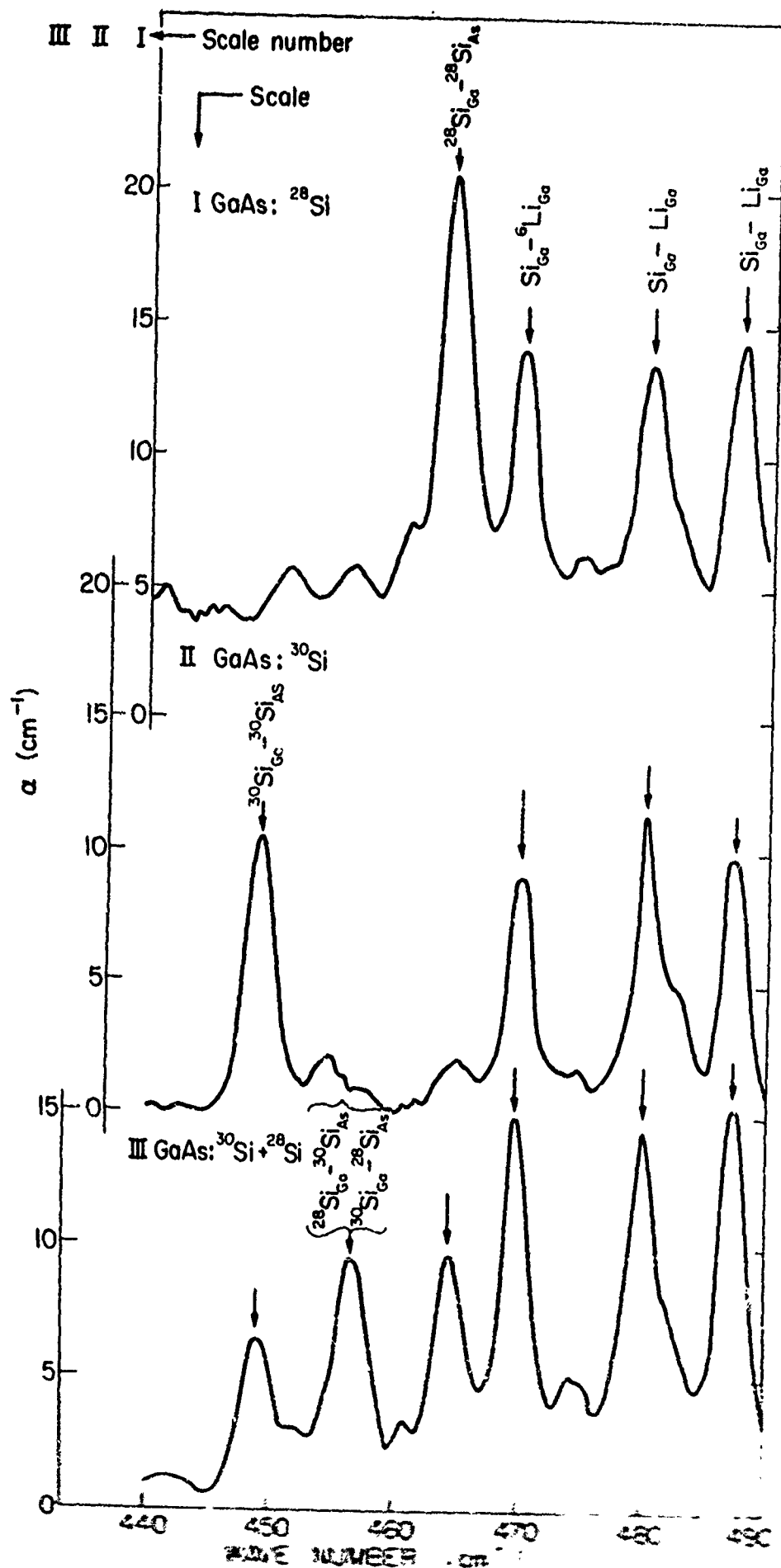


Figure 41: Absorption coefficient vs. frequency for three GaAs samples at liquid nitrogen temperatures.

the difficulty was in determining how much of the previous ingot was already used. Another ingot was then pulled with a small amount of ^{30}Si added. The results of sample 4 indicated $[^{30}\text{Si}]:[^{28}\text{Si}] \approx 1:1$.

The absorption spectrum for the sample with mixed Si-isotopes doping showed the presence of all the bands in the ^{28}Si -doped and ^{30}Si -doped samples. Because of the many overlapping bands at the same or nearly the same frequencies, it was impossible to pick out the mixed-isotope bands at the lower frequencies (350 to 420 cm^{-1}). Therefore, the band at 464 cm^{-1} was chosen for the analysis since it presented an unambiguous picture.

Figure 41 shows the composite plot of the liquid nitrogen temperature absorption coefficient vs. frequency for sample I (CZ-99, ^{28}Si -doped, ^6Li diffused), sample II (CZ-55, $^{30}\text{Si} + ^{28}\text{Si}$ -doped, ^6Li -diffused) and sample III (CZ-51, ^{30}Si -doped, ^6Li -diffused). The bands at 470, 480, 487 cm^{-1} are due to ^6Li vibrations of the $\text{Si}_{\text{Ga}} - ^6\text{Li}_{\text{Ga}}$ pairs, and they were present in all three samples. The band at 464 cm^{-1} for sample I was shifted to 449 cm^{-1} . This shift of 15 cm^{-1} was as expected from the isotopic change. For sample III, the bands at 464 cm^{-1} and 449 cm^{-1} were both present. In addition, there was an intermediate band at 456 cm^{-1} .

Previous studies [23,24] showed that the bands at 367, 393, 464 cm^{-1} are from the same defect. The interpretation was that they are due to $\text{Si}_{\text{Ga}} - \text{Si}_{\text{As}}$ pairs. Pfeuty and Elliott [25] calculated the frequencies of the modes for this defect at 327, 369, 390, 419 cm^{-1} . The

lowest frequency band has not been observed since it is near the reststrahl. The experimentally observed frequencies of the two middle bands at 367 and 393 cm^{-1} are very close to those predicted. The 464 cm^{-1} is substantially larger than the calculated $\omega = 419 \text{ cm}^{-1}$, but this is the out-of-phase axial mode and its frequency should be extremely sensitive to the $\text{Si}_{\text{Ga}} - \text{Si}_{\text{As}}$ force constant which was not included in the calculation. Moreover, the overall splitting of these bands indicates a very strong coupling interaction, probably due to nearest neighbors, as compared to the much smaller splitting of the 374, 379, 405 cm^{-1} bands for the substitutional neighbor pairs $\text{Si}_{\text{Ga}} - \text{Li}_{\text{Ga}}$. Although the interpretation is satisfactory, there remains the possibility that the bands at 367, 393, 464 cm^{-1} may be due to other complexes.

The presence of the intermediate band for sample III with the mixed $^{28}\text{Si} + ^{30}\text{Si}$ doping clearly establishes the fact that there was more than one silicon in the defect, since only the shifted band at 449 cm^{-1} would be expected if the defect involved only one silicon. The presence of one intermediate band with the frequency in the middle between the two pure isotope bands is only compatible with the model of two atoms in the defect with equivalent sites [26]. A three atom model with equivalent sites gives at least two intermediate bands. In this particular case, the two sites in the defect may be slightly inequivalent. There may have been two bands too close in frequency to be resolved, giving rise to the larger half-width of the intermediate band compared to the two pure isotope bands. A theoretical calculation is being carried out to predict the frequencies of

$^{30}\text{Si}_{\text{Ga}} - ^{28}\text{Si}_{\text{As}}$ and $^{28}\text{Si}_{\text{Ga}} - ^{30}\text{Si}_{\text{As}}$ and the equivalency of the two sites.

The experimental results for the ^{28}Si -doped and the corresponding ^{30}Si -doped and $^{30}\text{Si} + ^{28}\text{Si}$ doped samples clearly show the 464 cm^{-1} band and therefore also the 367 cm^{-1} and 393 cm^{-1} bands are due to the nearest neighbor $\text{Si}_{\text{Ga}} - \text{Si}_{\text{As}}$ pairs.

C. Infrared Modulation of Cathodoluminescence

Wen N. Lin and David B. Wittry

The effect of light on the cathodoluminescence of Czochralski grown, Cr-doped semi-insulating GaAs single crystal was studied as a function of wavelength [27]. The experiments were performed at 300°K and 114°K . Steady light from a 150 watt quartzline lamp (color temperature 3200°K) passed through a Hilgen and Watts D292 plane grating monochromator and was focused on the sample at the same position as the electron beam. Using a $0.38\text{ }\mu\text{A}$, 20 KV electron beam, the light induced a change in cathodoluminescence as a function of wavelength as shown in Fig. 42. With wavelength λ longer than about $1.6\text{ }\mu$, (0.77 eV), only a small increase in cathodoluminescence was observed. As λ became shorter than $1.6\text{ }\mu$, the cathodoluminescence increased rapidly with decreasing λ . No change of cathodoluminescence was observed in undoped high resistivity GaAs. Cr is known to introduce an acceptor level in GaAs at about 0.8 eV below the conduction band. The observed change of cathodoluminescence in Cr-doped GaAs may be attributed to the excitation of electrons from Cr level to the conduction band since

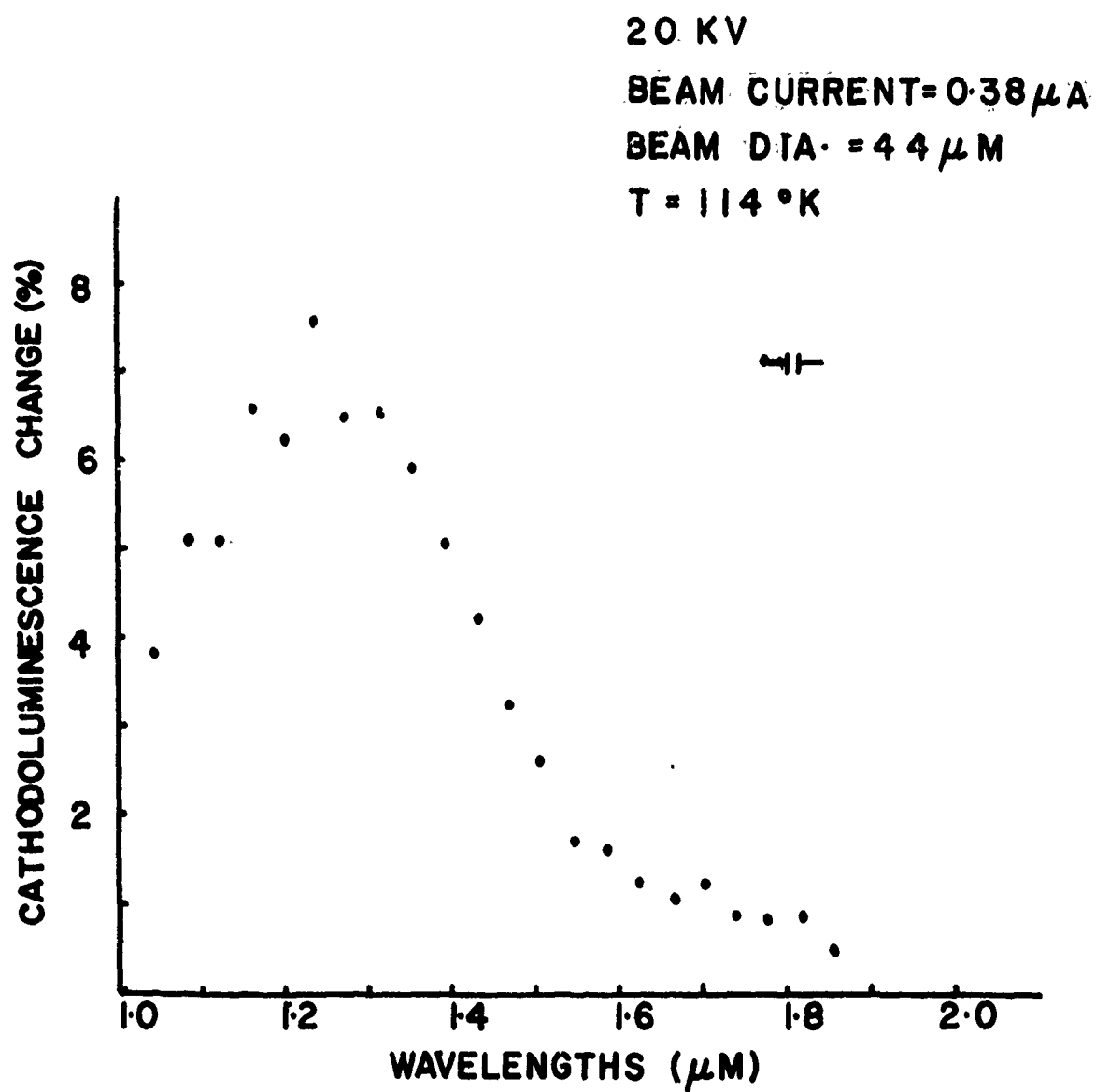


Figure 42: Cathodoluminescence change as a function of wavelength.

ionized Cr atoms are efficient hole traps.

Figure 43 shows the light-induced change of sample current as a function of wavelength using a 10 KV, 0.44 μ A electron beam at 114°K. With wavelength λ longer than 1.6 μ , only a small increase in sample current was observed. As λ became shorter than 1.6 μ , the sample current increased rapidly with decreasing λ . The observed change in sample current may also be attributed to the excitation of electrons from the Cr level to the conduction band, resulting in an increasing of conductivity of the semi-insulating GaAs: Cr and changes in the surface charging state in such a way as to increase the efficiency of collecting secondary electrons from the surface.

From that shown above, it is seen that by choosing a proper beam voltage and current, the light-induced change of cathodoluminescence and sample current can be used to detect deep impurity levels in semiconductors.

D. Cathodoluminescence of GaAs, GaP, and GaAs_{1-x}P_x

Hans C. Marciniak and David B. Wittry

In this work cathodoluminescence spectra are being studied at various temperatures and electron beam current densities for GaAs, GaP, and GaAs_{1-x}P_x alloys near the direct-indirect crossover point in order to provide better understanding of the recombination processes. Preliminary results were shown in the previous report [1] and were presented at the 7th National Conference on Electron Probe

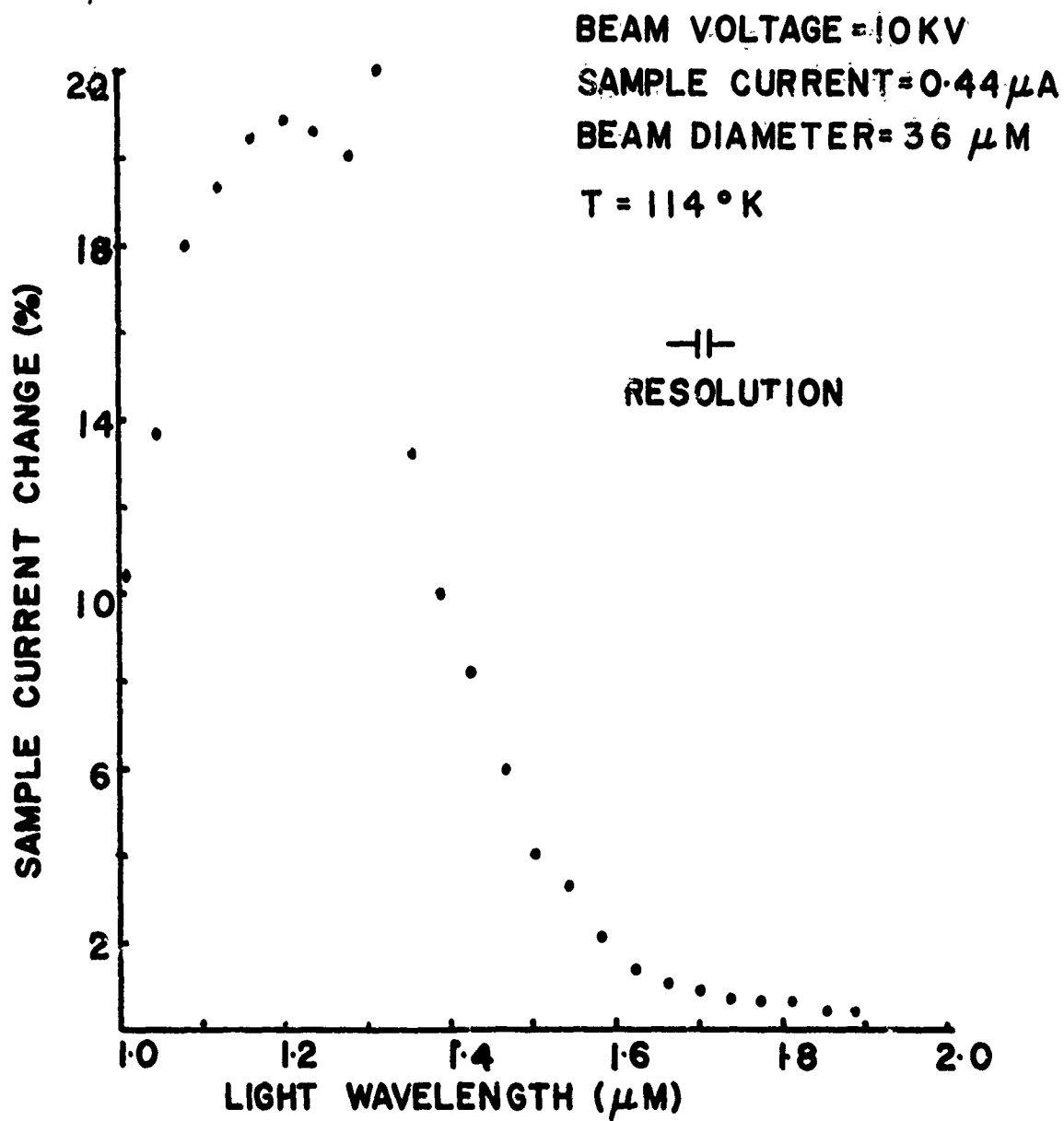


Figure 43: Sample current change as a function of wavelength.

Microanalysis [28].

Recently, samples of GaAs-GaP alloys were obtained from Bell and Howell, Pasadena, California. More information is available on the dopant species and concentration for these samples than for those previously studied. Results from measurements on these specimens should be easier to interpret in terms of theoretical models than results obtained on specimens studied previously. This work is now in progress.

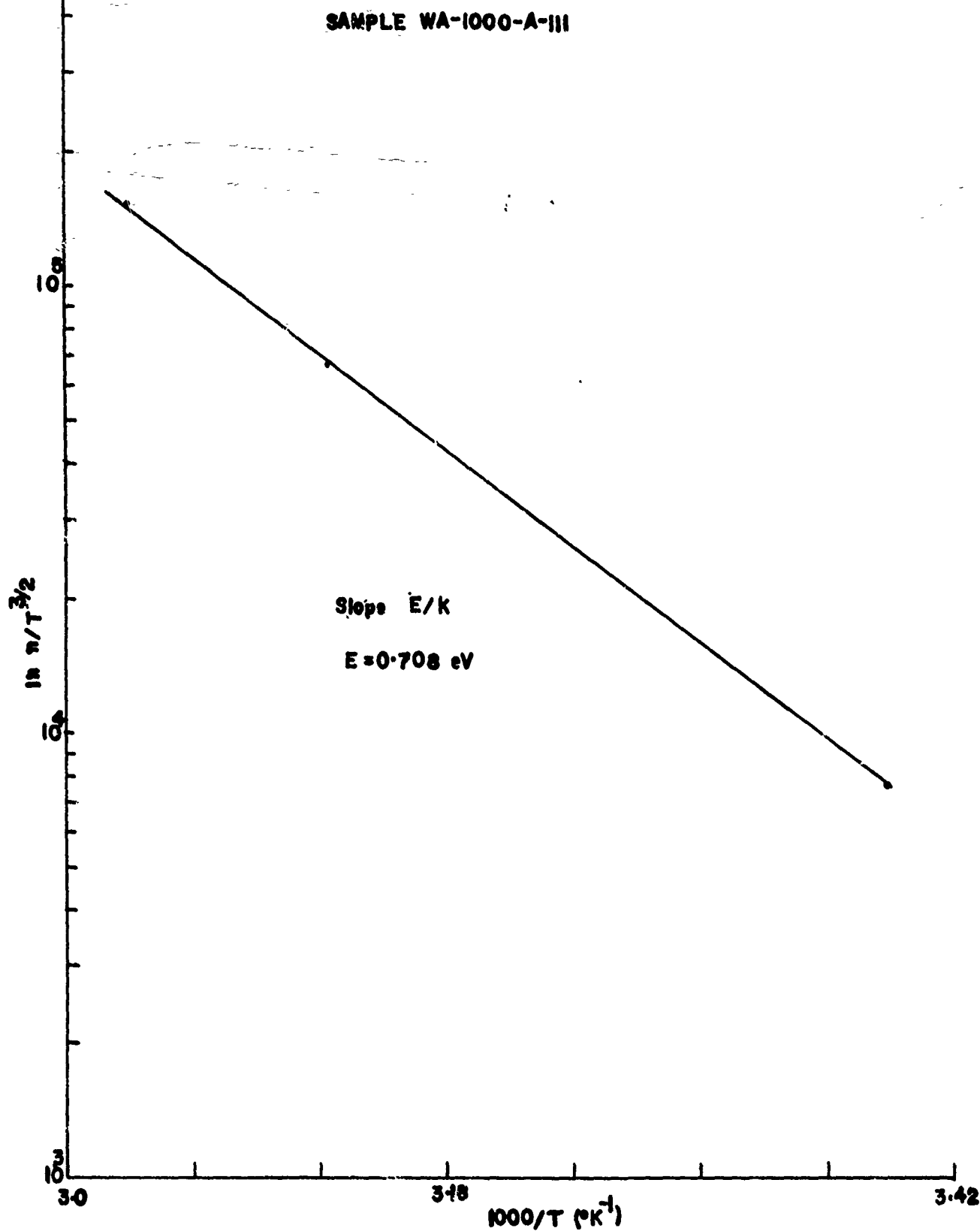
E. High Impedance Hall System

Sharad Joshi and Clarence R. Crowell

A knowledge of the Hall coefficient and its temperature dependence provides an essential tool for the characterization of semiconductor materials, since the carrier activation energy and mobility may thus be determined. It is essential for this purpose to know the temperature of the Hall sample accurately. During this period we completed an integration of our high impedance Hall system with a Janis variable-temperature cryostat. In this system, temperature is specified in terms of the resistance of a platinum resistance sensor, which is also incorporated in the circuitry at the temperature controller. We have investigated errors due to sample placement relative to the sensor and the dependence on the flow rate of the exchange gas which provides cooling and also influences the heater power required.

The platinum resistance thermometer in the Hall cryostat was calibrated against another calibrated platinum sensor, using an extended

Figure 44: Hall-effect carrier concentration vs. reciprocal temperature for high resistivity GaAs, grown by the horizontal Bridgman method without intentional doping. Energy level from slope corresponds to Cr.



Callender-van Dusen equation [29]. The two temperature sensors were then used to obtain a table of potentiometer setting on the temperature controller vs. temperature at the sample position with no flow of the exchange gas.

The potentiometer circuit of the temperature controller was modified to extend the high accuracy range below $\approx 300^{\circ}\text{K}$ to include the temperature range up to 400°K .

The difference in temperature between the sample position and the sensor position for a finite flow of exchange gas and medium power dissipation (1.25 watts at liquid nitrogen temperature) was less than 0.02°K . Thus, with the present arrangement the absolute temperature can be set and controlled within an accuracy of about 0.05°K . The temperature controller gives a clean indication of temperature differences of 0.01°K .

The system is now being routinely used to characterize GaAs material being grown here. The samples are prepared in a square Van der Pauw configuration. The ohmic contacts are made by evaporating AuGe onto the corners of the square and alloying them at 450°C for 30 seconds in a forming-gas ambient. Temperature vs. Hall effect measurements were performed on a number of samples. Figure 44 shows one such sample (WA-1000-AIII) of our typical high resistivity GaAs material. The room temperature resistivity, Hall mobility and carrier concentration of this sample were found to be $1.29 \times 10^8 \Omega \text{ cm}$, $1238 \text{ cm}^2/\text{V sec}$ and $3.91 \times 10^7 \text{ cm}^{-3}$, respectively. The activation energy

obtained from this plot was 0.708 eV, assuming that the material was compensated by deep impurities [30]. Typical low resistivity samples (CZ-36 Te doped, CZ-53 undoped) were prepared from GaAs material grown by our Czochralski liquid-seal technique. The temperature dependence of the Hall effect on these samples in the temperature range of 300°K to 77.3°K did not show an appreciable change in the carrier concentration. To detect the shallow impurities, the temperature range of the experiment would have to be extended below 77.3°K. The room temperature resistivities and electron concentrations measured for CZ-36 were 0.0324 Ω cm and $1.08 \times 10^{17} \text{ cm}^{-3}$ respectively. The same parameters measured for CZ-53 were 0.0434 Ω cm and $8.85 \times 10^{16} \text{ cm}^{-3}$, respectively.

F. Schottky Barrier Capacitive Characterization of Impurities

Cheng H. Huang, C. L. Anderson and Clarence R. Crowell

The behavior and concentration of charged impurity states is a critical factor in the operation of charge control semiconductor devices. To this end we have sought to improve the tools for measuring and analyzing the effects of such levels in Schottky barriers. The Schottky barrier has been chosen as a fairly standard configuration because it can be formed with a minimum perturbation of the semiconductor material. A simple, easily applied, theory of the capacitance effects of such impurities has been developed. (This aspect of the work has been funded by the Army Research Office, Durham.) The resulting guidelines

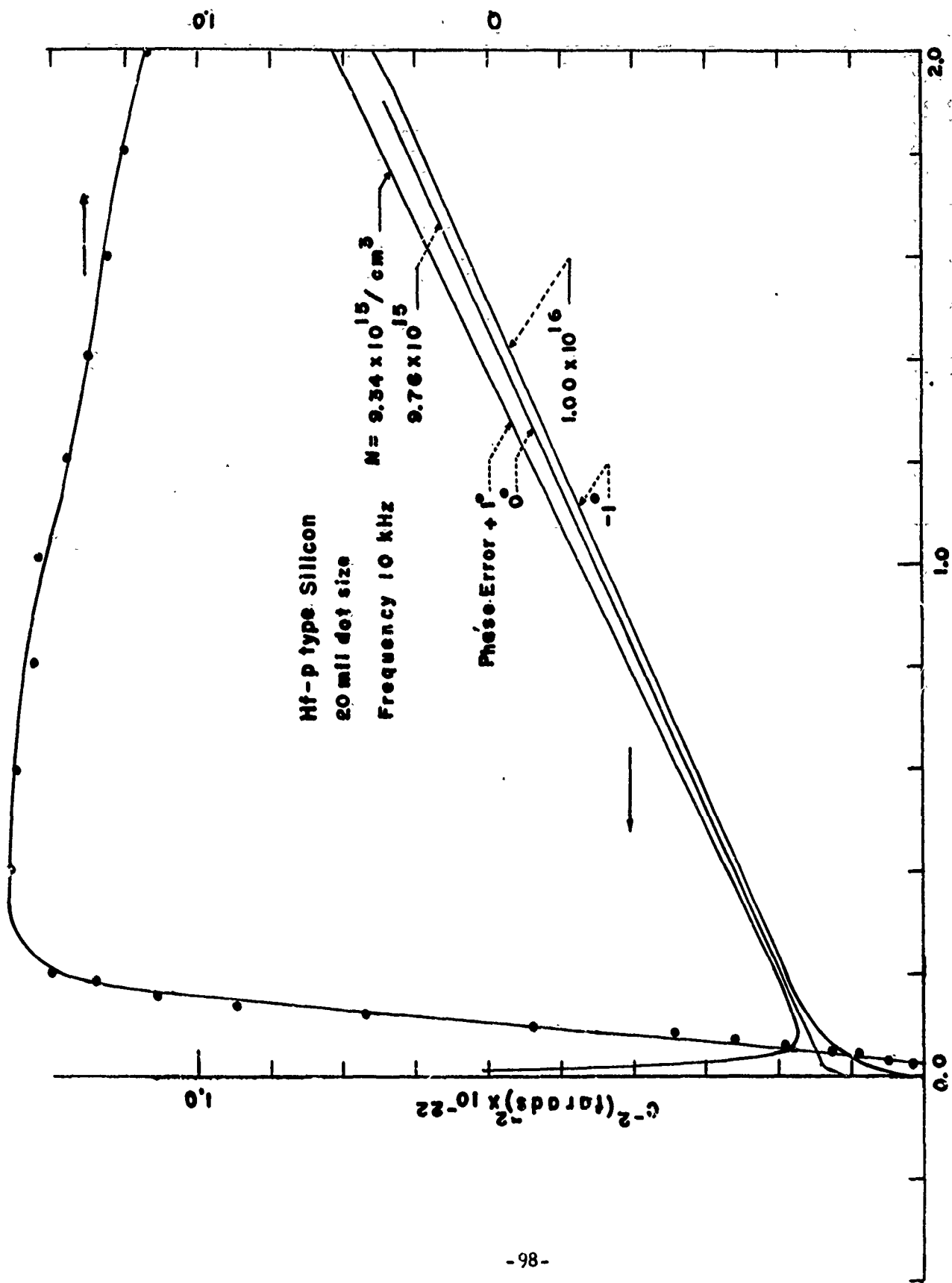
are summarized in the previous report [1]. We have also continued work on measuring equipment for acquiring capacitance-voltage and capacitance-frequency relationships for Schottky barriers.

1. Measurement Facilities

Our electrically balanced measurement system for C-V, C- ω , G-V, and G- ω measurements has undergone considerable testing and calibration during the past six months. The basic circuit guidelines are as outlined in the previous report [1]. We have, however, added a d.c. overload indicator circuit for the preamplifier because the Bridged-T circuit can be saturated by direct current from the device under test without the PAR phase sensitive detector giving a clear indication of the d.c. overload. We also anticipate replacing the PAR 124 with a PAR 129 which has better frequency sweep capabilities and better phase orthogonality. We have also made many minor improvements which add to the ease of use and calibration accuracy of the system. In particular, a phase calibration technique which permits phase orthogonality to $\pm 0.1^\circ$ at a single frequency was developed. A paper describing this system was presented at the International Electron Devices Meeting, December, 1972.

2. Measurements

To determine the instrument's capacity for measurement of capacitance on low Q diodes we made measurements of $1/C^2$ vs. V on a hafnium on p-type Si Schottky diode at 10 Hz (cf. Fig. 45). The diode had a Q on the order of unity over much of this range, but as the bias approached zero the diode capacitance rose rapidly. Note that the proper phase



adjustment of the system is responsive solely to the capacitive portion of the diode admittance for Q values as low as 0.01. Phase errors of $\pm 1^\circ$, however, produce "anomalous" plots of $1/C^2$ vs voltage. Considering the fact that the apparent doping concentration is inversely proportional to the slope of this plot, it is clear that the phase adjustments are critical for measurements on low Q diodes, i.e., for all diodes near zero bias or in the forward bias region.

We also took $1/C^2$ vs. V measurements on a high Q nickel on n-type GaAs diode. This was epitaxial GaAs provided by the Royal Radar Establishment, Great Malvern, U.K. Figure 46 shows the results at various frequencies. The total doping concentration was computed from the results to be $4 \times 10^{15} \text{ cm}^{-3}$ at 120 kHz, $4 \times 10^{15} \text{ cm}^{-3}$ at 10 kHz, and $4.6 \times 10^{15} \text{ cm}^{-3}$ at 100 Hz. We see that the apparent total doping concentration was higher at lower frequency, as expected if deep level impurities were present. We did not see a kink which would be characteristic of a deep level impurity in $1/C^2 - V$ curves as we went down to 0.35 volt forward bias where the diode conductance started to interfere with the capacitance measurement [32]. Thus, the deep level probably lies within 0.5 eV below the conduction band edge unless it had a characteristic response time well below 0.01 second. In this case the level might lie as low as 0.85 eV below the conduction band edge. Still deeper levels would not be detected by this method [33].

To further define the deep level impurity we took $C - \log \omega$ data on a nickel on n-type GaAs diode (Fig. 47). The capacitance indeed showed

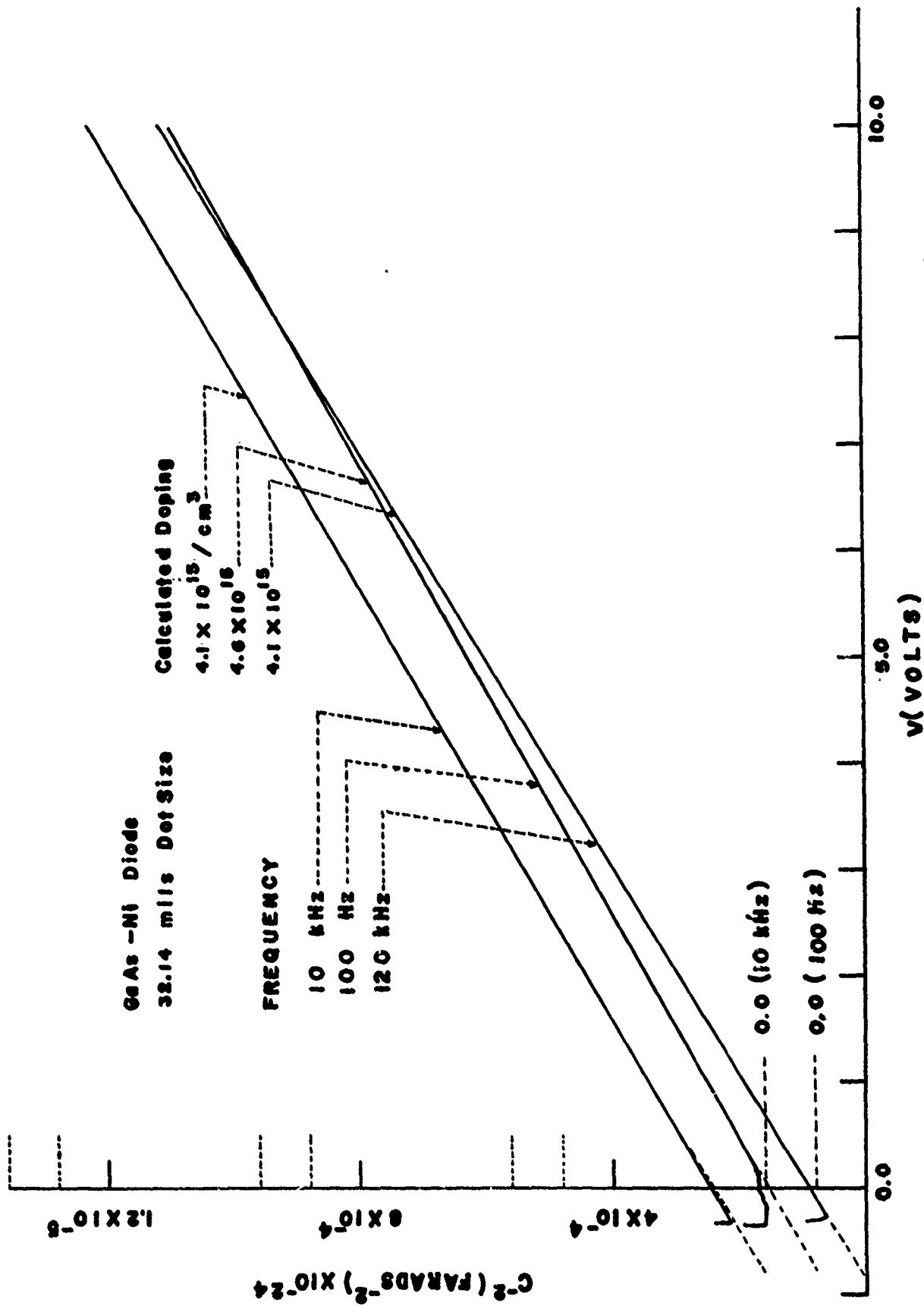


Figure 46: Capacitance-voltage measurements for GaAs diode at various frequencies.

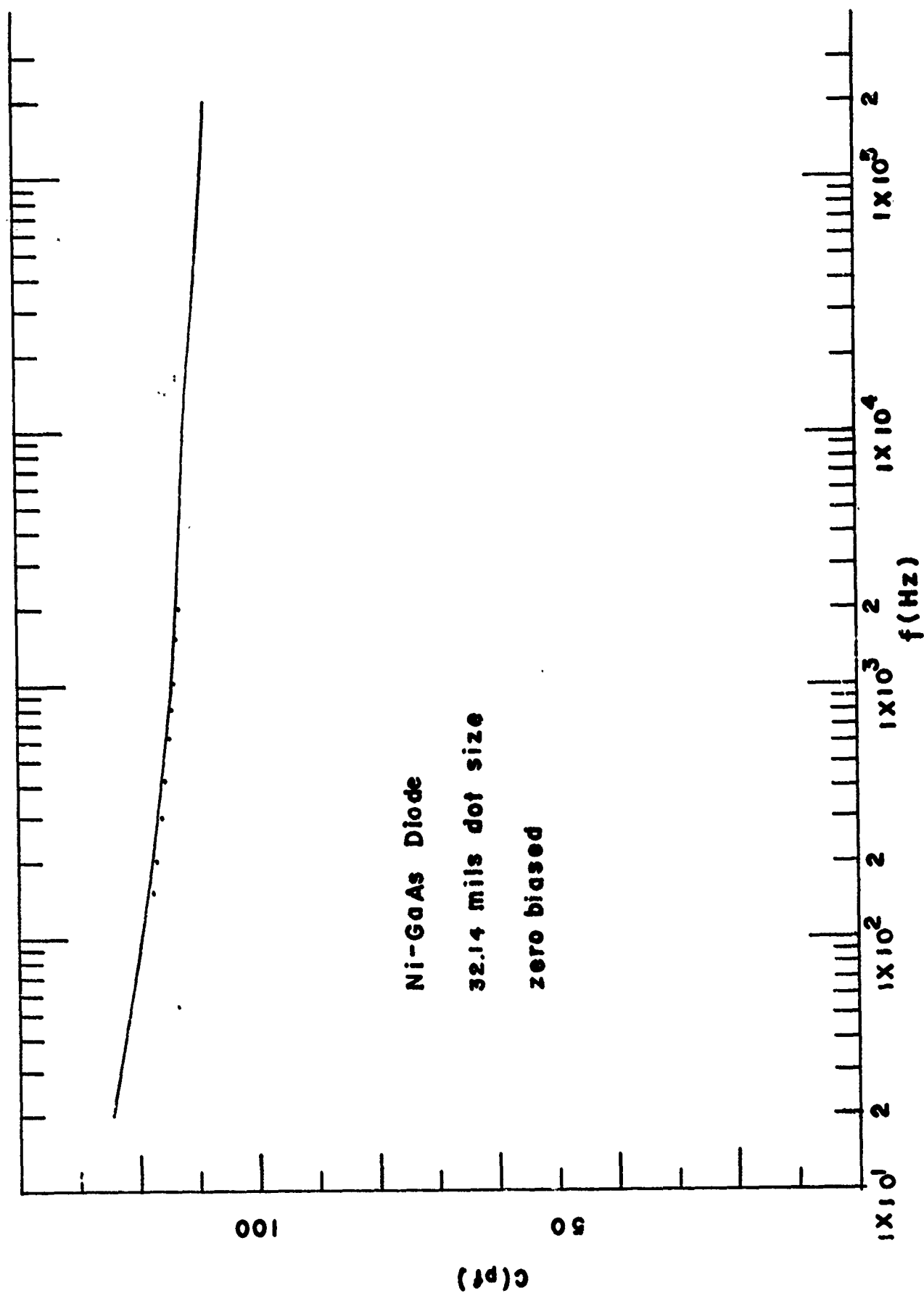


Figure 47: Capacitance-frequency data for GaAs diode.

dispersion in the frequency range from 20 Hz to 200 kHz. Point-by-point measurements were done in the frequency range from 150 Hz to 2 kHz. We found that the agreement was very good, indicating that the phase adjustment was good down to 150 Hz. There appears to be appreciable variation in the corresponding $G-\omega$ relationship which has not yet been completely established.

We have not yet attempted to interpret these data in terms of our theoretical model but anticipate making additional capacitance vs. temperature and impurity profile measurements to assist in our diagnostic approach.

G. Tunnel and Thermal Effects in Photoemission in Schottky Barriers

The work described in the previous progress report [1] has been submitted to Solid-State Electronics [34]. An earlier manuscript which describes an operational equivalent to the Fowler photothreshold plot (without tunneling correction) has been published [35].

REFERENCES

1. "New Methods for Growth and Characterization of GaAs and Mixed III-V Semiconductor Crystals", USCEE Report 423, ARPA, Grant No. DAHC15-71-G6 (1 July 1971 - 30 June 1972).
- * 2. E. S. Johnson and W. P. Allred, Bull. Am. Phys. Soc. 17, 1185 (1972).
- * 3. V. F. Yip and W. R. Wilcox, Bull. Am. Phys. Soc. 17, 1185 (1972).
- * 4. C. E. Chang and W. R. Wilcox, Bull. Am. Phys. Soc.
- * 5. V.H.S. Kuo, "Removal and Separation of Particles by Crystallization",
- * 6. V.H.S. Kuo and W. R. Wilcox, Sep. Sci. (in press).
- * 7. V.H.S. Kuo and W. R. Wilcox, submitted to I & EC.
8. W. R. Wilcox, J. Crystal Growth 13/14, 787 (1972).
9. K. H. Chen and W. R. Wilcox, I & EC Fund. 11, 563 (1972).
- *10. W. R. Wilcox and V.H.S. Kuo, in preparation
11. T. H. Etsell and S. N. Flengas, J. Electrochem. Soc. (Jan. 1972).
- *12. A. L. Esquivel, W. N. Lin, and D. B. Wittry. Bull. Amer. Phys. Soc. Ser. II 17, 1194 (1972).
13. S. R. Morrison, Phys. Rev. 104, 619 (1956).
14. T. Figielski, Phys. Stat. Sol. 6, 429 (1964).
15. T. Figielski, Phys. Stat. Sol. 9, 555 (1965).
16. T. Figielski, Phys. Stat. Sol. 10, 75 (1965).
- *17. A. L. Esquivel and S. Sen, Bull. Amer. Phys. Soc. Ser. II 17, 1195 (1972).
18. W. T. Read, Jr., Phil. Mag. Ser. 7, 47, 111 (1955).

* Papers resulting from this grant.

19. R. M. Broudy, Adv. Phys. 12, 135 (1963).
20. R. A. Logan, G. L. Pearson and D. A. Kleinman, J. Appl. Phys. 30, 885 (1959).
21. R. L. Bell and A. F. W. Willoughby, J. Mater. Sci. 5, 198 (1970).
22. C. M. Wolfe, G. E. Stillman, and J. A. Rossi, J. Electrochem. Soc. 119, 250 (1972).
23. O. G. Lorimor and W. G. Spitzer, J. Appl. Phys. 37, 3687 (1966).
24. W. G. Spitzer and W. P. Allred, J. Appl. Phys. 39, 4999 (1968).
25. R. J. Elliott and P. Pfeuty, J. Phys. Chem. Solids 28, 1789 (1967).
26. M. E. Levy, private communication.
- *27. W. N. Lin and D. B. Wittry, Bull. Am. Phys. Soc. 17, 1194 (1972).
- *28. H. C. Marciniak and D. B. Wittry, Proc. 7th Nat. Conf. on Electron Probe Analysis (San Francisco, July 1972).
29. Chan Yet-Chong and A. M. Forrest, Jour. of Sci. Insts. (Jour. of Phys. E) Series 2, Vol. 1 (1968).
30. S. M. Sze, Physics of Semiconductor Devices, (John Wiley, New York, 1969), p. 35.
- *31. C. L. Anderson, R. Baron, and C. R. Crowell, The International Electron Devices Meeting, December, 1972.
32. G. I. Roberts and C. R. Crowell, Jour. Appl. Phys. 41, 1767 (1970).
33. G. I. Roberts and C. R. Crowell, Solid-State Electronics 16, 29 (1973).
- *34. C. L. Anderson, T. W. Kao, and C. R. Crowell, submitted to Solid-State Electronics
- *35. C. R. Crowell, T. W. Kao, C. L. Anderson, and V. C. Rideout, Surface Science 32, 591 (1972).